LA-UR-09-01860

Design Fundamentals for Cost-Optimized Neutron Detectors Based on an Array of Helium-3 Tubes

By

Randy J. Spaulding

A thesis submitted in partial fulfillment of the

Requirements for the degree of

MASTER OF SCIENCE

IN

PHYSICS

IDAHO STATE UNIVERSITY

2009

This work was funded by in part by DHS [fund #] and DTRA [fund #]

Table of Contents

List of Figures

List of Tables

LA-UR-09-01860

Abstract

Helium-3 gas has long been a popular medium for neutron detection because of its enormous 5320 barn thermal cross-section. Unfortunately, helium-3 is not found in significant naturally-occurring quantities on Earth. The existing supply of helium-3 is essentially exclusively limited to the radioactive decay of tritium stockpiles. Increasing competition over the world's finite helium-3 reserves creates an urgent need to utilize the gas in the most efficient manner possible. A new concept for neutron detector design using an array of low-pressure helium-3 drift tubes nestled inside a polyethylene lattice has been developed at Los Alamos National Laboratory (LANL). This detector design promises to be 2.5 to 3.5 times more efficient than old-style high-pressure helium-3 tubes. A prototype detector containing 72 tubes was constructed at Los Alamos for benchmarking purposes as well as supporting standoff interrogation experiments. The Monte-Carlo code MCNPX shows excellent agreement with benchmarking experiments that were performed in 2008-2009. A new concept for a semi-deterministic method for calculating detector responses to environmental neutron scattering, called efficacy, is also introduced. The complete development of this technique is left as future work.

Chapter 1 : Introduction

1.1 History of the Neutron

The discovery of the neutron is credited to J. Chadwick in 1932. Chadwick was following up on an observation made by I. Curie-Joliot and F. Joliot in 1931; in 1930, Bothe and Becker had first produced radiation that they assumed consisted of "very penetrating gamma rays" by bombarding light elements such as boron and beryllium with polonium alpha rays. In studying this further, Curie-Joliot and Joliot observed radiation that behaved like energetic protons when sheets of paraffin were placed in the path of this yet-unknown radiation. They calculated the photon energy required to produce these protons through a process similar to the Compton effect to be an unrealistic 55 MeV. Chadwick confirmed that these were indeed protons and postulated that they were instead being produced by massive, energetic particles having a neutral electric charge. The lack of electric charge of these "neutrons" explained their ability to penetrate matter with little absorption [1].

Unfortunately, the lack of electric charge also makes it impossible to measure the mass of the neutron by conventional electromagnetic means. It was not until two years later in 1934 that Chadwick and Goldhaber were able to first measure the mass of the neutron by splitting deuterons with Thorium gamma-rays [2]. The neutron rest

mass, now commonly used as a physical mass reference constant[1], is

$m_n = 1.6749286 \times 10^{-24}$ g.

1.2 Neutron Detection

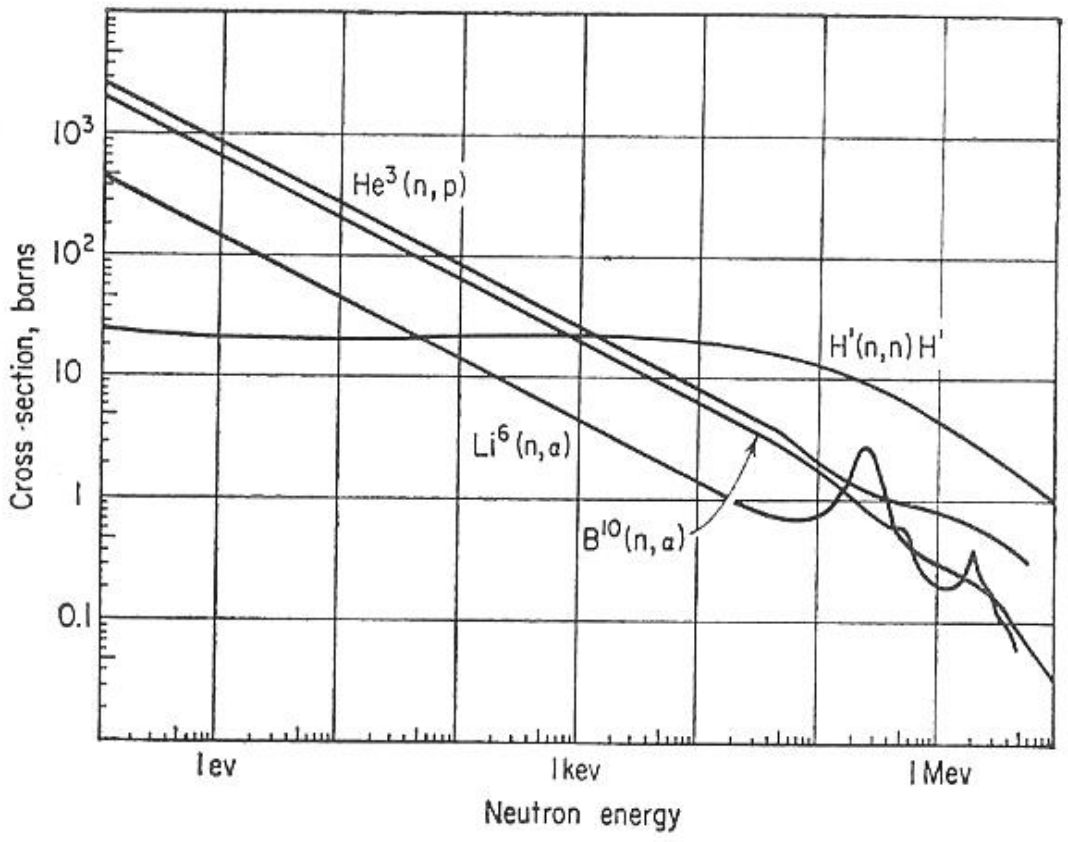

Figure 1: Cross section versus neutron energy for several common neutron-detection processes [4]

The very long interaction length resulting from the zero net electric charge of the neutron also makes it very difficult to detect them directly. However, neutrons do have a significant cross-section for many nuclear interactions such as elastic

[1] In the modified nuclear system of units commonly used in computer codes, the neutron mass is defined to be equal to 1 mass unit. In this system, the mass of carbon-12 equals 11.8969142 units and Avogadro's number is 5.9703109×10^{23} [3].

scattering, inelastic scattering, (n, γ), (n, p), (n, n'), (n, fission) etc. Neutrons are easily detected via interactions of the secondary charged particles produced during one of the preceding nuclear reactions.

1.2.1 Types of neutron detectors

The reaction products are detected either in real time via direct charge conversion, or offline, by activation of a sample and monitoring of its radioactive decay [4]. Charge-conversion methods are predominant in most nuclear experiments because they give immediate or near-immediate results, while activation techniques [3] remain popular for small-scale experiments, high-radiation environments, and applications where the neutron spectrum needs to be known, such as boron-neutron capture therapy (BNCT) [6]. This document will focus on a handful of the real-time techniques that offer the highest detection efficiency; the reader is invited to refer to [4] for a more complete discussion.

Figure 1 shows the cross-section for several of the most common reactions used in neutron detection. The strong energy dependence shown by these examples is characteristic of all neutron interactions. As a result, the scientist typically has a large degree of freedom in choosing the detector that is most suited to the energy range of neutrons present in his or her experiment.

Reactions whose cross-sections dominate at low neutron energies can be used effectively for detecting high-energy neutrons by adding moderating material around the detector. The moderating material slows the neutrons down through multiple scattering events. The energy lost by the neutron in scattering from a nucleus of mass A is readily calculated from kinematics:

$$\frac{E'}{E} = \frac{A^2 + 1 + 2A\cos\theta}{(A+1)^2} \qquad (1.1) \quad [8]$$

where E is the initial energy of the incident neutron, E' is the final energy, and θ is the scattering angle in the center-of-mass frame. The relationship between energy loss and mass of the nucleus is more apparent when this equation is rewritten in a different form:

$$\Delta \equiv 1 - \frac{E'}{E} = \frac{2A}{(A+1)^2}(1 - \cos\theta) \qquad (1.2)$$

which clearly shows that the energy lost decreases as atomic mass increases. Thus, light nuclei, in particular hydrogen, are the most effective neutron moderators, as they absorb a greater fraction of the incident neutron's energy per collision. This form also shows that maximum energy loss occurs at $\theta = \pi$ (pure backscattering) and no energy transfer occurs for $\theta = 0$ (no collision). The most popular moderating material is polyethylene ($(CH_2)_n$). Polyethylene has density similar to water (~0.89-0.97 g/cm^3) and high hydrogen content (14% by mass), which makes it substantial enough to be an effective moderator while being less bulky and easier to handle in the laboratory than heavy metals. It is also inexpensive to produce and machine. The density of polyethylene increases as the average length of the ethylene chains grows. Polyethylene sold commercially is sorted by chain length and categorized by density. High-density polyethylene (HDPE) obtained in such fashion typically has a guaranteed average density of 0.93-0.95 g/cm^3.

1.2.1.1 Scintillator-based proton recoil detectors

Scintillator-based proton recoil detectors take advantage of the n-p elastic scattering reaction which has a large cross-section over a wide range of neutron energies (denoted $H^1(n, n)H^1$ in Figure 1). The recoil proton creates electrons through ionization and these electrons in turn create optical photons through the scintillation process. The total optical energy is directly related to the energy transferred to the scintillator by the incident neutron. The difficulty with detecting neutrons with scintillator detectors is that they are quite sensitive to all forms of ionizing radiation and it is very difficult to discriminate low-energy neutron signals from gammas, betas, etc. based on traditional pulse-shape or rise-time-discrimination methods. The inclusion of high-Z shielding materials can improve this to some extent, as the neutrons easily penetrate such materials but gammas and betas are absorbed. However, scintillation detectors remain most useful for fast neutrons (>2 MeV) where the neutron signals can readily be discriminated from competing signals, with efficiencies on the order of 30% [9][2]. Scintillation detectors also become very effective at detecting thermal neutrons when loaded with thermal absorbers such as boron and lithium. Efficiencies in the thermal regime can effectively reach 100% [11, 12].

[2] The theoretical efficiency for direct detection of fast neutrons is as high as 90%. Imperfect discrimination of gamma-rays reduces the effective efficiency considerably [10].

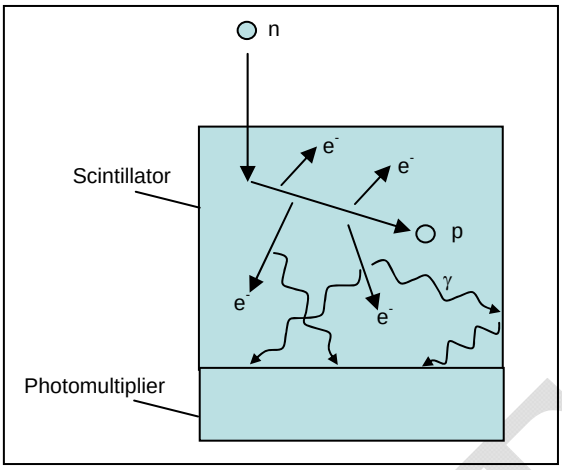

Figure 2: Organic scintillation detectors detect fast neutrons via proton recoil.

1.2.1.2 Helium-3

Helium-3 is a monatomic gas having density 0.134 x 10^{-3} g/cm^3 at standard temperature and pressure (STP). The He-3(n, p)t reaction has a cross-section of 5320 barns [13] for thermal neutrons[3]--fourth-greatest among the stable nuclides behind only Gd-157 (2.54E5 bn), Gd-155 (6.09E4 bn), and Eu-151 (5.90E3 bn) [14]. The large cross-section and modest range of its daughter particles make He-3 ideal for use in gaseous tubes. The helium-3 gas is typically mixed with a proportional gas and possibly also a quench gas to improve signal-to-noise and stabilize the Townsend avalanche. Historically, detectors have been typically operated at a pressure of 2-10 bar[4] to maximize neutron detection efficiency. However, this practice is very wasteful of the He-3 gas because of decreasing returns in efficiency as pressure is increased. There is a significant ongoing effort at Los Alamos National Laboratory

[3] In this document, "thermal" neutrons refers to T = 293.15K (kT = 0.02526174 eV)

[4] In the CGS system of units, 1 bar = 10^5 Pa = 1 / 1.01325 atm.

(LANL) studying the use of atmospheric-pressure tubes containing a few hundred mbar of helium-3 in hopes of reducing this wastefulness on a widespread scale[5].

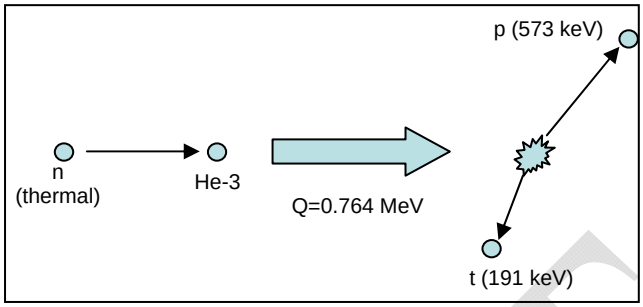

Figure 3: The ^{3}He(n,p)t reaction for thermal neutrons

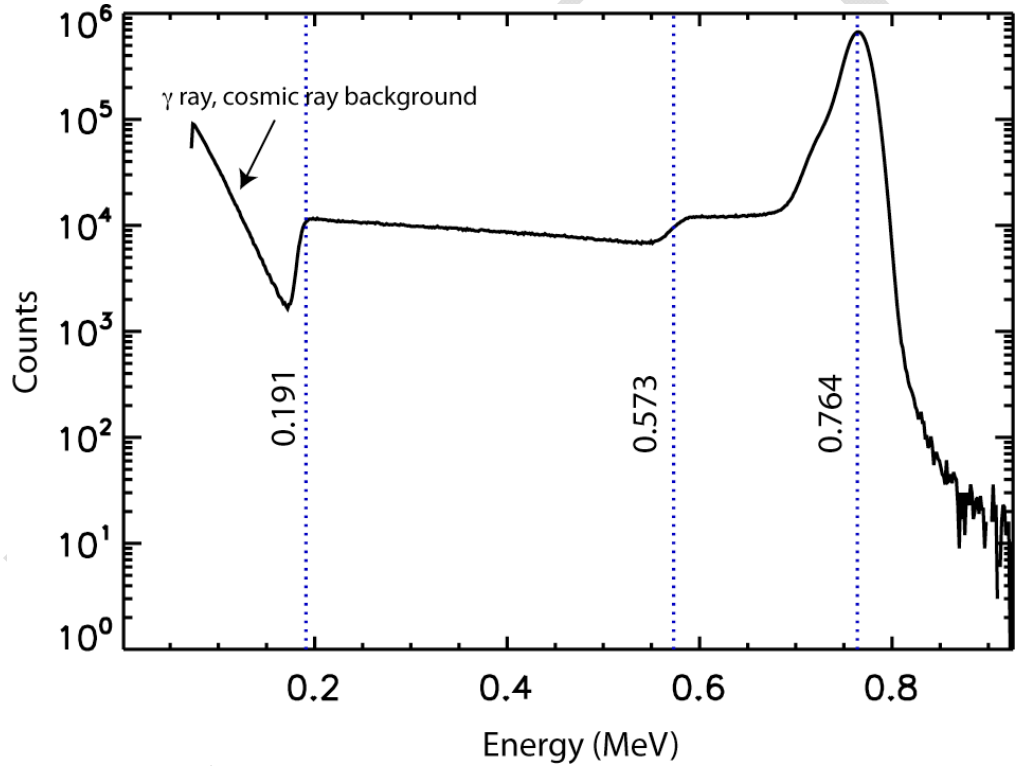

Figure 4: Energy spectrum of 2”-dia. x 48"-long detector containing 200-mbar He-3 and 800-mbar proportional gas. Neutron counts appear above 191-keV and background counts from gamma-rays, cosmic rays, and electronic noise appear at lower energies, as indicated. Wall effects from both p (573 keV) and T (191 keV) daughters are clearly resolved [15].

[5] See §1.3 and §1.4 for a full discussion.

Figure 4 shows an energy spectrum representative of atmospheric-pressure He-3 detectors. The proportional gas produces a sharp full-energy peak having a full-width-at-half-maximum (FWHM) ~5%. The low-energy background peak is produced by electronic noise, gamma-rays, and cosmic-ray muons and is typical of all gaseous detectors. The two "shelves" at 191-keV and 573-keV are produced when one of the energetic daughter particles (proton or triton, respectively) intersects the wall of the tube and does not deposit its entire energy in the gas. The energetic proton from the He-3 reaction has a range of ~1.5 cm in atmospheric-pressure tubes, while the triton's range is ~0.5 cm. These wall effects, which are present in all gaseous neutron detectors, cause a minor loss in counting efficiency, as counts that do not contribute to the full-energy peak could be lost in the noise/cosmic-ray background peak that appears at low energies. This is not a great concern for a fairly new tube, as the wall effects represent a small fraction of the total counts and the background is easily discriminated out. However, the noise level tends to increase as the tube ages because of effects such as gas spoiling, or gradual replacement of the proportional gas with air by leakage and diffusion through the wall of the tube. Gas spoiling also causes wall effects to increase slightly because the air is less dense and has less stopping power than the proportional gas. Consequently, the range of the charged particles increases as proportional gas is lost. Researchers at LANL are currently developing techniques that will be applicable to all gaseous proportional counters, to monitor the health of the tube and predict its remaining lifetime [15].

1.2.1.3 Boron-10

Boron-10 is another popular medium for thermal neutron detection due to its high cross-section (3845 bn [13]) and high Q-value (see Figure 5). As depicted in the figure, the B-10(n,α)Li-7 reaction can populate either the ground state of the Li-7 ion or the first excited state. In the latter case, the excited Li-7 nucleus immediately decays to ground[6], emitting a 477-keV gamma ray. Boron-10 is only 19.9% abundant in natural boron, the remainder being Boron-11. For this reason, it is typical to use isotopically-enriched boron-10 in neutron counters.

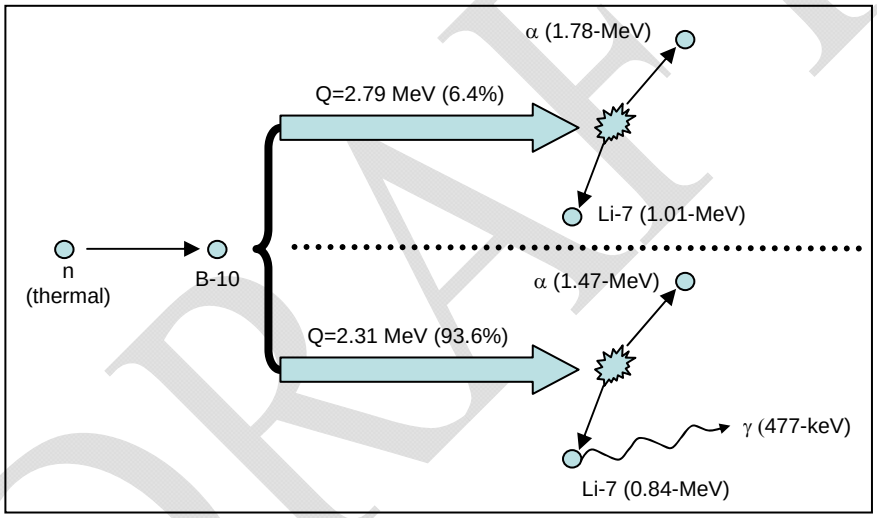

Figure 5: Thermal neutron capture on Boron-10

Boron is used for neutron detection in several schemes involving both solid and gaseous forms [4]. The most common form used is B-10-enriched gaseous boron triflouride (BF_3), which has a density of 2.99 x 10^{-3} g/cm^3 at STP at 100% B-10 enrichment and contains 14.9% B-10 by mass. The sensitivity of BF_3 detectors is

[6] The half-life of the first Li-7 excited state is 73 fs [12].

somewhat lower than that of He-3. However, Stokes, Meal, and Myers showed that BF_3 detectors are particularly radiation-resistant and can be operated in gamma fluxes of 1000 R/hr or more [17], making them attractive for mixed-waste and reactor applications.

1.2.2 Detector Efficiency

The concept relating the measured count rate in an experiment to the current of interacting particles present is called efficiency[7]. There are several methods of defining detection efficiency; the terminology used in this document for the most common definitions will be: a) conversion efficiency, b) intrinsic efficiency, and c) total efficiency. Another quantity commonly used by commercial detector manufacturers is sensitivity, which is defined as counts per second per unit incident particle flux. Many of these quantities involve assumptions about the energy and/or angular distribution of the incident particles, as will be explained in following sections.

Conversion efficiency refers to a detector's absolute ability to convert the energy from a reaction into recordable signals, and is defined by:

$$\varepsilon_C(E) = \frac{\text{signals out}}{\#\text{ of reactions involving particles having energy } E} \leq 1$$

Conversion efficiency is the probability of obtaining a useful signal each time the desired reaction occurs. This plays a fundamental role in determining the count rate from a nuclear experiment. In general, the contribution to the count rate dC in a

[7] The reader should continually keep in mind that the context of this development is emphasized toward detection of high-energy neutrons from active-interrogation methods, although much care has generally been taken to present the concepts in a way applicable to all nuclear counting experiments.

volumetric detector for particles having energy between E and E + dE in the volume element dV is the reaction rate dR times the quantum efficiency, or:

$$dR = N(\vec{r}) \cdot \frac{\partial \sigma}{dE}(E) \cdot \Phi(\vec{r}, E) dE dV \qquad (1.3)\ [4]$$

$$dC = \varepsilon_C \cdot dR = \varepsilon_C(E) \cdot N(\vec{r}) \cdot \frac{\partial \sigma}{dE}(E) \cdot \Phi(\vec{r}, E) dE dV \qquad (1.4)$$

where $N(\vec{r})$ = number of target atoms per unit volume

$\frac{\partial \sigma}{dE}$ (E) = reaction cross-section at energy E

$\Phi(\vec{r}, E)$ = flux per unit energy interval, defined as

$$\Phi(\vec{r}, E) \equiv v \cdot n(\vec{r}, E) \qquad (1.5)\ [7]$$

where $n(\vec{r}, E)$ = number density, the number of particles of interest per unit volume, and v is the velocity of the particles.

In practice, determination of the conversion efficiency can be quite complicated, as most physical detectors employ multiple energy conversion schemes to produce the final signal and many of the reactions themselves involve multiple chains, e.g. B-10 (n, α) {Li-7, Li-7*}. Thus, experimenters frequently neglect direct determination of the conversion efficiency. However, it cannot be neglected when particle transport codes such as MCNPX[8] are used, as the code can only estimate the reaction rate—not the actual count rate in the detector. In many cases ε_C can be assumed to be equal to or near unity over the entire applicable energy range. The detectors described in this document generally all fit this requirement.

[8] See § 3.1 for a description and discussion of the MCNPX code.

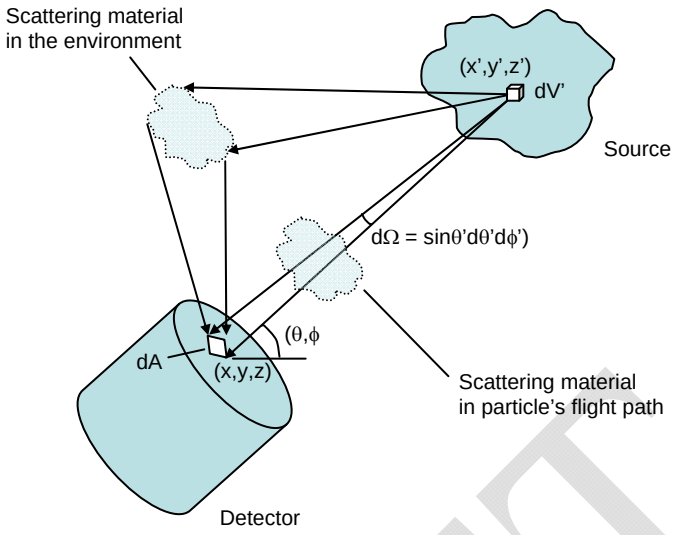

Figure 6: Detection of particles in a nuclear physics experiment

Total efficiency ε_T and intrinsic efficiency ε_I are inherently related quantities describing the count rate for a particular experimental configuration. Total efficiency is defined as counts per particle emitted from the source, while intrinsic efficiency is defined as counts per particle crossing the detector boundary. In the most broad sense, the relationship between the two involves the angular emission characteristics of the source; the geometry of the experiment, including the physical sizes and placement of source and detector; and the presence of scattering materials in the flight path of the particle and the environment:

$$\varepsilon_T(E) \equiv \frac{\int dV' d\theta' d\phi' dA \cdot \varepsilon_I(E', \vec{r}, \theta, \phi) \cdot \Im(E, E', \theta', \phi', \theta, \phi) \cdot \frac{\partial^2 I}{\partial \theta' \partial \phi'}(E, \vec{r}', \theta', \phi')}{\int \frac{\partial^2 I}{\partial \theta' \partial \phi'}(E, \vec{r}', \theta', \phi') dV' d\theta' d\phi} \qquad (1.6)$$

where I is the source emission rate of particles originating from the point (x', y', z'), having energy E, into the cone $d\Omega = \sin\theta' d\theta' d\phi'$; ε_I, the intrinsic efficiency, is the

fraction of particles having energy E', crossing the point (x, y, z) on the detector's surface, at the angles of incidence θ and ϕ, that create useful signals in the detector; and $\Im(E,\theta,\phi,E',\theta',\phi')$ is the transfer function that envelops all interactions experienced by every source particle during its flight from the source to the detector. The transfer function accounts for attenuation and up- or down-scattering during transmission; environmental effects such as off-angle particles scattered toward the detector; secondary particle production; etc. In this form, the integral in the numerator is over the source volume, all source angles, and the detector surface area. The integral in the denominator is over the source volume and all source angles and is written explicitly to emphasize that, in order to achieve the proper normalization of "per source particle" one must normalize to the total source activity. Note that $|\Im|$, the magnitude of the scattering function, can be >1, particularly for showers created by high-energy particles, representing multiplication of the source particles by reactions such as (n, xn).

Equation (1.6) represents the formal relationship between ε_T and ε_I; however, its purpose in being presented here is merely to broaden the reader's thinking about nuclear physics experiments for the forthcoming discussion. In practice, nearly all nuclear physics experiments employ a general strategy of reduction of the effects of finite source size and scattering objects--both in-flight-path and environmental--to negligible levels or eliminate them entirely. When this is true, the above expression can be greatly simplified to the more palatable form:

$$\varepsilon_T(E) = \varepsilon_I(E) \cdot \frac{\Omega_{sd}}{4\pi} \tag{1.7}$$

or alternatively

$$\varepsilon_T(E) = \varepsilon_I(E) \cdot \frac{A}{4\pi R^2}, \qquad \pi R^2 \gg A \tag{1.8}$$

where Ω_{sd} is the solid angle of the source subtended by the detector, A is the surface area of the detector, and R is the distance to the source. As shown by Eq.(1.8), if the detector is small relative to the square of the source distance, the fractional solid angle is well approximated by the ratio of the projected area of the detector to the surface area of a sphere having radius R. This assumption goes hand-in-hand with the assumption that angular effects at the detector surface are negligible that was already inherently made in writing Eq.(1.7). In practice, this is further simplified by averaging the convolution of the detector's efficiency and the energy spectrum of the source over the applicable energy range, so that the efficiency can be conveniently quoted by a single number[9]:

$$\overline{\varepsilon_{T,I}} \equiv \frac{\int \varepsilon_{T,I}(E) \cdot \frac{d\Phi}{dE}(E)dE}{\int \frac{d\Phi}{dE}(E)dE} \tag{1.9}$$

1.2.3 Cf-252 neutron source

The majority of experiments presented herein used various Cf-252 neutron sources at Los Alamos National Laboratory. Cf-252 has a half-life of 2.645 years,

[9] Note on terminology: whenever the term 'efficiency' appears by itself throughout the remainder of this document, it refers to the average intrinsic efficiency of Eq.(1.9)

undergoing alpha decay with a branching ratio of 96.91% and spontaneous fission with a branching ratio 3.09% [19]. The average neutron multiplicity per fission is 3.76 [20, 21], which results in a neutron emission rate of $2.314\text{E}6\,\text{n}\cdot\text{s}^{-1}\cdot\mu\text{g}^{-1}$ [22]. The energy of the emitted neutrons is well approximated by a Maxwellian distribution having average energy $\overline{E} = 2.13 MeV$: $N(E) = \sqrt{E}\cdot\exp(-E/T)$, where the temperature $T = 2/3\cdot\overline{E} = 1.42 MeV$ [23].

The activity of a californium-252 source is not constant over an indefinite period of time. Two isotopes in particular become important contributors of secondary activity as a Cf-252 source ages: Cf-250, which is usually present as a minority impurity from the manufacturing process, and Cm-248, the product of Cf-252 alpha decay. Cf-250 has a half-life of 13.1 years and a neutron emission rate of $1.72\text{E}4\,\text{n}\cdot\text{s}^{-1}\cdot\mu\text{g}^{-1}$, while Cm-248 has a half-life of 340,000 years and an emission rate of $59\,\text{n}\cdot\text{s}^{-1}\cdot\mu\text{g}^{-1}$. The low emission rates relative to Cf-252 imply that both isotopes are negligible for the first several years of a new source's usage and only become a factor as the source weakens after many half-lives. The increase in the effective activity of the Cf-252 source by these isotopes is summarized in Table 1:

	Years to reach fractional increase, by isotope		
Fractional Increase in Cf-252 activity	**Cm-248**	**Cf-250 at 1% initial impurity level**	**Cf-250 at 0.1% initial impurity level**
10%	33.1	36.2	47.2
100%	41.9	47.2	58.2

Table 1: Effect of secondary isotopes on Cf-252 source activity

Cm-248 is always present in a Cf-252 source, as it is a natural product of the Cf-252 alpha decay[10]. Therefore, Cm-248 limits the amount of time a Cf-252 source can be used before buildup effects must be considered. The effective lifetime when simple exponential decay can be used is roughly 30 years. Furthermore, if the source is older than about 35 years one should make a serious attempt to determine the initial quantity of Cf-250 that was present. The oldest Cf-252 source used in these experiments was 21 years old; thus simple exponential decay still applies.

1.2.4 Note on calibration using check sources

The experimenter often desires to directly measure detector efficiency by means of a calibrated source standard. For fast neutron measurements with filled-gas-tube detectors such as He-3 and B-10, all information about the source neutron's energy is usually lost before detection. A direct result of this is that it is only possible to measure the flux-convoluted average efficiency as in Eq. (1.9). When doing so, the experimenter must keep in mind that the energy spectrum of the neutrons present in the experiment can be, and generally is, quite different from that of the source used in the calibration. If the detector response is nonuniform over the applicable energy range, this can result in the experimental efficiency being different from the calibrated efficiency. This is typically the case for gas-tube detectors. In some applications it is sufficient to simply make note of awareness of this situation, whereas in others it is crucial to quantify it through a source-correction factor:

---

[10] The half-life of Cm-248 is essentially infinite relative to human lifetime, and as 96.91% of the original Cf-252 ultimately becomes Cm-248 through alpha decay, one can consider Cm-248 to yield a constant terminal activity of an extinguished Cf-252 source of $57.2\ \mathrm{n \cdot s^{-1} \cdot \mu g^{-1}}$.

$$\varepsilon_{I\,\exp} = \gamma \varepsilon_{I\,src}$$

$$\gamma \equiv \frac{\int dE \cdot \left[\Phi_{\exp}(E)\right] \cdot \varepsilon_I(E)}{\int dE \cdot \left[\Phi_{src}(E)\right] \cdot \varepsilon_I(E)} \qquad (1.10)$$

where $\Phi_{\exp}$ is the experimental neutron energy spectrum and Φ_{src} is that of the source. The square brackets in Eq. (1.10) denote that this is a simplified form; the energy spectra are required to have the same normalization—both are typically normalized to unity. Monte-Carlo simulations have shown that gamma can easily vary from <0.6 to >1.7 [18]. An example calculation comparing several neutron energy spectra to a Cf-252 standard is presented in Figure 7:

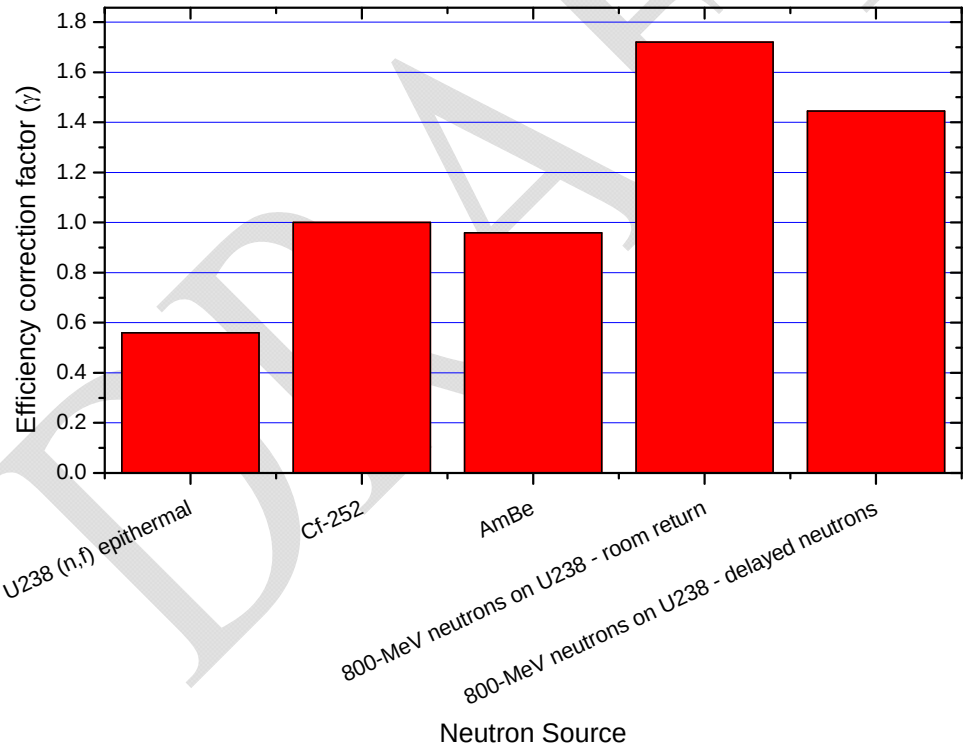

Figure 7: Comparison of detector response to Cf-252 standard neutron source and experimental spectra calculated with MCNPX. The spectra used in the 800-MeV proton data were obtained from MCNPX simulations of proton interrogation experiments conducted at LANL in 2007 and 2008.

1.3 Motivation for this work

The goals of traditional portal monitoring systems are to monitor and control the movement of specific items throughout the country, and on a larger scale, worldwide. In this modern era of heightened terrorist activity, systems such as these have become pivotal in keeping the world's people, governments, and economies safe and providing peace of mind for the general public. Of particular interest is the possible threat of a nuclear attack on United States soil. Prevention of such an attack requires (1) the detection of the Special Nuclear Material (SNM) in a safe and effective manner and (2) interception and neutralization of the material before it

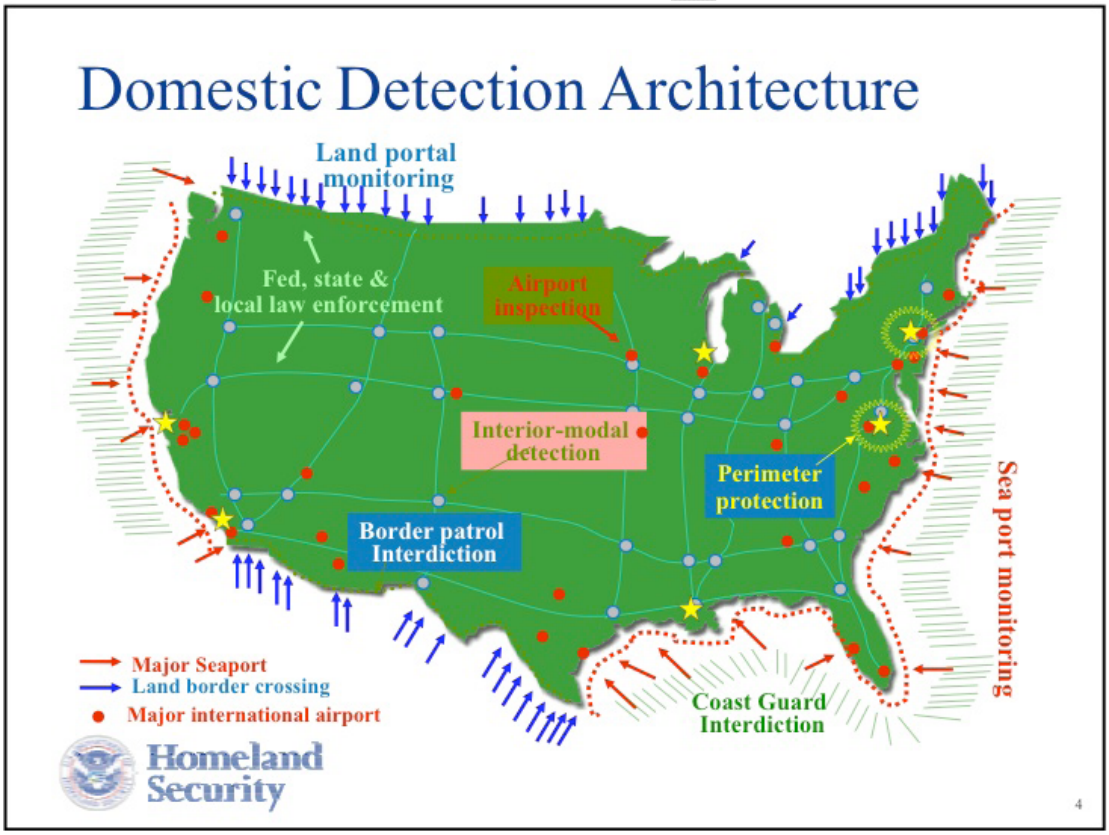

Figure 8: The Department of Homeland Security (DHS) employs multiple levels of detection and interdiction to thwart terrorist attacks in the United States [29]

reaches the primary target and before it can be released on a secondary target. The difficulty in the detection stage is that while nuclear materials emit unique and known radiation signatures, these signals are fairly weak and easily shielded from radiation detectors. An additional problem is the enormous scale of the task. Any comprehensive solution must therefore offer maximum efficiency at minimal cost and must also provide sufficient flexibility and scalability for deployment in a wide variety of portal monitoring scenarios.

1.3.1 Active interrogation

Existing passive-interrogation methods are largely ineffective, particularly on national and worldwide scales [30]. The difficulty in the task is that nuclear material is extremely difficult to obtain and terrorists in possession of a dangerous quantity would certainly go to extreme lengths to protect it [31]. The solution to the weak radiation signature from SNM is to use an active probe—an energetic beam of particles. Active techniques include x-ray imaging and signal enhancement through induced nuclear fissions in the target. The latter technique can employ neutrons, bremsstrahlung photons from high-energy electrons, or protons to produce signatures unique to SNM in the form of beta-delayed fission neutrons [32, 33, 34]. These signatures can also be used to identify the species of the nuclear material [35], which can aid in determining the threat level.

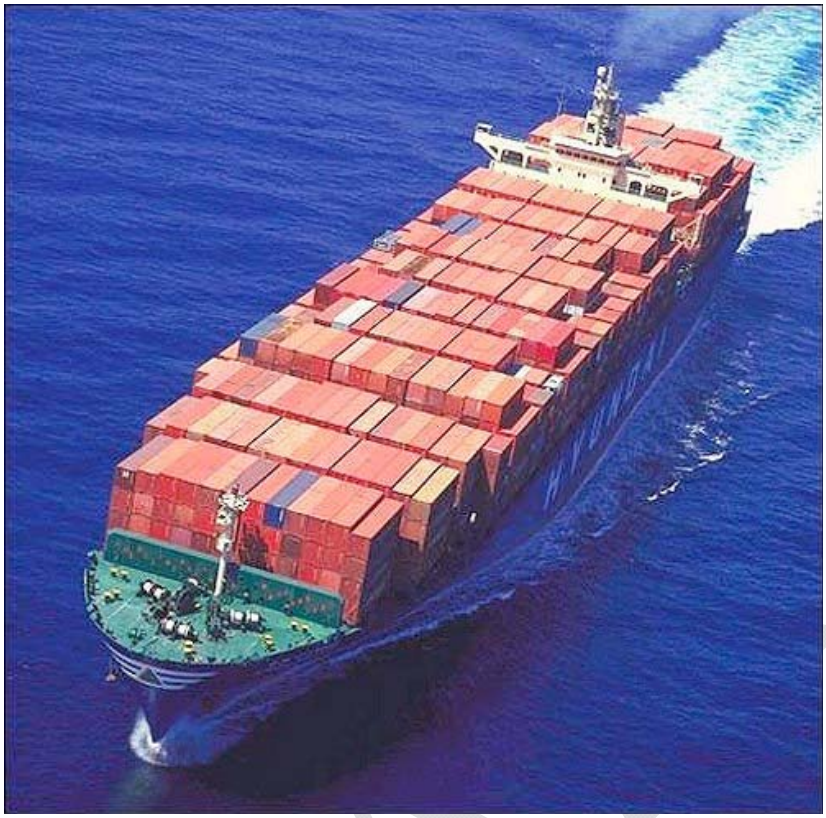

Figure 9: Mammoth cargo container ships, or "boxships" carry millions of containers across the world's oceans annually.

One of the greatest conceived threats is the smuggling of a nuclear device via ocean-going vessel [36]. Millions of containers per year enter the USA by cargo container ship, bound to destinations nationwide [37]. The largest existing cargo container ships are capable of carrying over 15,000 8'x8'x20' boxes [38]. The danger is that these container ships provide a way for the terrorists to defeat land-based interdiction by detonating the device in or around the seaport of a major city. An additional potential threat is a nuclear device being delivered to a neighboring country and transported to the U.S. shore on a smaller vessel such as a private yacht. Researchers at LANL are currently investigating means of interrogating these vessels at a safe distance from shore. This technique is referred to as *standoff interrogation*.

Figure 10: Many private vessels have an extensive range and provide another potential means of delivering a nuclear device to the United States.

1.3.2 Standoff interrogation

Standoff interrogation involves long-range scanning with a source-to-target distance from 100 m to perhaps 1 km or more[11]. This is extremely difficult to accomplish with bremsstrahlung and neutron beams; the range of photons is limited by absorption in air and a neutron beam would require an impractical high-energy flux. High-energy proton beams in the 800-to-4000 MeV range, however, are readily produced with sufficient current and a tight enough beam spot for such distances[12]. The dose delivered by the proton beam potentially poses a significant radiological risk to crewmembers on the ship and/or illegal immigrants who may be stowed aboard the ship. This imposes a limit on the amount of beam current that can be used,

[11] The original goal of 5-km is now believed to be impractical [39].

[12] Another potential method, quasi-passive interrogation using muonic x-rays exists [40]. The applicability of this technique to standoff interrogation is presently being studied at LANL.

and hence the available signal. Thus, maximization of neutron detection capability is crucial to this technique. helium-3 is the most attractive medium from a detection standpoint due to its superior efficiency compared to B-10 and lesser sensitivity to photon and charged-particle backgrounds compared to plastic scintillators. Unfortunately, He-3 is fairly expensive because it is quite rare on Earth. Additionally, competing demands for He-3 such as proposed power generation via nuclear fusion threaten to make it difficult to obtain large quantities in the years to come. Combining these factors it becomes immediately apparent that there is a very important cost factor associated with deploying He-3 detectors on any kind of national scale.

1.3.3 Fusion power and the worldwide He-3 shortage

The He-3 fusion reaction has been under extensive study for over 20 years and is now widely regarded to be one of the best long-term solutions to the world's energy crisis. Reactor engineering and development aside, the overwhelming problem is that we simply do not have enough helium-3. Early studies estimated that tens of metric tons of He-3 would be required per year to supply the USA's electricity demands. However, current worldwide He-3 production, being almost entirely limited to radioactive decay of tritium collected from spent nuclear fuel, is only in the tens of *kilograms* per year [41, 42, 43] —1000 times less than what is required to provide a viable fuel. Moreover, the amount of He-3 required to build a research reactor would essentially exhaust the entire present worldwide stockpile [42]. The solution to this emergency is beyond the scope of this work; however, its implication

to the Homeland Security effort is clear: He-3 use must be minimized by identifying and implementing the most efficient use of He-3 *on the basis of the quantity used*.

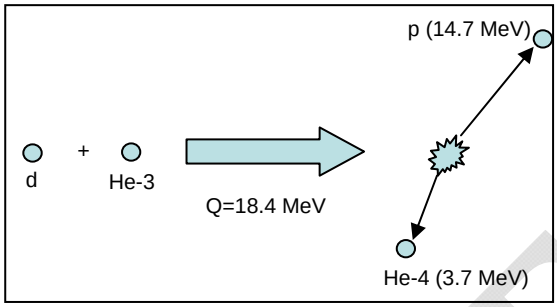

Figure 11: The d-He3 fusion reaction

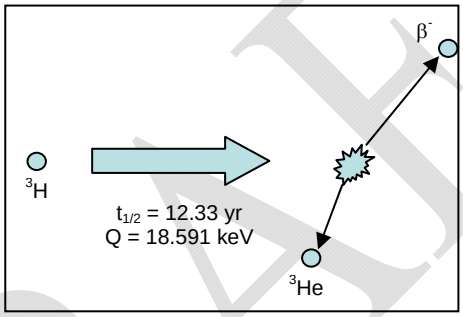

Figure 12: Virtually all helium-3 in present worldwide stores has been produced as a product of tritium β-decay.

1.4 Maximizing the efficiency cost factor for He-3 tubes

Historically, use of He-3 drift tubes in the laboratory has been governed by the mantra "maximum efficiency in minimum space." This has driven manufacturers to produce tubes containing as much as 40 atm He-3 [44]. Unfortunately, such high pressures result in very inefficient use of the He-3 gas due to self-shielding, increasing n-^{3}He elastic scattering, increased sensitivity to gamma-rays and charged particles, and other effects.

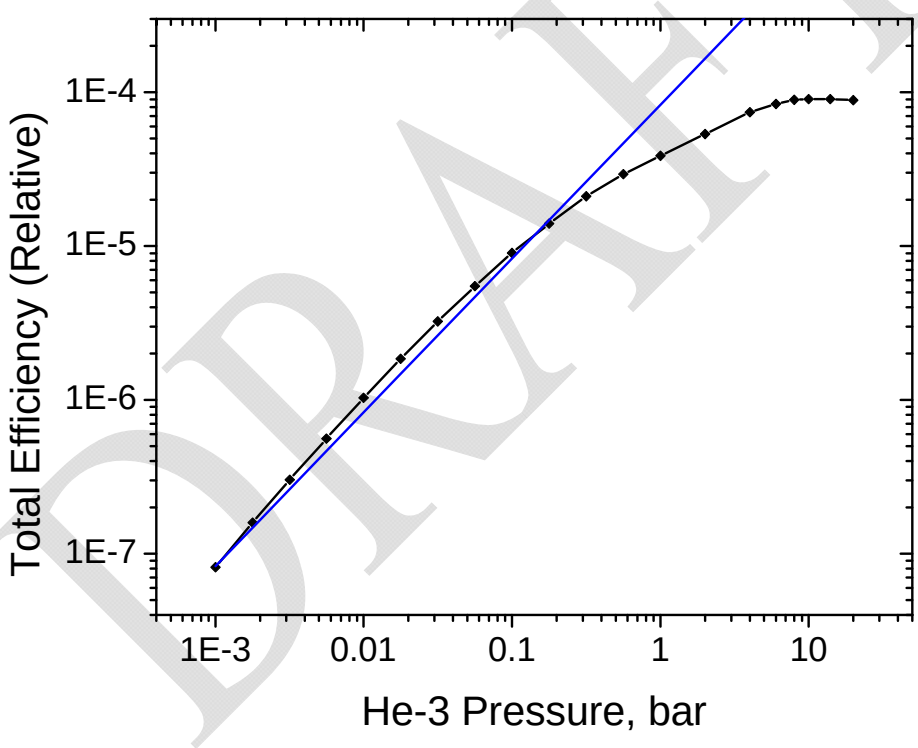

Figure 13: Efficiency of a 1" x 12" cylindrical He-3 detector versus He-3 partial pressure predicted by MCNPX [27]. The straight line represents proportionality. At low pressures the tube is filled to 1 bar with a proportional gas consisting of Argon, CF_4, and ethane (C_2H_6). The slope of the curve is greater than unity at very low pressures due to improved moderation provided by the fill gas itself.

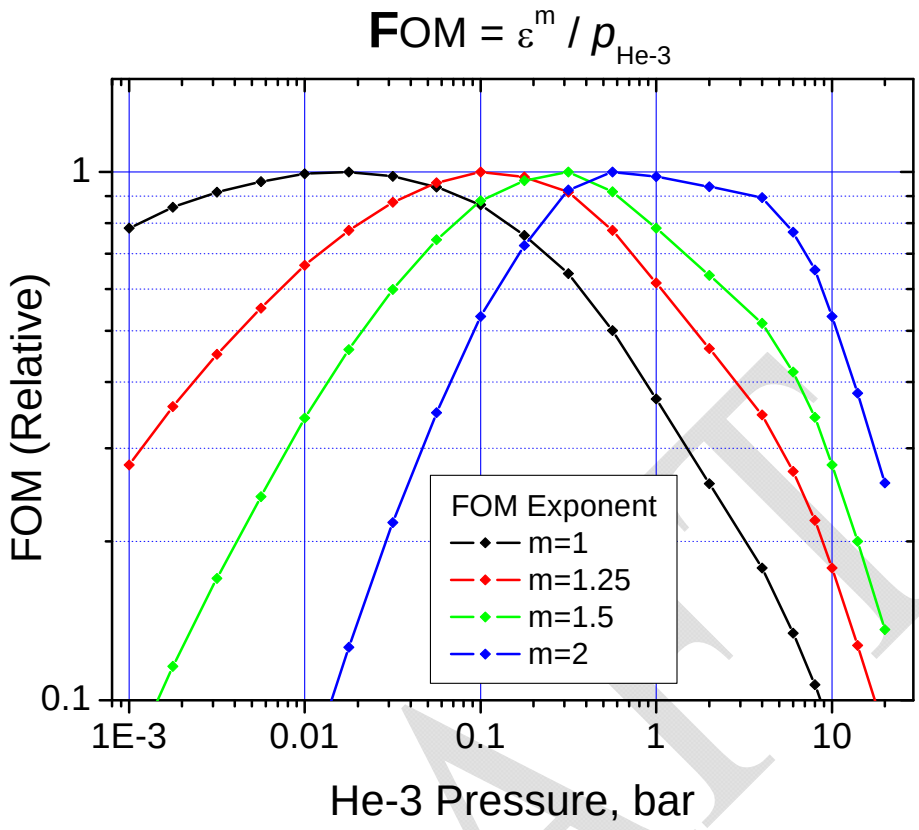

Figure 14: Efficiency Figure of Merit (FOM) given by efficiency per unit He-3 gas. The exponential weighting factor *m* controls the relative emphasis between efficiency and amount of gas used.

Figure 13 demonstrates the loss in efficiency as helium-3 pressure is increased for a typical research detector used at LANL. For *m*=1 in Figure 14, intrinsic efficiency is given equal priority to the quantity of gas used. This scenario assumes that total efficiency requirements can be satisfied by increasing the detector surface area indefinitely; the optimal partial pressure of He-3 in this regime is $P_{He\text{-}3} < 200$ mbar. At the other end of the scale, *m*>2 represents the traditional viewpoint that the amount of He-3 used is of no importance at all. This scenario is not without merit; constraints on laboratory space typically limit the size of detectors so that maximizing the volumetric count rate is crucial. However, this is not feasible for large-area

detectors such as those required for standoff interrogation applications[13] because (1) the cost of packing more gas into the tubes outweighs the cost of adding additional detectors, and (2) the amount of He-3 required to deploy such a high-pressure detector system nationwide simply does not exist terrestrially. However, traditional single-tube detector designs are not efficient enough at low pressures to satisfy count rate requirements[13]. This dilemma prompted LANL researchers to search for a new detector design that can better meet both requirements.

1.4.1 Track length and the arrayed detector[14] concept

Monte carlo computer codes employ the concept of track length in estimating particle flux in a volume as in Eqs. (1.3) and (1.4). Using (1.5) and $ds = vdt$, the time-integrated flux is given by:

$$\iiint_{V,E,t} \Phi(\vec{r},E,t)\cdot dt\cdot dE\cdot\frac{dV}{V} = \iiint_{V,E,t} n(\vec{r},E,t)\cdot ds\cdot dE\cdot\frac{dV}{V} = T_l/V \qquad (1.11) \quad [7]$$

where T_l is the total track length, or the total distance traveled by all particles of interest throughout the volume. It is important to note that T_l includes reentrant tracks as well as secondary tracks made by particles produced in the volume. Therefore, there is an alternative to increase the count rate; instead of the classical way—increasing N in (1.3) and (1.4) by packing more gas into the tube— increase

---

[13] Back-of-envelope calculations suggest that, at 35% intrinsic efficiency, 100 m^2 active detector area is required per (100 m)^2 standoff distance. This figure may change dramatically as detection goals and radiological limitations are finalized.

[14] Important terminology distinction: the term ‘detector’ is confusing as it can refer to anything from a single counter to a huge assembly consisting of hundreds of counters involving multiple particle species. To avoid confusion, every effort has been made throughout this document to limit the use of the word ‘detector’ to an entire assembly of shielding, moderation, and counters. Individual He-3 proportional counter are referred to as ‘tubes.’

T_l by placing an array of He-3 tubes inside a lattice of material having a high neutron albedo[15] and good moderating characteristics—typically HDPE and/or carbon (see Figure 15). In this design, the thickness of the separating layers between the cells, or separators (C and D in Figure 15) is chosen so there is a 20-30% chance of reflection from each layer (see Figure 16). The neutrons are thus allowed to penetrate several layers within the detector before losing a significant amount of kinetic energy. The albedo increases after each collision due to the energy loss, and the neutrons are effectively trapped within the interior of the lattice. They continue scattering from the walls, thermalizing gradually until they are either absorbed in one of the He-3 tubes or being captured on a hydrogen atom[16]. Each neutron thus passes through many tubes before being captured. This large increase in track length allows the experimenter to use relatively low He-3 partial pressure; making much more efficient use of the gas in the detector per Figure 13. The common term used to refer to such detector designs is ANDY, an acronym for Arrayed Neutron Detector.

[15] In nuclear applications the term *albedo* describes the fraction of incident particles that are reflected from an object's surface.

[16] The neutrons can also be captured by atoms in the air or the tube constituents; however, these effects are negligible compared to hydrogen capture H(n, γ)d. The fraction of neutrons lost in this fashion is briefly discussed in following chapters.

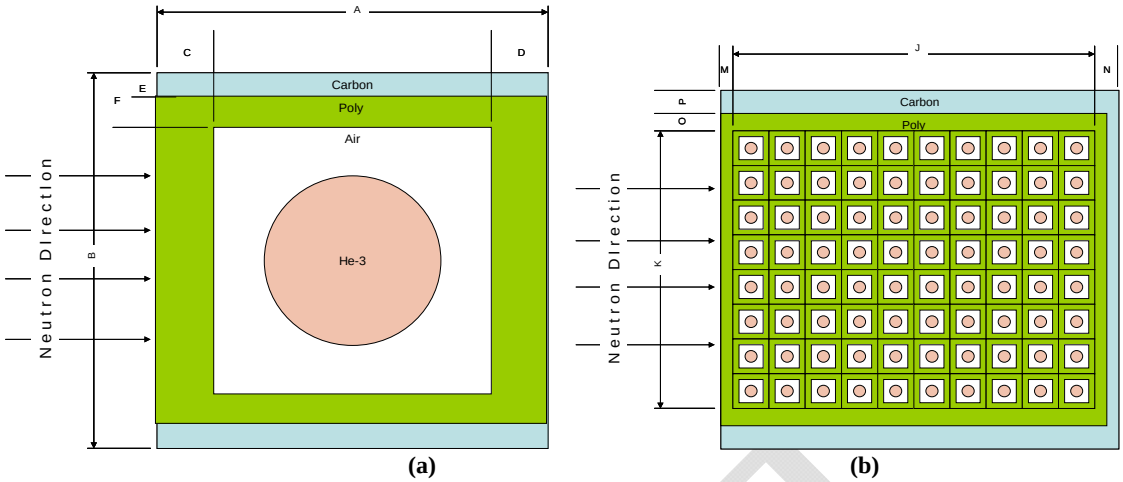

Figure 15: (a) Lattice cell containing a single He-3 tube, and (b) lattice configuration including an outer carbon reflector.

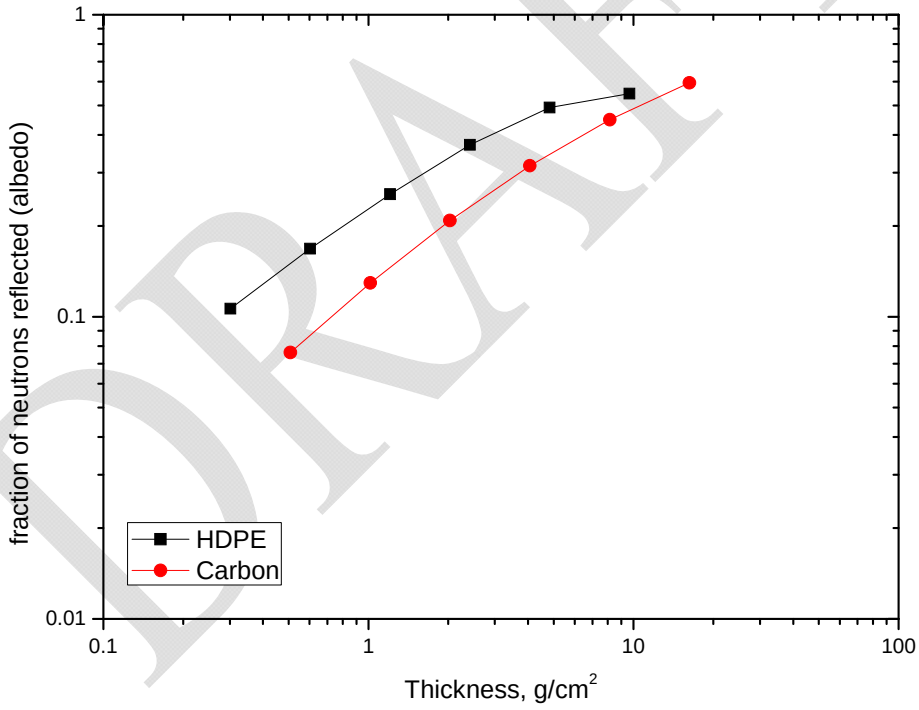

Figure 16: Neutron albedo for HDPE and Carbon slabs. The incident neutron field was a semi-isotropic Watt fission spectrum from thermal neutrons on U-235: $f(E) = C\exp(-E/0.988)\sinh(2.249E)^{1/2}$

Chapter 2 : Theory of environmental effects: The Efficacy[17]

The experimenter usually has direct control over the source and thus minimizing—or at least understanding—source size effects is trivial. However, one must remember that neutrons have a high scattering cross-section for many materials commonplace in the laboratory, particularly those containing significant amounts of low-Z materials—most notably of course, hydrogen—such as concrete, wood, asphalt, cooling water, and plastic. Therefore, real-world neutron counting experiments can seldom completely ignore scattering effects. This is particularly true for many active interrogation applications, where the scientist may have little control over the source and its environment[18]. Hence, it is proposed to modify Eq. 1.3 by introducing a new term describing a given detector's efficiency in a given environment: the *efficacy*:

$$\begin{aligned} \overline{\varepsilon_e} &\equiv \overline{\varepsilon_I} \cdot (\kappa + 1) \\ \kappa(\textit{efficacy}) + 1 &\equiv \kappa_\Phi \cdot \kappa_\gamma \end{aligned} \tag{2.1}$$

where $\overline{\varepsilon_e}$ is the experimental efficiency and the two coefficients κ_Φ and κ_γ represent all environmental effects combined into two factors: the change in incident flux and the change in efficiency due to the perturbation of the neutron energy spectrum and

[17] The term efficacy is adopted from the context of healthcare, where it describes the capacity of a treatment to produce a certain effect [26].

[18] The experimenter may actually have a strong motivation to avoid interfering with the source--in fact desiring to stay as far from it as possible. One example situation where this applies is inspection of a container that is suspected of containing a weapon that could potentially be activated remotely!

incident geometry, respectively. The efficacy, then, is the *fractional increase in the number of counts in the detector, per source particle travelling directly from the source to the detector's active surface, due to environmental interactions.*

2.1 Understanding the two components of Efficacy

The two components κ_Φ and κ_γ are inextricably related to one another, as virtually all nuclear processes are strongly energy-dependent and involve both energy and momentum transfer; however, it is useful to consider them conceptually distinct, as the following sections will illustrate.

Note that nearly all detectors used in nuclear science are somewhat sensitive to particles entering the detector at positions not considered part of the active area. This is particularly true for detectors that count fast neutrons by relying on external moderation to reduce the energy of the neutron to thermal levels. Therefore it is important to take note that the detector area involved in the efficacy comprises the *entirety of the detector's outer surfaces*[19].

2.1.1 Effects of environmental scattering on particle flux

To reiterate, κ_Φ is the overall change in magnitude of the particle flux entering the detector due to environmental interactions. As shown in Figure 17 below, changes in particle flux arise from many objects and processes. The challenge faced by the experimentalist is analyzing the environment and accurately determining which objects will have the greatest effect on the particle flux. A solid

[19] The surface area used for normalization, however, remains the detector's front face, the same as used in calculating the intrinsic efficiency.

apriori assessment will serve as a guide for decisions such as detector placement, location and makeup of supporting apparatus, source configuration, etc. The primary considerations are the object's solid angles relative to the source and detector and total cross-section for neutron interactions. Obviously, hydrogenous materials such as wood, oil, water, concrete, etc. near the source or detector are particularly troublesome and should generally be avoided when possible. Depending on the specific application it is not always necessarily to measure κ_{Φ} but the experimenter should consider it a general requirement to at least achieve a reasonable estimate of its magnitude and take whatever steps are possible to restrict it as close to unity as possible.

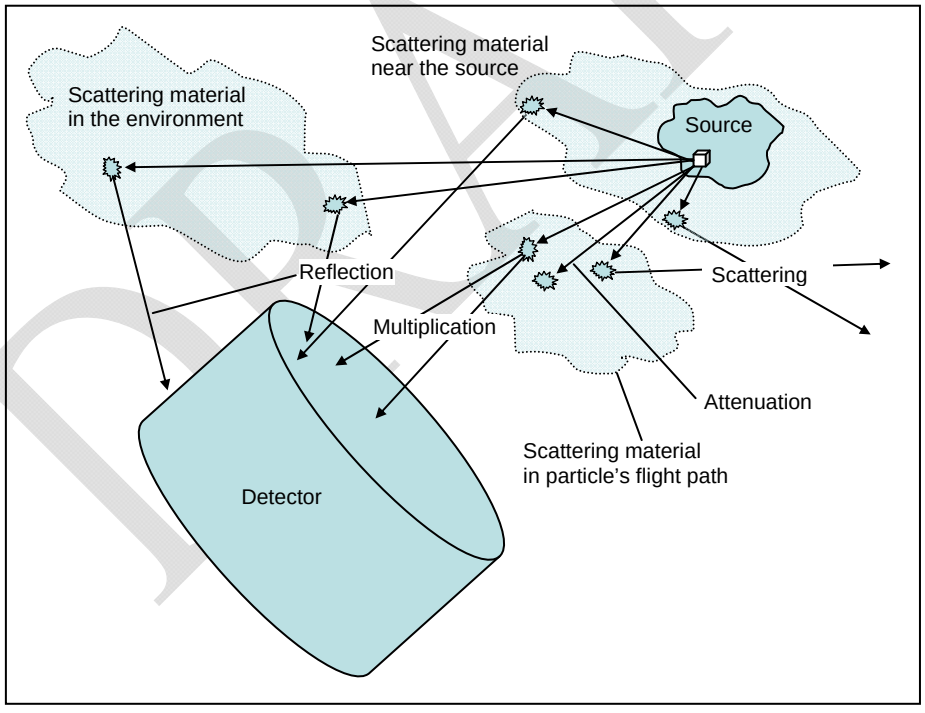

Figure 17: Examples of the various scattering processes that effect the absolute particle flux incident upon the detector.

2.1.2 Effects of environmental scattering on intrinsic efficiency

For the purposes of analyzing the effect that the change in particle flux has on experimental intrinsic efficiency, it is convenient to simplify our thought process by considering the effect that nuclear interactions have on the average energy of a large number of incident particles. Some majority nuclear interactions and their effects on both efficacy parameters are summarized below[20].

- **Attenuation:** Most materials preferentially absorb thermal neutrons.

Therefore, as attenuation becomes a significant effect, the spectrum is generally hardened. For the detector used in Figure 7 this increase in the average energy would cause an additional decrease in efficiency: $\kappa_{\Phi} < 1$ and $\kappa_{\gamma} < 1$.

[20] In the inequalities describing κ_{Φ} and κ_{γ}, the use of multiple symbols suggests the relative degree of the effect. For example, $\kappa_{\Phi} << 1$ might suggest that κ_{Φ} may be in the range $0.8 < \kappa_{\Phi} < 1$, whereas $\kappa_{\Phi} <<< 1$ may suggest $0.1 < \kappa_{\Phi} < 1$. In all cases these are merely generalizations, however, and by no means does this notation suggest universally applicable values.

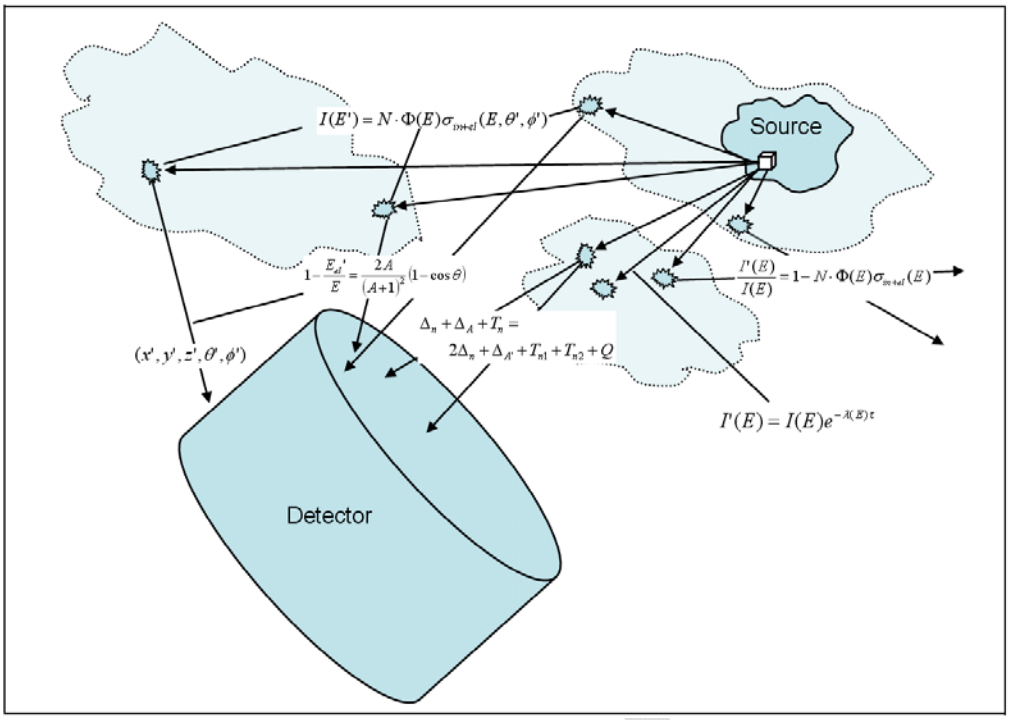

Figure 18: Effects of various scattering processes on energy spectrum and particle incidence.

- **In-flight scattering:** Neutron scattering cross-sections also globally decrease with energy for most elements, although not as universally as for attenuation. This is the case for long flight paths through atmosphere such as in standoff interrogation experiments. In this case the effect on the energy spectrum is much less significant: $\kappa_\Phi << 1$ and $\kappa_\gamma \approx 1$.

- **Near-source scattering:** This is a much more complicated situation, and can be the most difficult to accurately assess. Hydrogenous materials have a large scattering cross-section and also extract significant amounts energy from the source particles. For one example, if the source is, say, hidden in an oil drum, the flux is significantly increased because the drum has a solid angle of 4π for source particles and the detector has roughly the same solid angle for the drum and the source:

$\kappa_\Phi >>> 1$ and $\kappa_\gamma >> 1$. High-Z materials can have significant cross-sections but generally have a lesser effect on the particles energy: $\kappa_\Phi > 1$ and $\kappa_\gamma \approx 1$. Many middle-Z materials and a few high-Z materials have both large absorption cross-sections and large scattering cross-sections. If such materials are present, the flux and efficiency generally increases only slightly: $\kappa_\Phi > 1$ and $\kappa_\gamma > 1$.

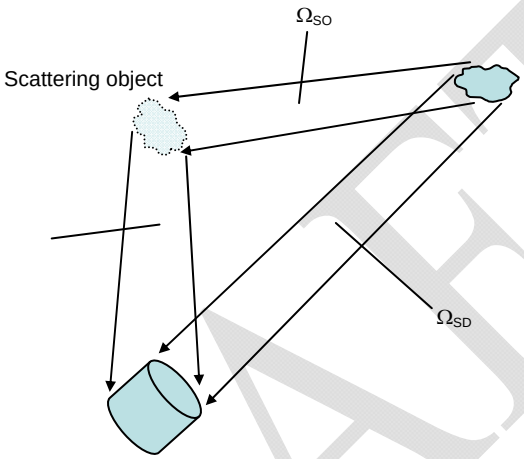

Figure 19: Determination of the flux efficacy factor for neutron-scattering objects in the environment.

- **Scattering from objects in the environment** is generally considered to be a source-induced background effect. For environmental objects, κ_Φ can be calculated directly. Assuming isotropic source emission and semi-isotropic reflection[21] from the object:

[21] The total solid angle of emission for particles reflecting from a surface is 1/2, or 2π steradians.

$$I_T = I\frac{\Omega_{SD}}{4\pi} + I\frac{\Omega_{SO}}{4\pi}\alpha\frac{\Omega_{OD}}{2\pi}$$

$$\kappa_\Phi = I_T \Big/ I\frac{\Omega_{SD}}{4\pi} \tag{2.2}$$

$$\rightarrow \kappa_\Phi = 1 + \frac{\alpha\,\Omega_{SO}\,\Omega_{OD}}{2\pi\,\Omega_{SD}}$$

where I is the source current, I_T is the incident current, Ω_{SD} is the source-detector solid angle, Ω_{SO} is the source-object solid angle, Ω_{OD} is the object-detector solid angle, and α is the albedo of the object. Of particular concern are extensive planar surfaces such as concrete floors and walls or the surface of the ocean for maritime applications. Figure 20 shows that the albedo for concrete is 0.5-0.8 in the neutron energy regime applicable to this work. The result of such high albedo is that most of the neutrons emitted from the source have multiple opportunities to interact with the detector.

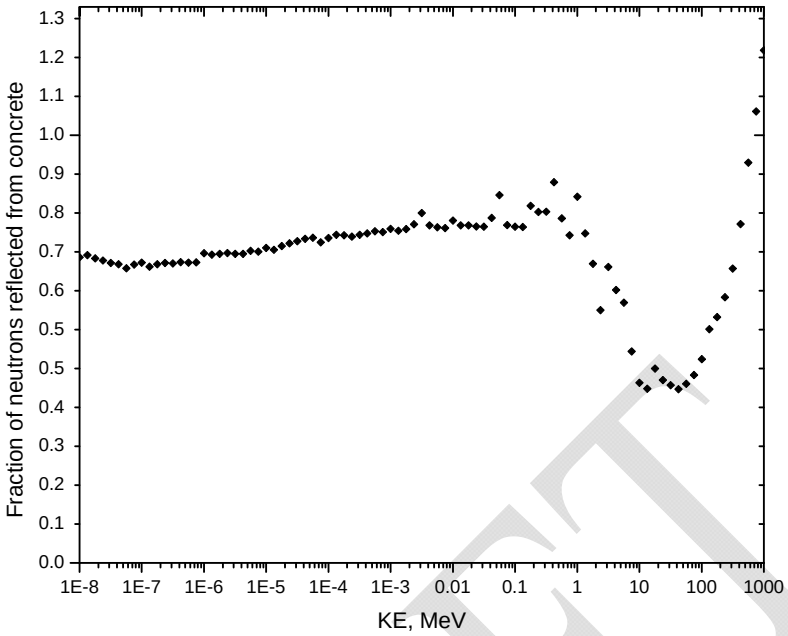

Figure 20: Neutron albedo from a thick concrete slab. The bumpiness is caused by scattering resonances in the constituents of the concrete. Notice the multiplication effect $(d\alpha/dE > 0)$ for E_n > 40 as the cross-section for (n, *x*n) reactions becomes significant. At even higher energies, interactions involving cascades of (n, *x*p*x*n) and (p, *x*p*x*n) reactions and (n, spallation) become possible and α eventually exceeds unity. [27]

2.1.3 Examples of efficacy calculations and discussion

Consider, for example, a He-3 detector having surface area 200-cm^2 located 1-m from an isotropic neutron source with the entire apparatus located 1m above a semi-infinite concrete floor and the source-detector axis parallel with the surface of the floor. Using (2.2) and taking $\alpha = 0.8$, $\Omega_{SD} = 200/100^2 = 0.02$, $\Omega_{SO} = 2\pi$, and Ω_{OD}=6.83E-3 [27], $\kappa_\Phi = 1.273 \pm 0.02$. Now move the detector to a 5-m distance from the source. Ω_{OD} decreases by about a factor of 10, to 7.04E-4 because the detector is further away from the part of the floor most strongly illuminated by the source. However, Ω_{SD} simultaneously decreases by a factor of 25, so the net result is a considerable increase in flux: $\kappa_\Phi = 1.704 \pm 0.03$.

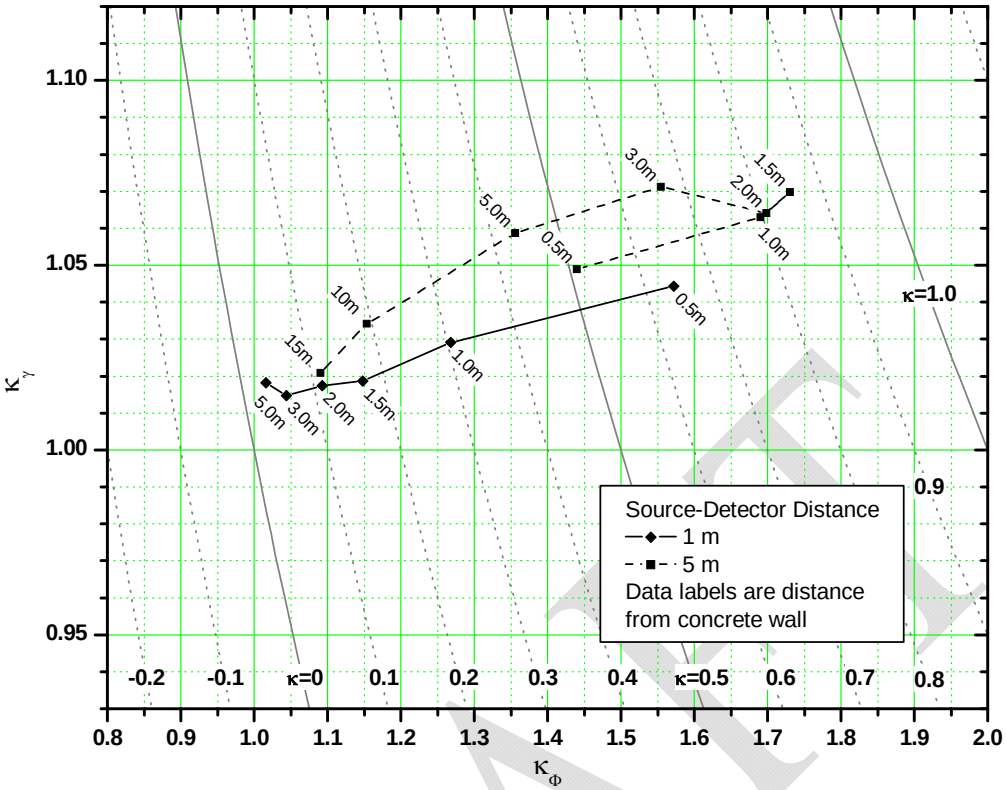

Figure 21: Effect of nearby concrete wall on detector[22] efficiency for an epithermal[23] neutron spectrum [27].

A suggested rule of thumb in the laboratory is to keep the efficacy (κ) below 10%. One would naturally expect the efficacy to decrease as the experimental apparatus is moved further from the wall. Figure 21 shows MCNPX calculations for the two experiments described in the preceding paragraph. Both 1-m and 5-m source-detector distances are presented for a wide range of wall distances. For a source-detector distance of 1-m, a 3-m distance from the wall is sufficient to meet the

[22] The actual detector model used was a 5-cm sphere of He-3 at 300-mbar surrounded by an 8-cm sphere of moderating HDPE. The neutron energy spectrum was uniform in probability from 100 keV-1 MeV. This paradigm is fairly representative of delayed neutron spectra being investigated at LANL by He-3 research detectors in terms of total efficiency and efficiency as a function of neutron energy.

[23] There are no universally-accepted neutron energy limits for the epithermal regime; for the purposes of this document the energy range will be defined as: $0.1eV \le E_{epi} \le 0.1MeV$.

$\kappa < 10\%$ paradigm. For a 5-m distance, the experiment must be moved >15m from the wall. In summary, for a single nearby semi-infinite wall, the necessary distance to minimize the efficacy effect is roughly 3 times the source-detector distance when the source and detector are less than a few meters apart, and it is somewhat greater than that for larger separations. Note that at such distances the efficacy is almost entirely due to the increase in flux; the energy effect (κ_γ) increases as the source-detector distance increases, but remains below ~110% in this scenario.

Interestingly, the 5-m source-detector distance data actually shows a *decrease* in efficacy for a wall distance less than 1.5m. This effect arises due to multiple scattering in the wall. As the source-detector apparatus gets closer to the wall, the average depth of the scattering point inside the wall becomes greater and the neutrons experience an increased probability of scattering away from the detector. The effect was also observed for the source-detector spacing of 1-m. The applicable wall distance was < 0.25-m in this case, and the data was omitted in the interest of readability.

Now consider the same two experiments placed inside a concrete room 10-m on a side. The neutrons are now confined on all sides and they can scatter from the walls multiple times. Using the facts that $\Omega_{SO} = 4\pi$ for particles emitted from the source and $\Omega_{S'O'} = 2\pi$ for wall-to-wall interactions and assuming equidistant walls and negligible fraction of neutrons absorbed in the detector on each "bounce", Eq. (2.2) can be modified thusly:

$$I_{Box} = I\frac{\Omega_{SD}}{4\pi} + \sum_n I\alpha^n \frac{\Omega_{OD}}{2\pi}$$

$$\rightarrow \kappa_{\Phi Box} = \kappa_{\Phi Wall} + \sum_{n>1} \frac{\alpha^n}{\Omega_{SD}} \frac{\Omega_{OD}}{} = 1 + \frac{\alpha}{1-\alpha}\frac{\Omega_{OD}}{\Omega_{SD}} \tag{2.3}$$

Comparing the second terms of Eq. (2.2) and Eq. (2.3), it is immediately apparent that the impact of the box on the flux is much more significant than a single wall alone—4 times greater for $\alpha = 0.75$! The energy effect is also increased, as the neutrons lose more and more energy as they continue to rattle around the room. Figure 22 summarizes the effects for various locations within a 7-m-tall box:

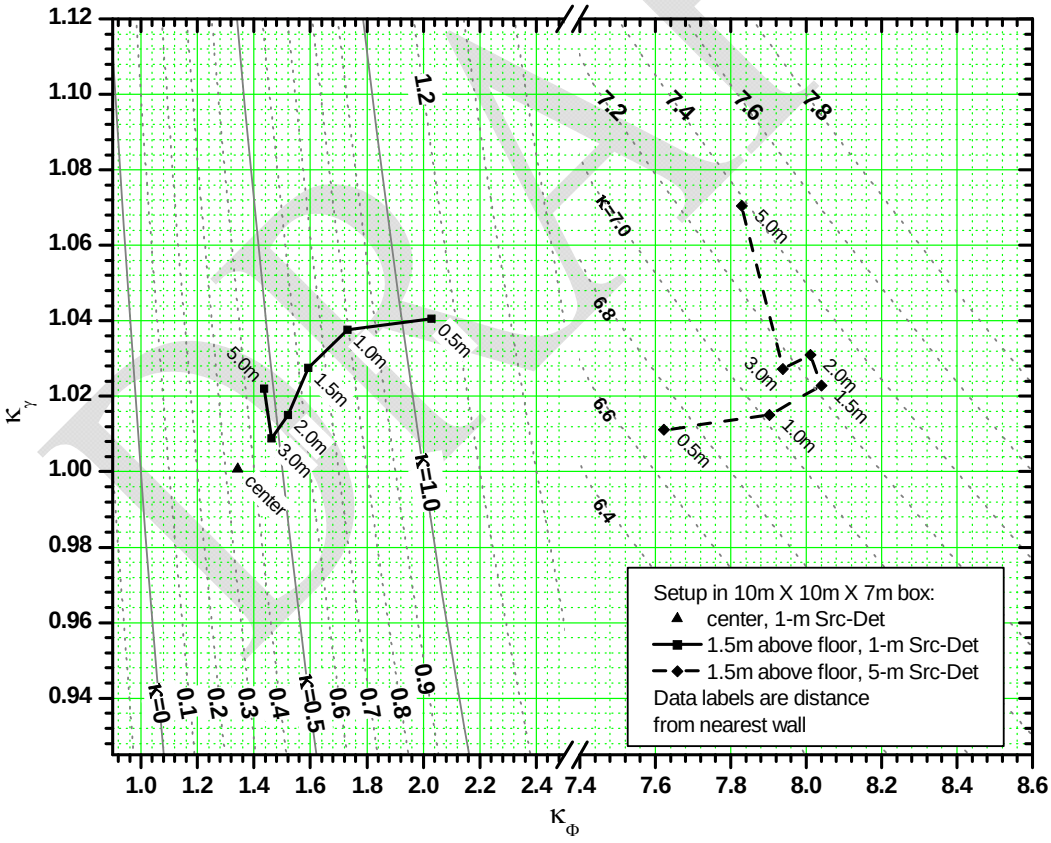

Figure 22: The effect on detector efficiency caused by placing the experiment inside a 10-m square by 7-m tall concrete box [27].

For comparison, the data from Figure 21 and Figure 22 are given in Table 2. The efficacy at the center of the box is 10 times greater than the single-wall case at a distance of 5 meters from the wall. For a detector 1-m from the source positioned 1.5m above the floor, the efficacy is increased by at least a factor of 2.5; this minimum increase logically occurs when the apparatus is in the center of the room. The magnification effect of the box increases to more than 6.5 times when the apparatus is very close to an adjacent wall. The effect is even more dramatic when the source-detector distance is increased to 5 meters—the efficacy is roughly a factor of 10 greater than the single wall no matter where you are in the room. The count rate in this situation is over *eight times greater* than if there were no walls present.

5-m from wall 1-m Src-Det	Center of box 1-m Src-Det	Distance to nearest wall in box, m	In Box 1.5-m above floor 1-m Src-Det	1.5-m from wall 1-m Src-Det	Distance to nearest wall in box, m	In Box 1.5-m above floor 5-m Src-Det	1.5m from wall 5-m Src-Det
		0.5	1.111		0.5	6.708	
		1.0	0.797		1.0	7.022	
0.034	0.343	1.5	0.637	0.169	1.5	7.223	0.718
		2.0	0.544		2.0	7.260	
		3.0	0.476		3.0	7.155	
		5.0	0.467		5.0	7.381	

Table 2: Values of efficacy (κ) for concrete wall and concrete box.

2.2 The neutron gas concept

Eschewing mathematical rigor, the situation can be conceptualized in an alternate fashion by envisioning a neutron gas being emitted by the source. Albedo neutrons are analogous to pressure waves being re-emitted from nearby objects, walls, etc. that they come into contact with. These waves, being comprised of uncharged particles, do not interact with each other and can be modeled as statistical

ensemble similar to an ideal gas [28]. A given experimental configuration thus creates a particular neutron gas flux-pressure gradient $\Psi(\vec{r},E)$ that the detector is subjected to in addition to the neutrons that travel directly from the source into the detector's acceptance. The flux-pressure gradient varies with position in both magnitude and energy spectrum. If the detector were rotated about the source, the direct flux would not change but the detector would be placed in a different flux-pressure scenario. On the other hand, if the distance from the source to the detector were changed, the direct flux would change but the flux-pressure would remain unaffected. In both cases, however, the neutron gas itself remains constant.

2.3 Closing remarks on efficacy

It can be impractical to calculate wall-to-detector solid angles with any appreciable accuracy on the fly in a laboratory setting. With practice, however, understanding of these relationships can be quite useful in determining what environmental factors must be considered and which can be neglected. More importantly, a thorough understanding can contribute invaluable insight into how much detail must be included in computer models to accurately reproduce the experiment.

The above discussion has considered the source to be entirely open and uncollimated. It is fairly easy to eliminate much of the efficacy effect by limiting the neutrons striking environmental objects through use of a neutron-absorbing collimator. Materials typically used for this purpose include polyethylene doped with boron, or b-poly, and outer sheets of Cadmium wrapped around inner layers of moderator (usually HDPE or b-poly). It is never possible to completely ignore

environmental effects in high-energy neutron-counting experiments no matter how well the source is collimated, however, as significant numbers of neutrons scatter from the front surface of the detector and pass through the detector entirely. However, through careful attention to details during the planning and construction phases of the experiment, environmental factors can usually either be reduced to negligible levels during the experiment or at least satisfied by simple additions to the geometry model used in the simulation.

Chapter 3 : Benchmarking Studies

The array design work was almost entirely performed with the monte-carlo radiation transport code MCNPX. It is important to have a solid understanding of the neutron scattering processes and the abilities and limitations of the code to accurately predict detector response before embarking on the array design. Therefore, a preliminary series of experiments was conducted to benchmark the code.

3.1 The MCNPX code

MCNPX is an extension to the MCNP code produced and maintained at Los Alamos National Laboratory. Development of MCNP and its parent codes dates back to the first nuclear reactor design work in the 1950's. MCNP is the most complete and accurate coupled neutron/photon/electron transport code in the world in its applicable energy range (0-20 MeV). MCNPX extends the capability of MCNP to include nearly all particles, including heavy ions, and much higher energies[24]. Development of both codes is ongoing and new features are continually being added. The relatively new addition of light-ion production from nuclear reactions is of particular interest. This gives the code the capability of producing and transporting the energetic daughter particles from several reactions. In this case it is the proton and triton from the ^{3}He(n,p)t reaction that are of interest. Transporting the daughter products allows for accurate representation of wall effects and also allows the user to specify a lower threshold in terms of total energy collected. This cutoff energy gives

[24] MCNPX does not define a maximum energy limit; however, care must be taken to ensure the applicability of the high-energy models used in the code. This should be considered on a particle-by-particle basis. A reasonable energy limit where this may start to become a consideration would be E > 10GeV.

the model slightly improved accuracy in predicting count rates, as it mimics the lower-level threshold used to remove electronic noise and contributions from other particles found in experimental helium-3 spectra.

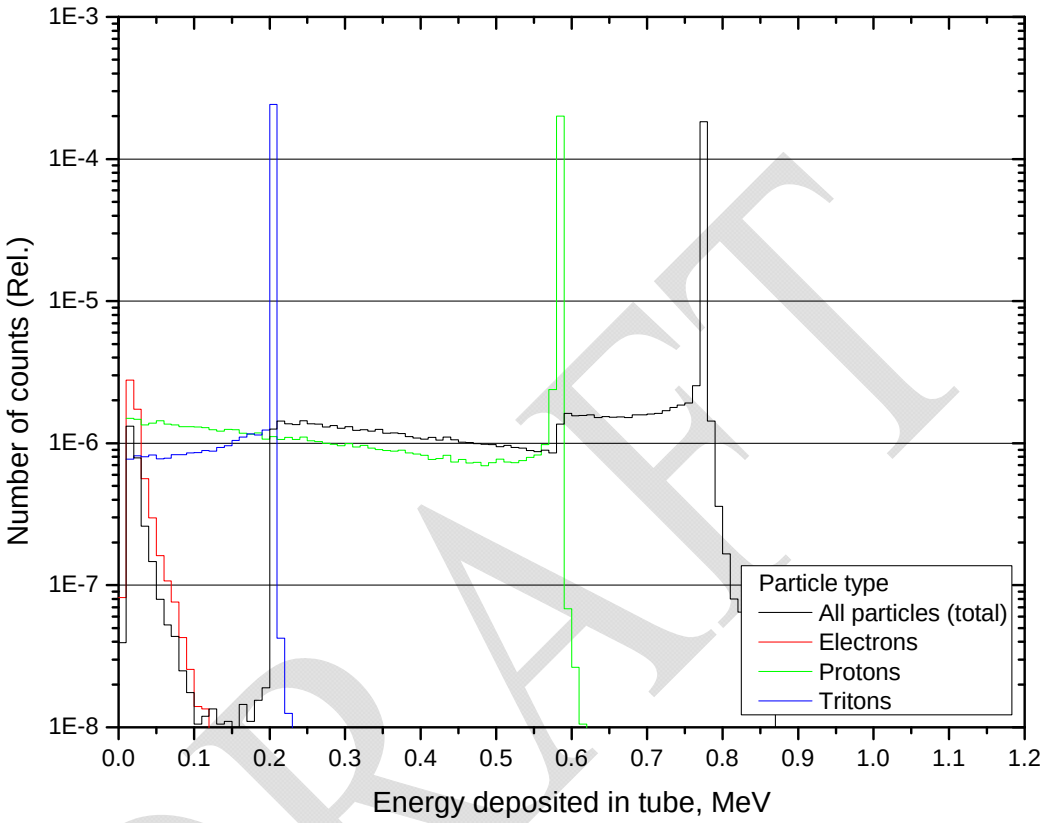

Figure 23: MCNPX pulse-height light[25] tally of energy deposited in He-3 tube from 3He(n,p)t reactions, broken down by particle type. The steps in the sum spectrum correspond to wall effects (see § 1.2.1.2). Notice that the peak in the proton spectrum is slightly shorter than that for the tritons; this shows that more protons stop in the wall because of their greater range. There is a clear threshold at about 190 keV above which all pulses can be considered to be produced by neutron capture events.

[25] The F8 tally with PHL option is referred to as a pulse-height light tally because it was originally intended for scintillator applications using energy deposition-to-light output KERMA factors. It works equally well for directly tabulating energy from charged particles by setting the KERMA factors to unity. Energy deposited by photons is not directly scored; the F8 PHL tally relies on creation of secondary electrons to track photon contributions.

3.2 Experimental setup

Three experiments were conducted to benchmark various aspects of the ANDY detector design: 1) albedo setup, which measured the efficiency of a He-3 counter versus thickness of HDPE layer behind the detector; 2) pressure setup, which measured efficiency versus He-3 partial pressure within the detector; and 3) diffusion/reflection setup, which measured the efficiency for a quasi-lattice detector consisting of a He-3 tube sandwiched between four stacks of alternating HDPE and air layers as the thickness of the HDPE layers was increased. All three experiments used 2" diameter by 12" long drift tubes constructed and filled at LANL. The fill gas was 1 bar total pressure containing a mixture of He-3 and proportional gas.

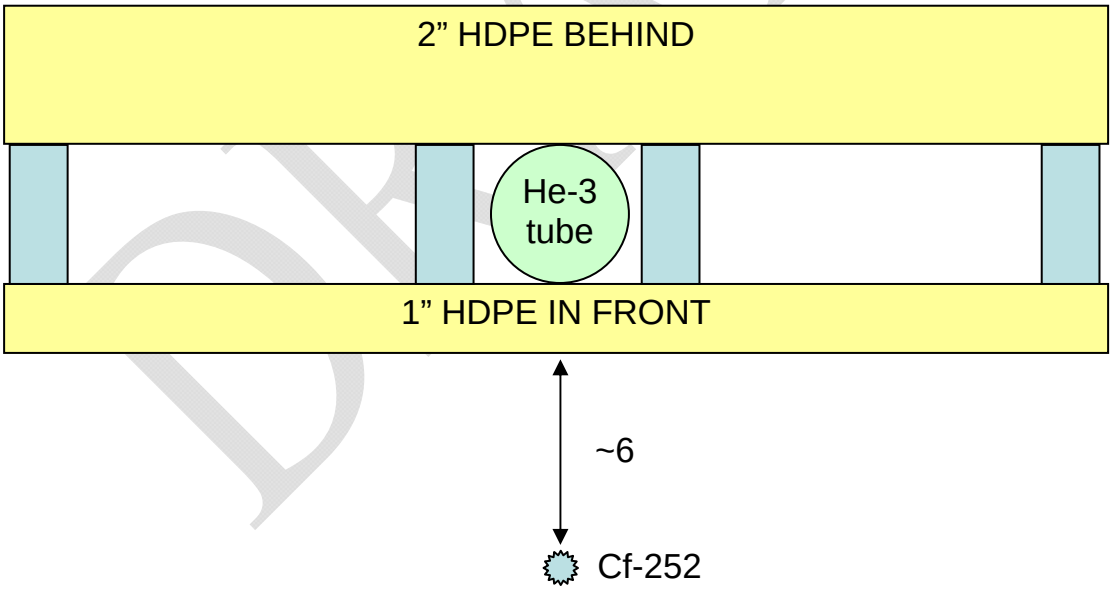

Figure 24: Setup for efficiency vs. He-3 partial pressure experiment

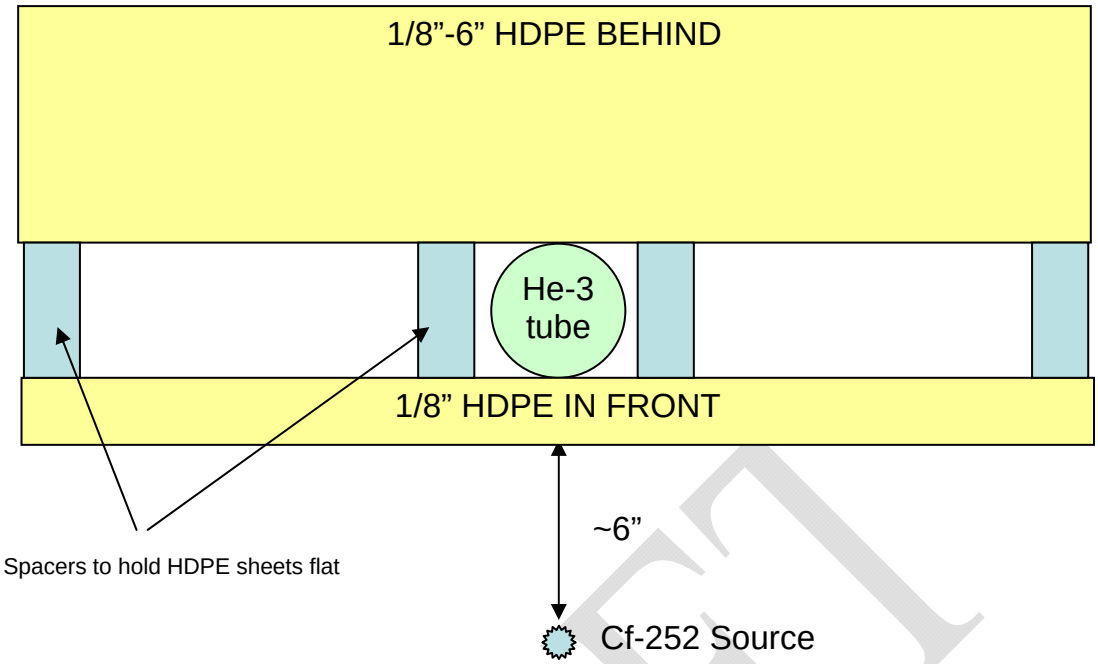

Figure 25: Setup for albedo experiment

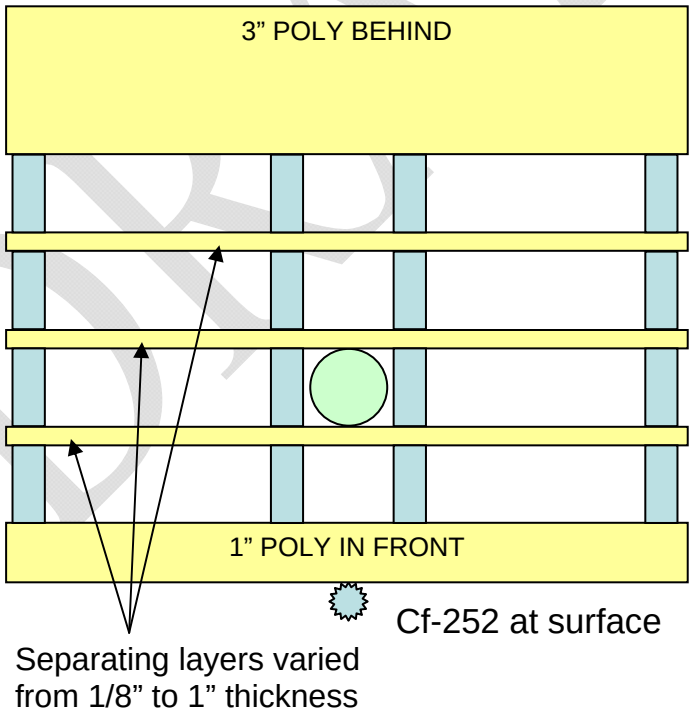

Figure 26: Setup for the diffusion/reflection (separator thickness) experiment

The experimental setups were intentionally designed in a minimalistic fashion to accentuate the desired effect and maximize repeatability. The setups generally consisted of HDPE sheets separated by cylindrical HDPE spacers to produce an air gap. The size of the HDPE sheets was 12” x 16” and the spacers were 1” diameter by 2-1/16” long. Holes 1/4" in diameter were drilled through the sheets and the center of the spacers and 1/4" HDPE rods were inserted through the entire setup to keep all layers properly aligned. The detectors were placed in the air gap lengthwise with the detector axis aligned parallel to the long side of the HDPE sheets. The center of the detector was aligned with the geometric center of the sheets. Four different Cf-252 sources were used in the experiments. Sources no. 208, 209, and 210 were cross-calibrated using source 108 as the standard. The results are shown in Table 3. The assumed uncertainty in the activity is 10%. The source capsules were cylindrical, 0.8-cm diameter by 1-cm long. The actual active volume of the sources is not known; a 1-mm dead layer in all dimensions was used in the model. The statistical error in the MCNPX runs was less than 1%; the data were assigned 5% error bars to account for approximations in the geometry definition. The manufacturer of the HDPE prescribed a range in density from 0.92-0.95 g/cm^3; the density used in the calculations was 0.93.

Source Number	Calibrated Mass, μg	Reference Date	Experiment Date	n emission rate, s^{-1}
108	1.0	6/1/1987	8/9/2008	13560
208	0.110	12/31/1988	8/9/2008	1492
209	0.214	12/31/1988	8/9/2008	2887
210	0.211	12/31/1988	8/9/2008	2853

Table 3: Cf-252 source data

3.3 Experimental results

3.3.1 He-3 partial pressure experiment

Three detectors were tested, containing He-3 at partial pressures of 50 mbar, 150 mbar, and 300 mbar. In the MCNPX models, tubes having >1 bar total pressure contained exactly 300 mbar of proportional gas. The self-shielding effect of the He-3 gas becomes readily apparent above 300 mbar as the slope of the curve becomes less than proportionality. The empirical data matches the MCNPX calculation exceptionally well within the 1-sigma error bars. It would have been desirable to measure tubes containing higher He-3 pressure (>=1 bar) in order to quantify the self-shielding effect of the helium-3. This was forgone at the time due to limited quantities of helium-3 available at LANL and multiple other experiments competing for the gas. Further experiments may be performed at a future date to expand the dataset and verify the code's predictions in the high-pressure regime.

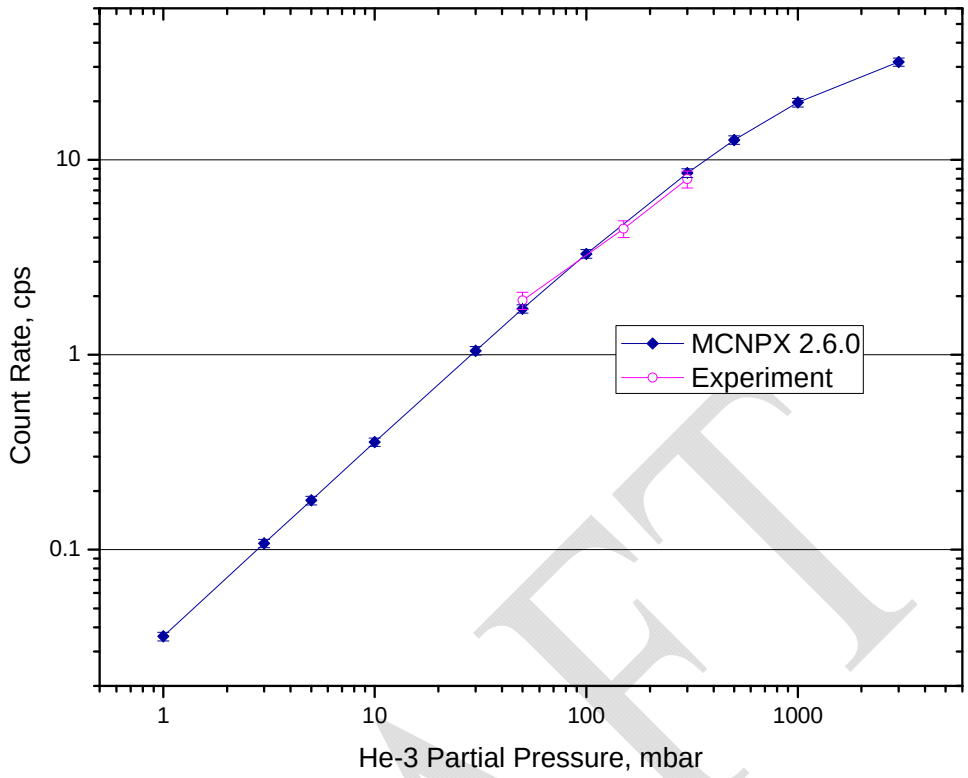

Figure 27: Results of He-3 pressure experiment

3.3.2 Albedo experiment

The purpose of the albedo experiment was to verify that MCNPX can correctly predict the increase in count rate from neutrons that backscatter from the adjacent HDPE slab. A 1/8"-thick front layer of HDPE was used for structural stability and to provide some initial moderation of the energetic Cf-252 fission neutrons. Figure 28 shows the excellent agreement between the code and experimental data. The deviation at the thinnest layers is due to poor signal-to-noise, which is -15dB for the thinnest layer (1/8", or 0.30 g/cm^2). The interior data points between 3/8" (0.90 g/cm^2) and 6" (14.48 g/cm^2) match within 1 sigma inclusively. There appears to be a slight deficiency (approx. 20%) in the MCNPX data at 2-3"

thickness (4.83-7.23 g/cm^2). It should be noted that the entire experimental curve is on average 9.0% higher than the MCNPX curve. This is within the uncertainty of the source activity and it can be treated as a systematic error. The deviation falls within the 1-sigma error bars after applying this renormalization to the experimental data.

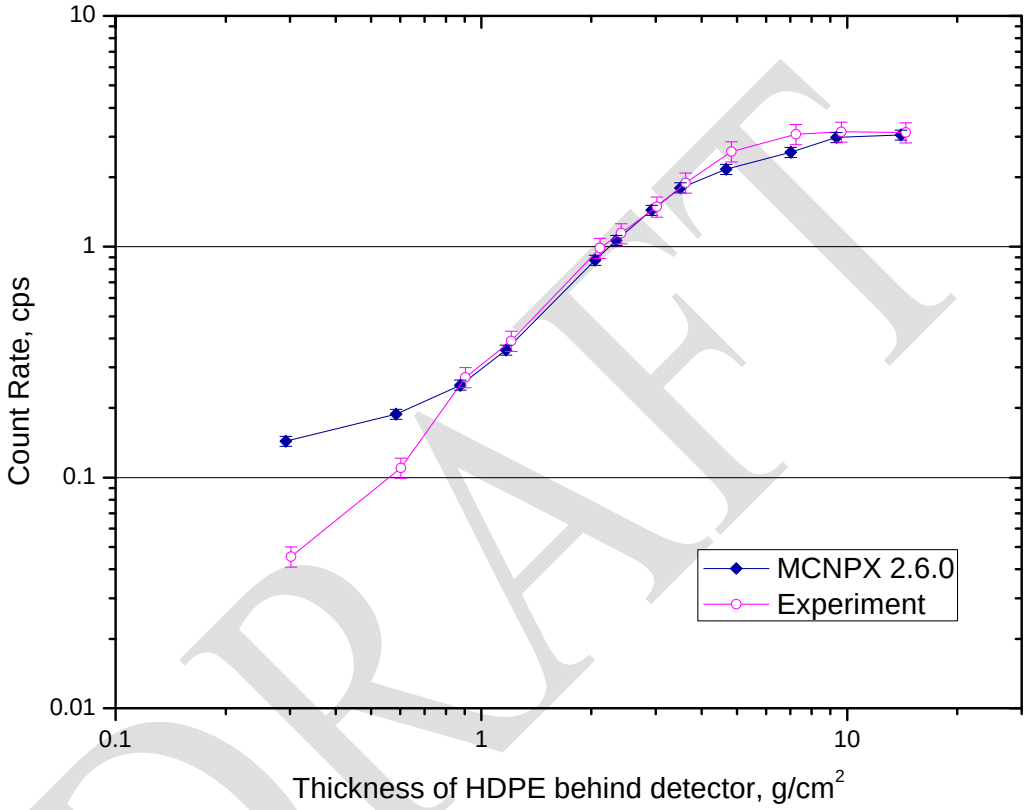

Figure 28: Results of Albedo experiment

3.3.3 Diffusion/reflection experiment

The diffusion experiment represented an attempt to reproduce the effect of the neutron "trap" created by the HDPE lattice. The simple design allows the separator layers to be easily switched. This facilitates the study of varying separator thickness while eliminating the need to manufacture multiple lattices. The data matches

exceptionally well within error, although the slope of the MCNPX curve does seem to exhibit a slightly greater increasing trend than the experimentally measured values. The difference in slope is not statistically significant; however, the systematic trend is suggestive that a systematic error may be present. The most likely error is that the assumed value of 0.93 for the HDPE density is incorrect. Ultimately, the results presented here are quite satisfactory. They also suggest that great care should be taken for future experiments that require increased sensitivity; greatly influential parameters such as the density of hydrogenous materials should perhaps be verified with an independent measurement.

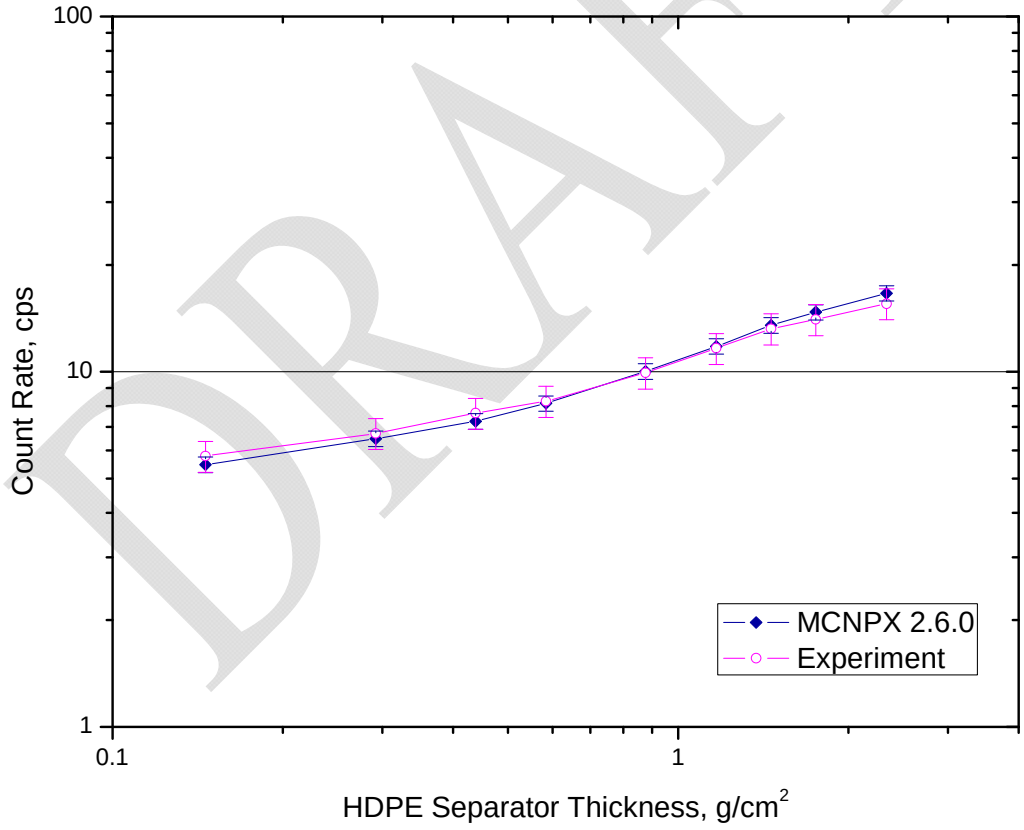

Figure 29: Results from separator thickness experiment

3.4 Conclusion of benchmarking studies

The Monte-Carlo code MCNPX provides highly accurate predictions of helium-3 detector response for many experimental setups involving polyethylene as the primary constituent. By extension, the code can be assumed to perform very well for pure Carbon as well. The code was shown to be quite sensitive to small modifications in the setup, and it is logical to presume that it will be quite sensitive to small environmental changes as well. Therefore, much care must be taken in modeling such experiments; not only to accurately define the pieces that make up the experimental apparatus, but also to adequately identify and characterize neutron-scattering objects in the environment.

Chapter 4 : Detector array optimization

The optimization work presented here is intended to lay a general groundwork for application-specific designs of ANDY-type detectors. Therefore, a thorough investigation of a uniform[26] rectangular HDPE lattice was performed. Different configurations may prove fruitful for enhancing efficiency; some suggestions are made at the end of this chapter. The ANDY concept provides a rich canvas for inspiring creativity and imaginative design; such tasks are left to the designers of real-world implementations. Throughout this chapter, the source used was a quasi-plane wave[27] of Cf-252 neutrons impingent upon the entire front face of the detector, including the outer walls.

4.1 Fundamental principles and parameters

Limiting the scope of the study to the above paradigm allows for a complete scientific analysis. The analysis is further simplified by setting the thickness of the four outer walls and rear slabs to the albedo-limited thickness[28] of 9.5 g/cm^2 (see Figure 16). The only remaining parameters to optimize are the thicknesses of the front moderating slab, the sidewalls, and the separators.

[26] The term uniform refers to the fact that all the sidewalls are the same thickness throughout the lattice, as are all the separators, etc.

[27] The source was uniformly distributed in position and was given initial momentum in a narrow cone having a 1-degree opening angle and central axis perpendicular to the face of the detector.

[28] Throughout this chapter the density used for HDPE was 0.95.

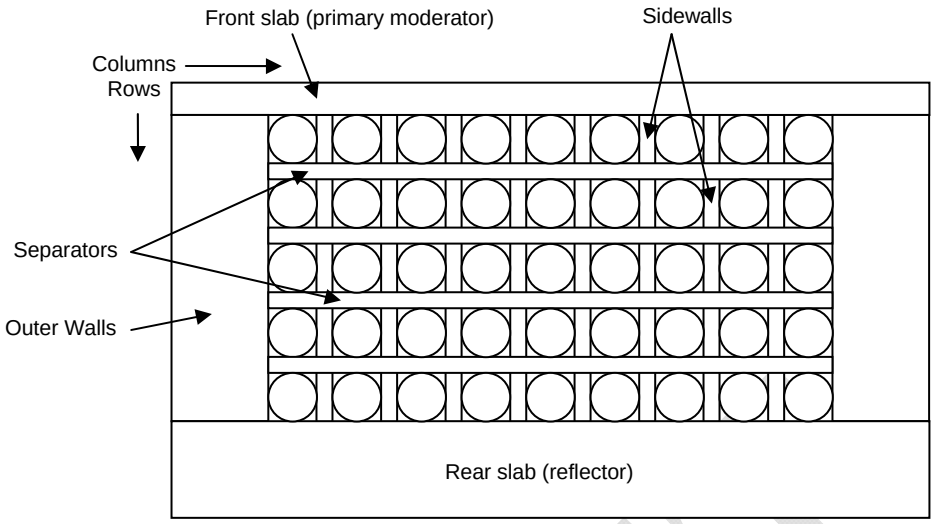

Figure 30: Diagram of an ANDY-type detector, specifying parameters to be optimized.

4.1.1 Total efficiency figure-of-merit

A figure-of-merit (FOM) is defined in order to properly compare detectors of different sizes. The FOM is the intrinsic efficiency normalized to one liter He-3 at STP present in the detector. The FOM is also geometry-normalized by multiplying by the surface area. A weighting factor *m* is included to control the relative emphasis between efficiency and amount of He-3 used:

$$FOM_{[m]} = \left(\overline{\varepsilon_I}\right)^m \cdot A/V \qquad (4.1)$$

where A is the surface area of the detector and V is the STP volume of helium-3 present in the detector. Referring to Eqs. (1.7) and (1.8) on page 15, it is readily apparent that, for *m*=1 this expression is proportional to the total efficiency times $4\pi R^2 \Omega_{SD}$. It is thus referred to as the total efficiency figure-of-merit. Note that because the magnitude of $FOM_{[m]}$ depends on the intrinsic efficiency raised to the factor *m*, comparison of $FOM_{[m]}$'s having different *m* is meaningless. To prevent this

mistake, *m* is always denoted as a bracketed subscript. The units are $m^2/L \cdot sr$. It is impossible to quantify the dimensionless factor *m*; henceforth the units are referred to as 'arbitrary.' The usefulness of this figure-of-merit is that it is invariant with the number of detectors used in the experiment (assuming zero cross-talk between detectors); therefore it permits direct comparison of the effectiveness of different detector designs.

4.2 MCNPX simulations

Before proceeding with the optimization process, a baseline was obtained by performing a simple study optimizing the response of a single high-pressure tube containing 3 bar He-3 inside a rectangular parallelepiped of high-density polyethylene.

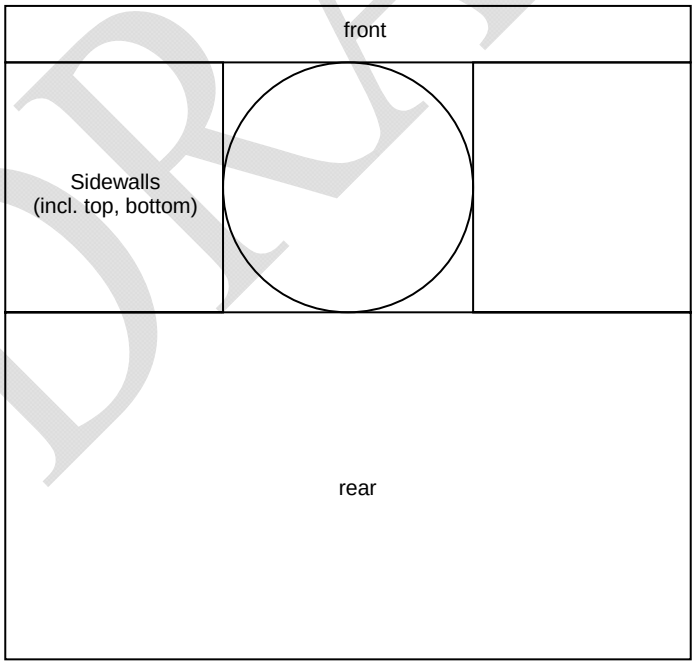

Figure 31: Single He-3-tube detector used for baseline comparison.

4.2.1 Baseline data: single He-3 tube

The tube used in the baseline simulation was 5-cm in diameter and 300-cm in length, containing approximately 17.3 L_{STP} (0.77 mol) He-3. The thickness of the back reflector was chosen to be 9.5 g/cm^2 and the front moderator 0.95 g/cm^2. The thickness of the four outer sides was varied from 1.9 g/cm^2 to 28.5 g/cm^2. The results appear in Figure 32.

The efficiency for the 3-bar tube reaches a maximum at about 9.2% at 4.75 g/cm^2-thick outer walls. An interesting phenomenon occurs as the wall thickness is increased beyond this point; the efficiency falls off, but the surface area simultaneously increases. The increase in surface area initially dominates, resulting in an increase in $FOM_{[1]}$. As the sidewall thickness is further increased, the two competing factors ultimately reach an impasse and $FOM_{[1]}$ saturates at about 33.3 above 12.35 g/cm^2. This presents an interesting scenario to applications such as neutron radiation monitoring: concrete is a very effective neutron moderator and it is typically used extensively in laboratories; therefore the most efficient use of the detector is to embed the radiation monitor directly into the walls and/or floor of the facility!

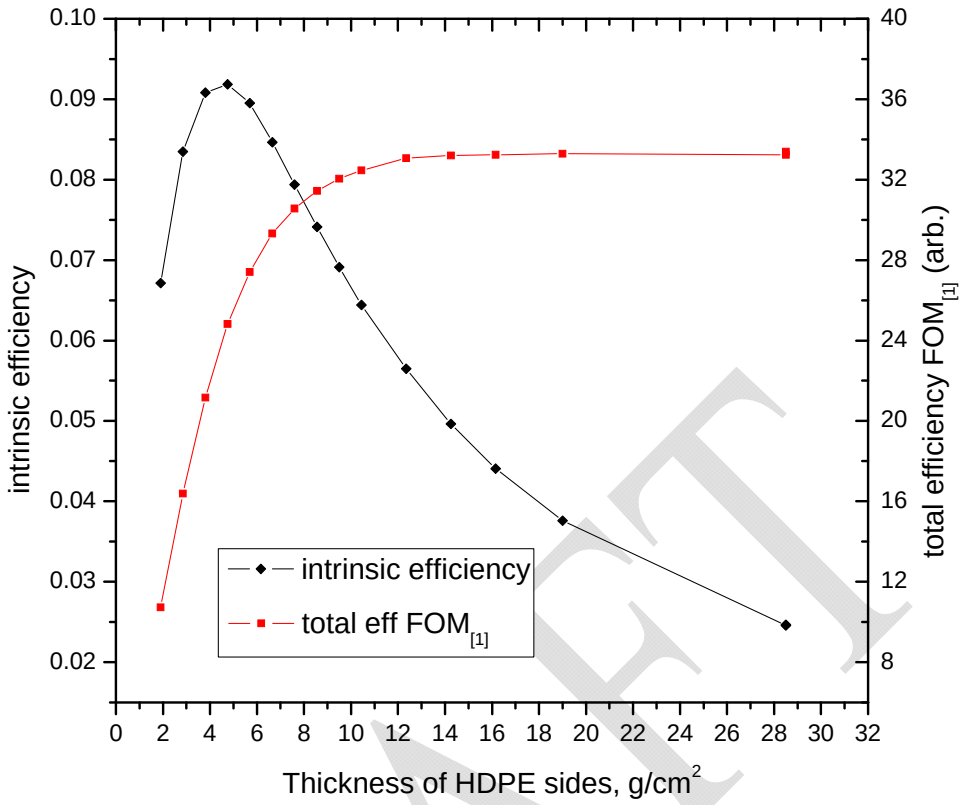

Figure 32: Intrinsic efficiency and total efficiency figure-of-merit for a detector consisting of a single He-3 tube.

4.2.2 Optimizing the design of the rectangular ANDY detector

The detector size was chosen to be 320-cm wide (approx.) by 320-cm tall by 20 rows deep. This is an adequate size to minimize fringe effects from the edges of the detector and thus is representative of a semi-infinite implementation. The tubes were 5-cm in diameter and 300-cm long. These dimensions are suitable to many homeland security applications while maintaining relevance to the laboratory regime. The exact width of the detector varied slightly as the sidewall thickness was changed. The number of columns in the detector was determined by choosing the odd number that made the interior width nearest to 300 cm. Using this convention there is always

a column of tubes centered on the vertical bisector of the detector. The goal of these choices was to maximize consistency of the detector's response as other detector parameters are changed. Initial parameters were chosen to be 0.95 g/cm^2 separator thickness and zero sidewalls. The detector contained 59 columns of tubes in this configuration.

4.2.2.1 Front thickness optimization

The front face of the detector plays two important roles: (1) it provides initial moderation of the incoming fast neutrons, which increases the detector's efficiency, but (2) it also reflects a significant portion of the incident neutrons via albedo. The loss from albedo predominates, and the detector begins losing efficiency at a front thickness of only 1.425 g/cm^2. The maximum value reached by $FOM_{[1]}$ is approximately 23.0; about 31% less than that for the single tube. This does not cause concern at this point, as the 20-row model was never assumed to be an optimal design; it merely highlights the fact that ANDY concept cannot be extended to an indefinite number of rows. The optimal front face thickness was chosen to be 1.5 cm. This thickness results in about 2% less than peak efficiency for this particular configuration; however, the additional thermalization should prove beneficial in the final step--optimization of the number of rows.

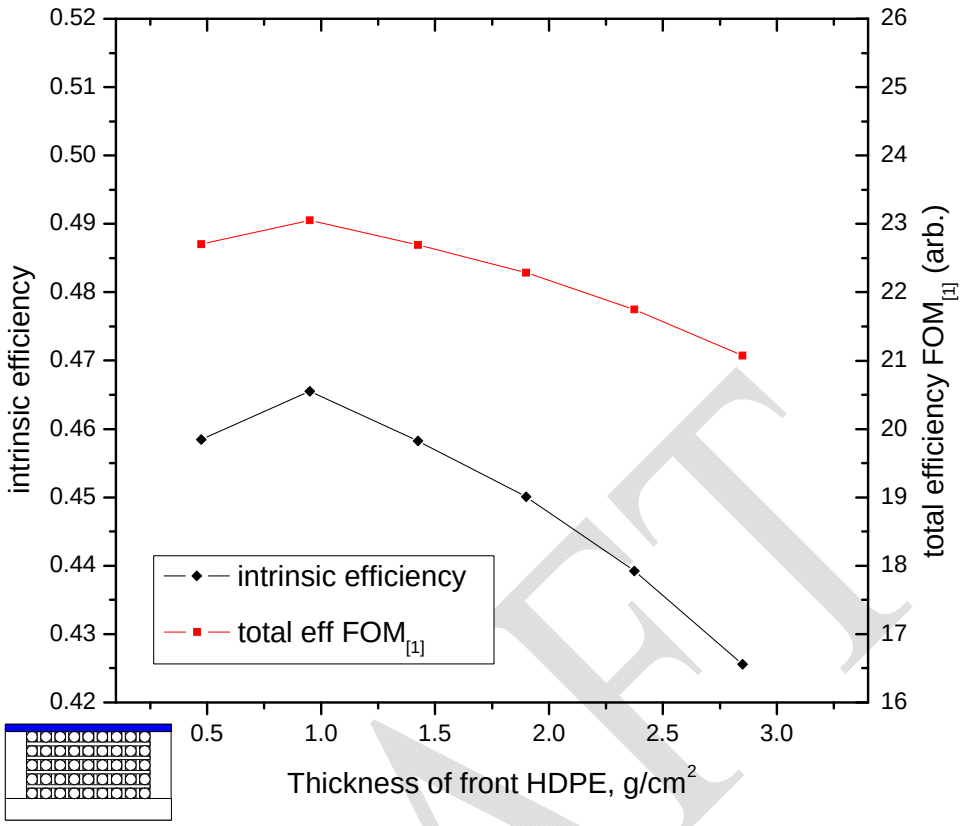

Figure 33: Efficiency parameters vs. thickness of front face. The surface area is constant throughout this comparison, and the two curves are identical in shape.

4.2.2.2 Sidewall thickness optimization

The effect of increasing the sidewall thickness is much as one would expect: the additional thermalization provided by the sidewalls is completely overwhelmed by neutron loss to capture on hydrogen: H(n, γ)d, and the efficiency drops monotonically. However, recall that the width of the detector is kept as near to 320 cm as possible. Because of this, the number of He-3 tubes in each row is simultaneously decreasing as they are supplanted by slabs of HDPE. This results in a net increase in $FOM_{[1]}$ that produces a broad peak near 0.7125 g/cm^2 sidewall

thickness. The number of columns and the associated detector dimensions are summarized in Table 4.

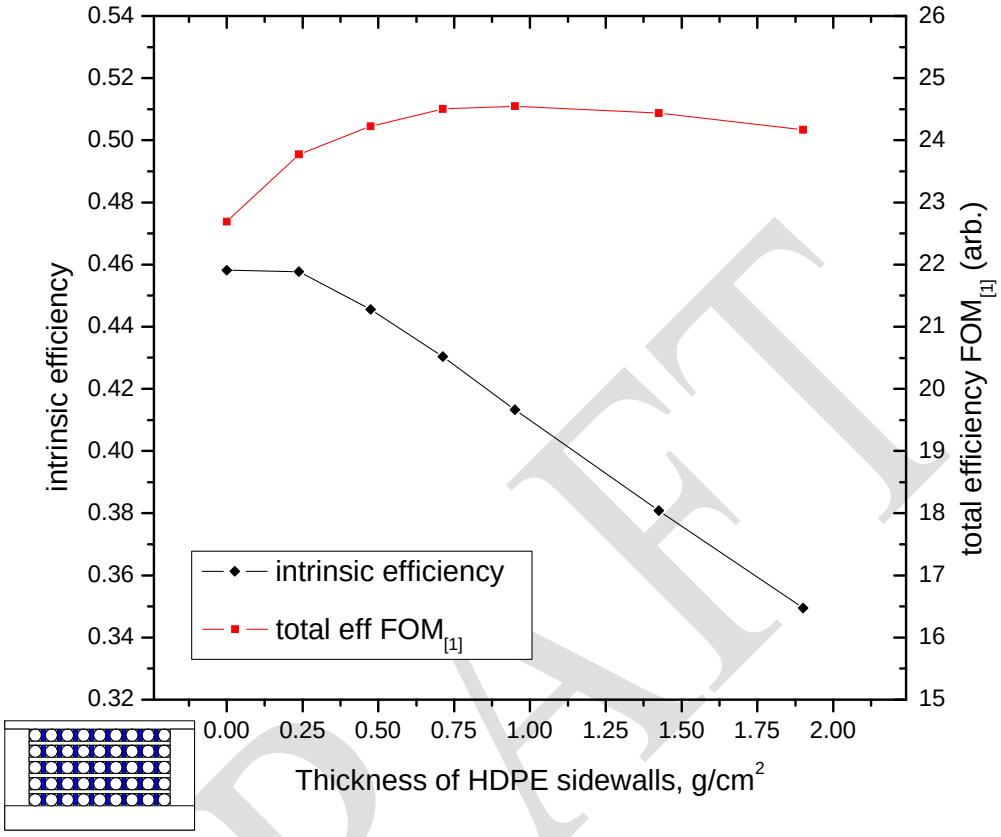

Figure 34: Efficiency parameters vs. sidewall thickness

Sidewall thickness, cm (g/cm^2)	Columns	Total width, cm	Surface Area, m^2
0.00 (0.0000)	59	316.18	10.12
0.25 (0.2375)	57	320.39	10.25
0.50 (0.4750)	55	323.60	10.36
0.75 (0.7125)	51	314.27	10.06
1.00 (0.9500)	49	314.98	10.08
1.50 (1.4250)	47	326.44	10.45
2.00 (1.9000)	43	321.86	10.30

Table 4: Number of columns and detector dimensions vs. sidewall thickness.

4.2.2.3 Separator thickness optimization

The results for the separator thickness study show a peak at 0.475 g/cm^2 separator thickness. The peak occurs at a fairly thin value because of the semi-infinite nature of the lattice; the outer HDPE box and the gas in the tubes do a fairly adequate job of trapping and thermalizing the neutrons by themselves. Increasing the amount of HDPE in the lattice creates an initial efficiency increase because of improved thermalization; however, beyond a certain point the losses due to increased albedo and neutron capture on hydrogen dominate. The optimum thickness chosen to use in the array depth study was 0.7125 g/cm^2; just as in the study of the front face thickness, the minor loss in efficiency for the 20-row detector is expected to be offset by improved thermalization for lattices containing fewer rows.

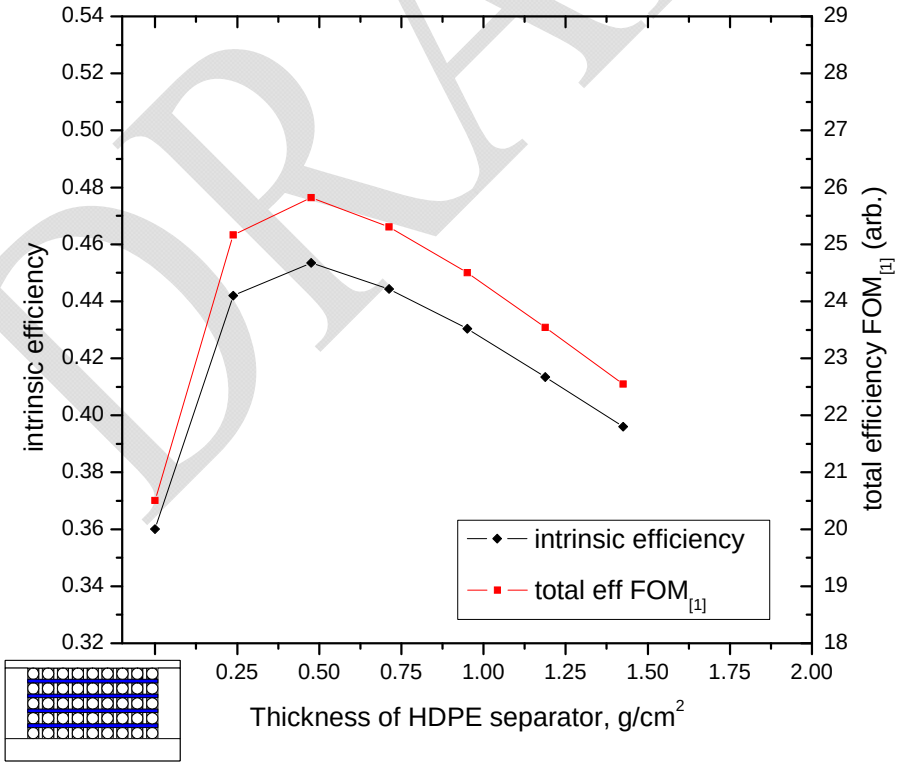

Figure 35: Efficiency parameters vs. separator thickness

4.2.2.4 Row-by-row study of the separator results

Before proceeding to the array depth study, the results of the preceding section were analyzed on a row-by-row basis. In Figure 36, each data point represents the sum of an entire row of detectors. Row 1 is at the front of the detector, and row 20 at the back. For zero separator thickness, the count rate is fairly flat with a slight bias toward the front rows of the detector. The frontward bias becomes more predominant as the separator thickness increases. Generally speaking, rows 2-3 experience the greatest count rate and the count rate decreases dramatically toward the rear of the detector. This is a clear demonstration of the lattice concept at work: for a well-moderated ANDY detector, a significant fraction of the incident neutrons are trapped and thermalized in the first few rows. The neutron flux steadily decreases through absorption and leakage through the walls of the detector as the neutrons diffuse into the deeper rows, and the count rate drops accordingly. This suggests that only a few rows of tubes may be necessary to achieve the desired efficiency. The optimal figure of merit will likely occur at even fewer rows.

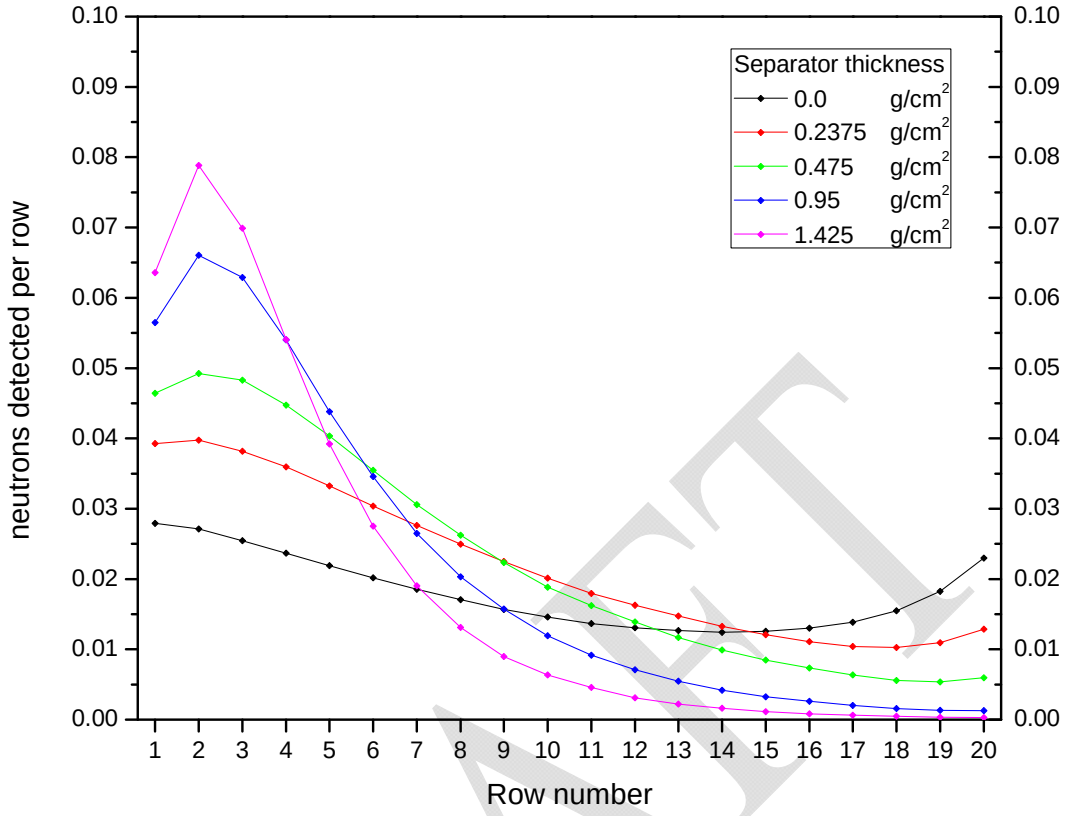

Figure 36: Row-by-row efficiency of the semi-infinite ANDY detector. Each line corresponds to a certain separator thickness, and each point on the line represents the sum of all the detectors in that row.

4.2.2.5 Array depth optimization

Figure 37 was produced by modeling several detectors, each containing a specified number of rows of tubes. The lattice parameters were identical in each case: 9.5 g/cm^2 in the outer sides, top, bottom, and rear; 1.425 g/cm^2 in front; and 0.7125 g/cm^2 in the separators and sidewalls. The results show that 20 rows are nearly sufficient to reach maximum possible efficiency and 90% of saturation efficiency is reached at only 10 rows. Furthermore, the efficiency for a single row is nearly equal to that of the optimized single high-pressure tube. While the efficiencies are comparable, the 1-row ANDY design enjoys a huge advantage over the single tube in terms of $FOM_{[1]}$. This is because each tube in the ANDY array only contains 1/10 the gas of the single tube; therefore the ANDY detector occupies a much greater solid angle relative to the amount of helium-3 in the detector. In this particular arrangement, the ANDY detector has 21.5 times the surface area of the single-tube detector but only uses 5.1 times as much helium-3, resulting in an increase in $FOM_{[1]}$ of 2.97--nearly 3 times the total efficiency per unit gas! This result clearly demonstrates the wasteful nature of vintage He-3 detector designs.

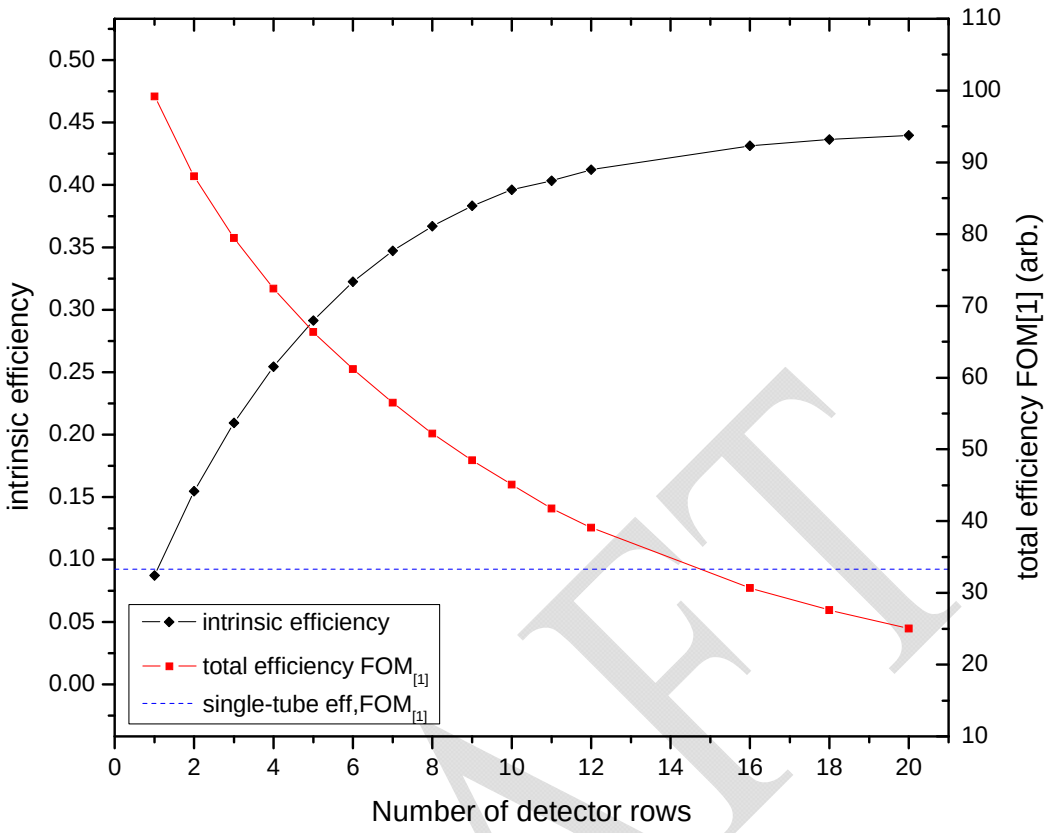

Figure 37: Efficiency parameters versus number of detectors rows for rectangular ANDY detectors. The results from the single high-pressure tube of section 4.2.1 appear as a dashed line for comparison; the two y-axes were aligned so the efficiency and figure-of-merit for the single-tube coincide.

The figure-of-merit results are initially surprising in that the maximum occurs at a single row. This initially appears to be in disagreement with the results of section 4.2.2.4, which suggested that the peak should have occurred at two to three rows. As shown in Figure 38, reanalyzing these results on a row-by-row basis reveals the discrepancy: the row-by-row efficiency increases monotonically towards the rear of the array for detectors having only a few rows. However, $FOM_{[1]}$ is based on the *average* efficiency of all the rows, which monotonically decreases. The monotonic increase in efficiency toward the rear is partly a result the high albedo of the thick

rear reflector, but is also due to insufficient thermalization that stems from the constant-thickness front moderator and separators that were used throughout this microstudy. To demonstrate this, the four-row ANDY detector was re-optimized to obtain maximum efficiency. The results are presented in Figures 39-41.

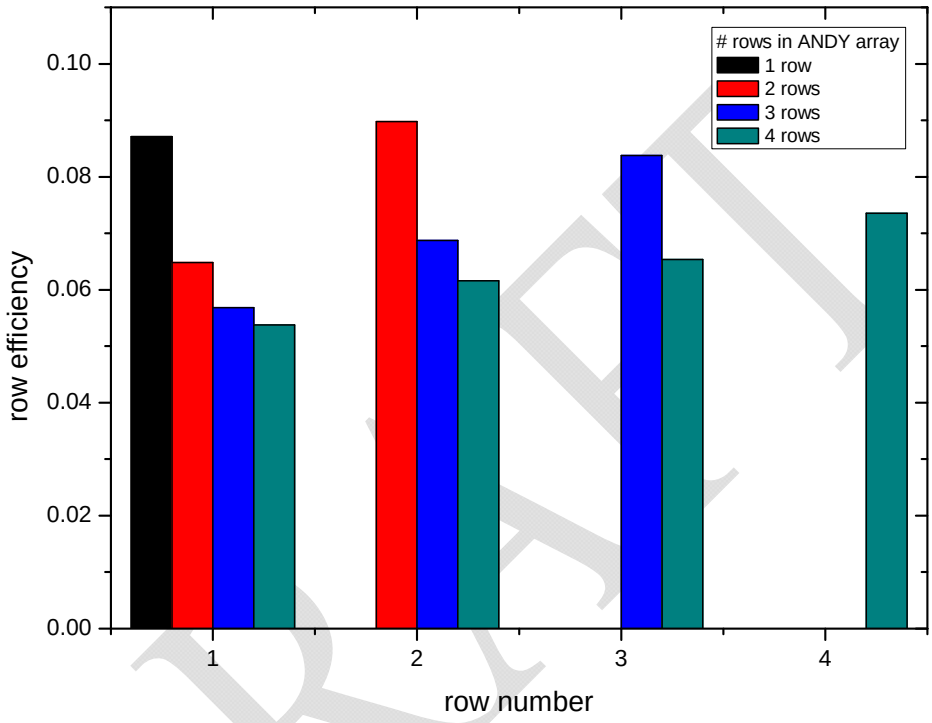

Figure 38: Row-by-row analysis of ANDY arrays containing only a few rows. As always, row 1 is the front row.

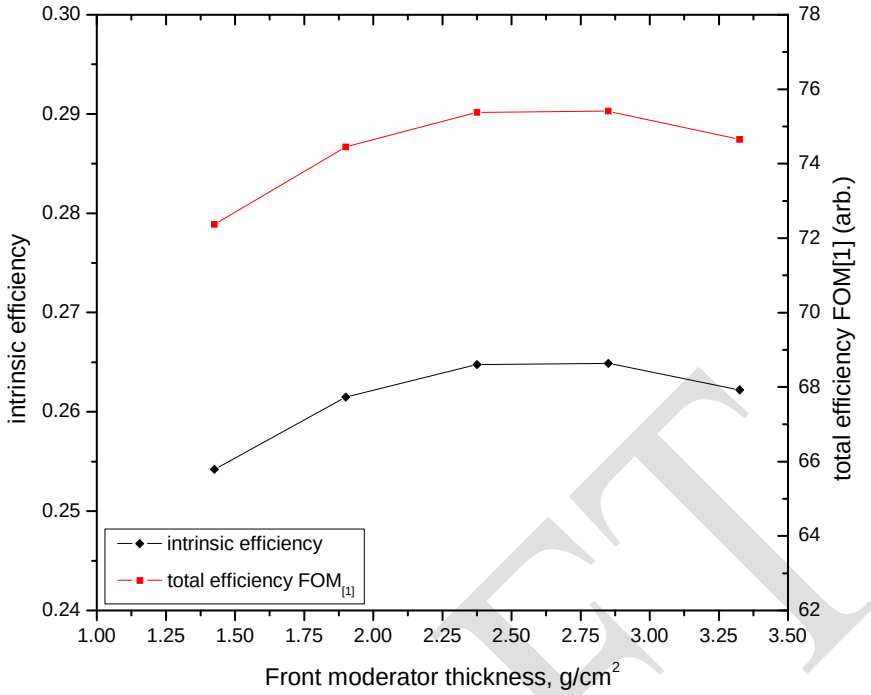

Figure 39: Optimizing the front moderator for the four-row ANDY lattice.

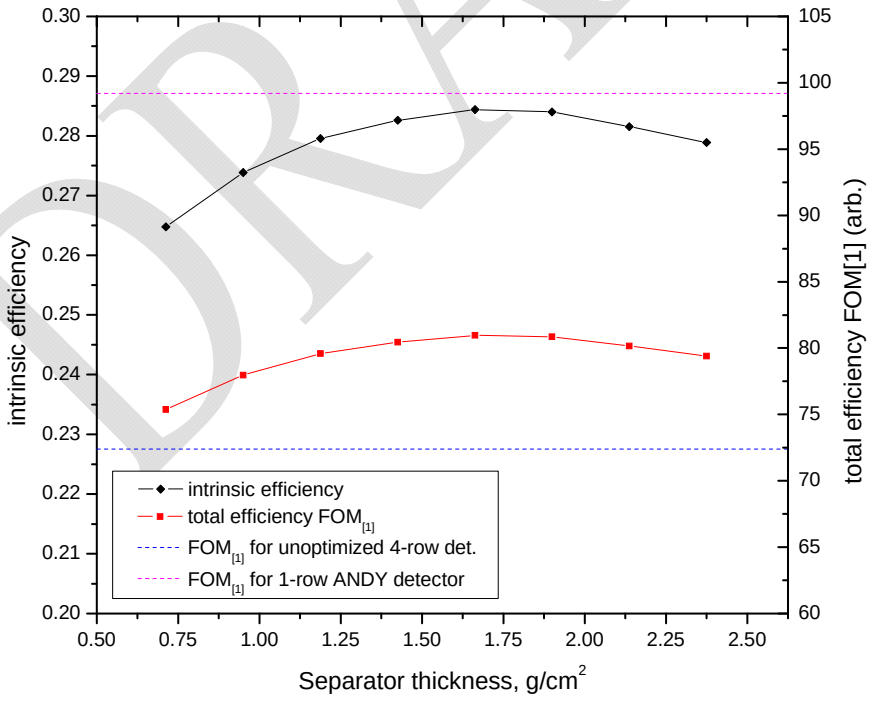

Figure 40: Optimizing the separators for the four-row ANDY lattice.

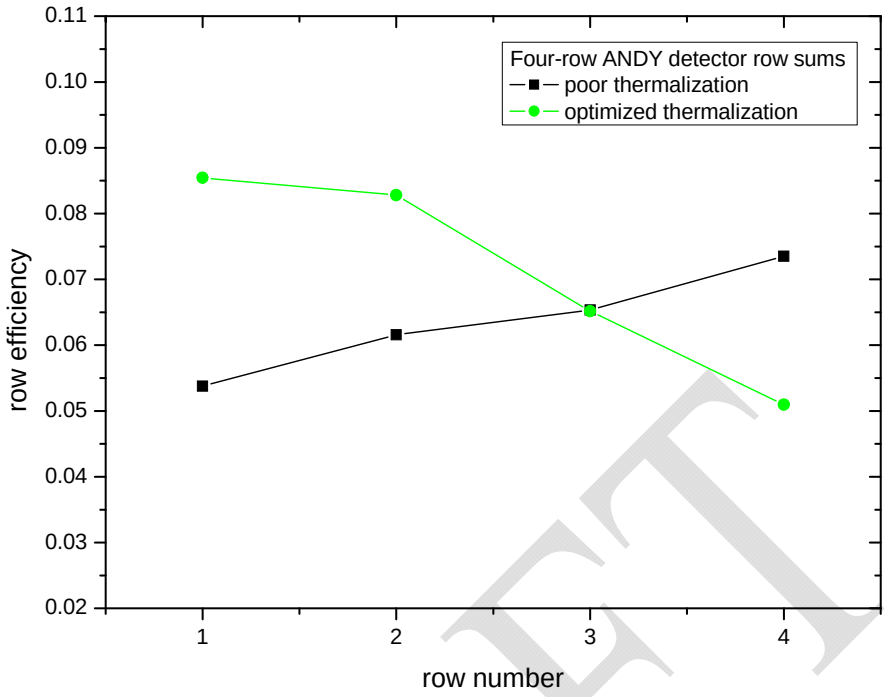

Figure 41: Row-by-row comparison of four-row ANDY detectors: poorly thermalized and optimally-thermalized.

Optimization of the four-row detector resulted in a 12% gain in efficiency. This is certainly a significant gain; however, the value of $FOM_{[1]}$ of 80 is still well short of the single-row ANDY detector, which appears as a dashed line in Figure 40. This microstudy shows that both the front moderator and the separators were too thin in the configuration used in Figure 37; this is not surprising considering that those parameters were optimized for a much deeper array. Figure 41 shows that the difference in the location of neutron capture events after optimization is dramatic—the slope of the row-by-row efficiency curve is completely inverted! Rows 1 and 2 have nearly identical efficiency in the optimized array. While these results are not intended to be all-inclusive, they do provide insights that will be quite valuable to designers of real-world ANDY arrays. However, the analysis of these results is not

yet complete; recall from section 1.4 that many experimental scenarios call for increased emphasis on efficiency. Applying this concept to the ANDY array has a significant impact on the lattice dimensions, as section 4.3 will demonstrate.

4.3 Applying the results to real-world configurations

The implication of the results presented in Figure 37 when applied to real-world scenarios is clear: from the purest standpoint of maximum utilization of the He-3 gas, a single row of detectors is optimal. Any required increase in count rate should be realized by adding additional detectors to the ends of the array. However, this solution may not be desirable for many applications due to space constraints or aesthetic and/or logistic considerations (consider, for an extreme example, a detector 18-cm deep and 100m long!). Thus it will frequently be preferable to increase efficiency by adding additional rows to the detector. From a design standpoint, this scenario is equivalent to stating that the intrinsic efficiency is more important than the solid angle. This can be realized mathematically by adding a *second* weighting parameter, *n*, to the figure-of-merit expression:

$$FOM_{[mn]} = \left(\overline{\varepsilon_I}\right)^{m \cdot n} \cdot A/V \qquad (4.2)$$

Obviously, Eq. (4.2) is mathematically equivalent to (4.1); however, both *m* and *n* are retained to emphasize the fact that the two weighting factors should be kept separate conceptually. Combining *m* and *n* into a single parameter could result in under-emphasis of the intrinsic efficiency. For example, a weighting factor of 3 represents a fairly extreme bias, and a practical-minded designer may be tempted to reduce the factor. However, the results of this strong single bias are identical to the results given

by the product of the two conservative factors m=1.5 and n=2, which represent a slight bias toward efficiency compared to the amount of gas used and only a moderate bias relative to the surface area of the detector, respectively. Therefore, $m \cdot n = 3$ does yield the desired result.

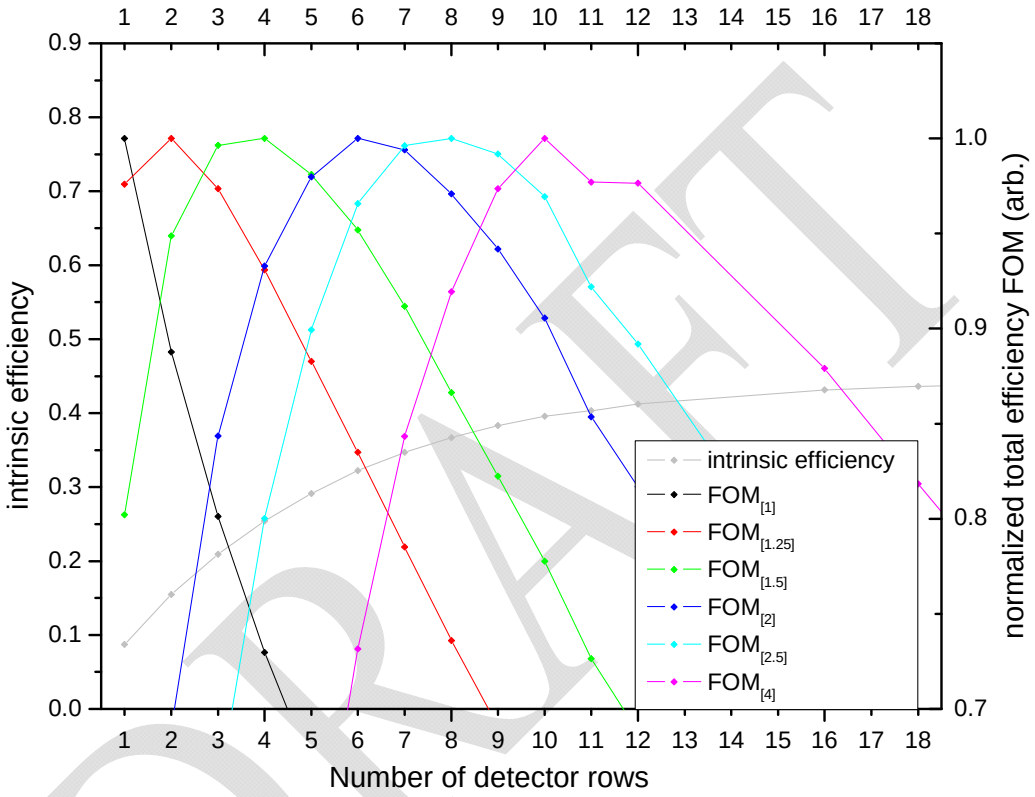

Figure 42: Weighted efficiency parameters for ANDY detectors for various efficiency scenarios.

For most real-world applications, m and n are both expected to be modest; the total weighting factor $m \cdot n$ will typically lie in the range 1.5-2.5. Figure 42 shows that the optimum number of rows in these circumstances for the array consisting of tubes containing 300-mbar helium-3 is 4-8. This corresponds to an intrinsic efficiency of 30-35%. The reader should keep in mind that while the 300-mbar level

is considered a good starting point for demonstrative purposes, the true optimum may involve more or less partial pressure of He-3 gas. The study of this final application-dependent optimization parameter is left to the designer.

Comparing the weighted figure-of-merit results to the old-style single-tube detector shows that the single tube initially gains ground as the emphasis on efficiency is increased (see Figure 43). However, when cost is truly no object (represented by the regime $m \cdot n > 3$), the ANDY design is even more dominant than the purist viewpoint ($m \cdot n = 1$). This remarkable result suggests that virtually any real-world detector design could be improved by implementing the ANDY concept.

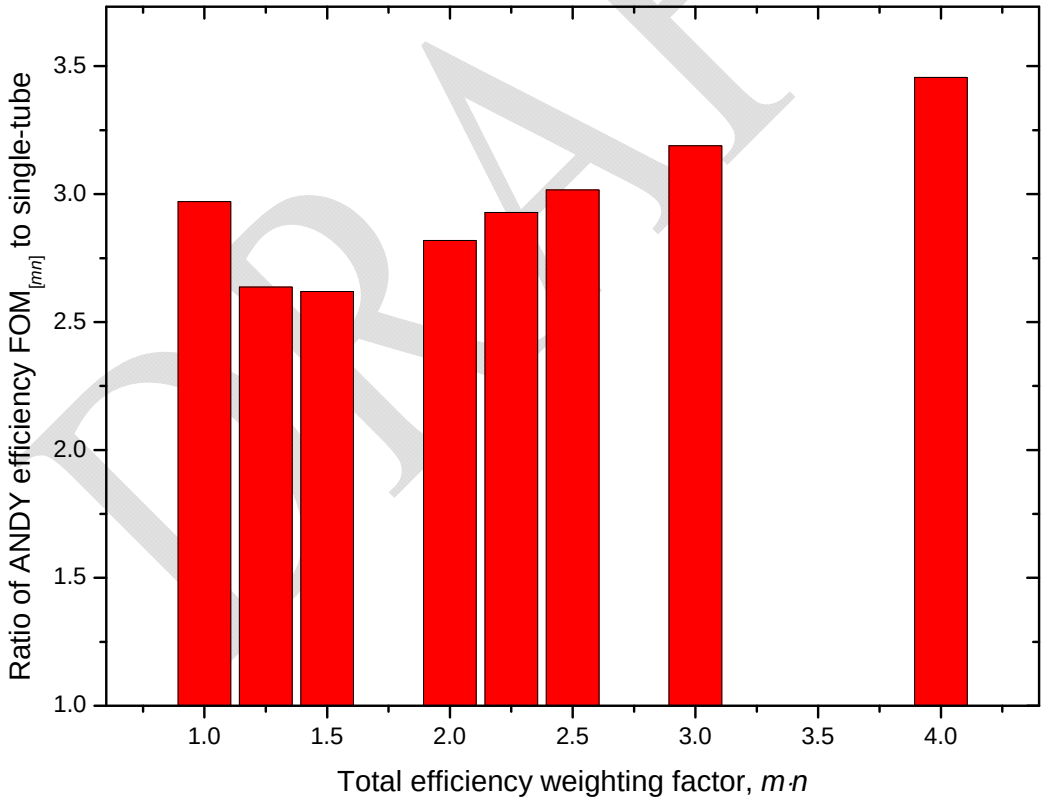

Figure 43: Improvement in total efficiency figure-of-merit for ANDY detector over single-tube detector for various efficiency-weighting scenarios.

Chapter 5 : Prototype development

A prototype detector was constructed at LANL for the purposes of benchmarking the results of Chapter 4 and providing a portable high-efficiency, large-area neutron detector suitable to conducting future standoff interrogation experiments at LANL and Brookhaven National Laboratory (BNL). The final design represents a compromise between cost, portability, recommended dimensions of the lattice, and efficiency required by the experiments.

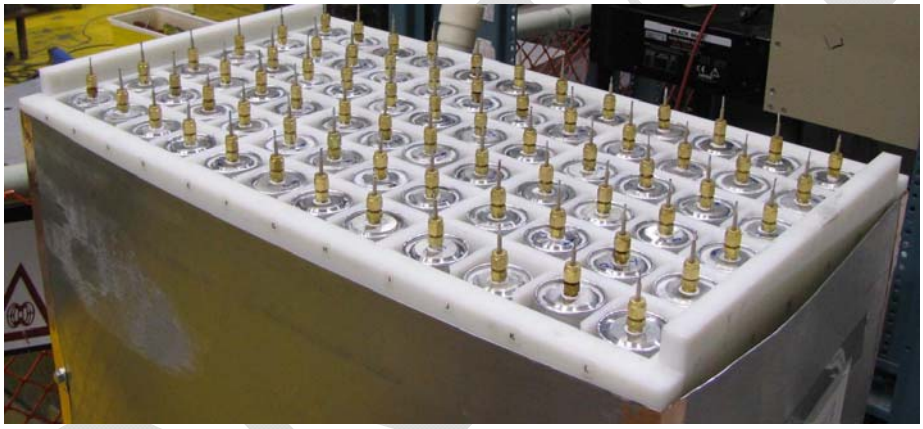

Figure 44: The ANDY prototype detector in the laboratory at LANL

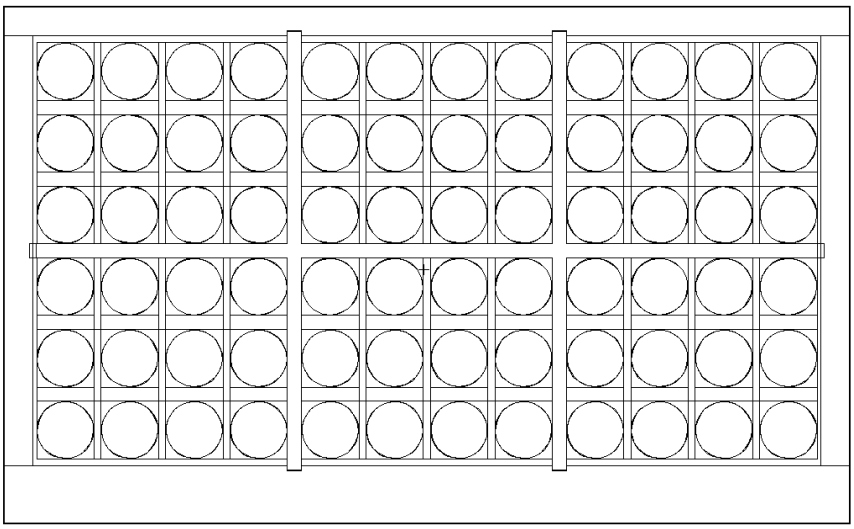

Figure 45: MCNPX model of the ANDY prototype. The top face in the MCNPX model is the front face.

5.1 Detector construction

The helium-3 detectors were built at LANL using a design emphasizing robust and inexpensive construction. The basis for the design was one that has been used successfully for constructing proportional counters up to 6.1-m in length for the ongoing development of a muon radiography and tomography system at LANL [45, 46, 47]. The detectors consist of an aluminum tube 5.08-cm in diameter that has been sealed at both ends with welded aluminum caps. The central wire is 35-micron diameter gold-plated tungsten stretched to 50g tension. The dual anode connections (top and bottom) are provided via copper tubes 0.15875-cm in diameter that are crimped onto the central anode wire. Thus the tubes can readily be adapted to position measurements using the time difference between the signals arriving at the two ends. The anodes are insulated from the housing by polyetheretherketone (PEEK) tubing.

Swagelok fittings inserted through threaded holes in the caps provide airtight seals at the Swagelok-PEEK and PEEK-anode interfaces. One end of the tube has a tee and a second Swagelok fitting. This fitting holds a second copper tube that provides the gas interface (not pictured). The ground connection is made by tightly looping copper wire around the Swagelok fitting at the small gap between the base of the fitting and the cap. The simplicity of this design allows the detectors to be easily assembled using off-the-shelf equipment at a fraction of the cost of retail industrial detectors.

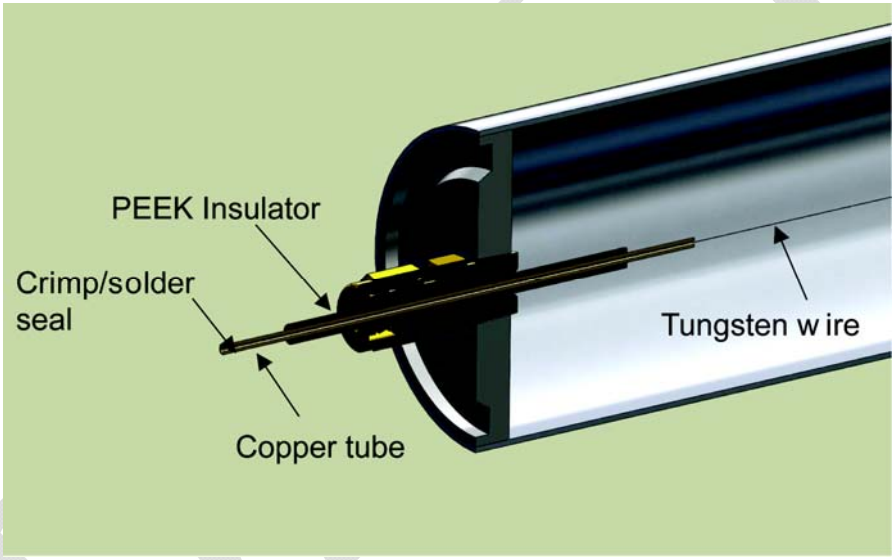

Figure 46: Schematic view of detector construction.

After the tube assembly is complete, the gas-fill and quality control processes are conducted simultaneously in an integrated fashion. First, the tension in the anode wire is verified with a vibration test. In this test, a magnet is placed near the detector to create a magnetic field gradient. The wire is caused to vibrate by gently striking the tube with a knuckle or rubber mallet. The fundamental frequency of the wire's vibration is proportional to the square root of the tension in the wire. The wire's

motion through the magnetic field induces an oscillatory electrical signal in the wire. The frequency of oscillation is measured with a digital oscilloscope that has built-in fast fourier transform (FFT) capability (Tektronix TDS3000B or similar). Several harmonics are excited during this test. The precision of the measurement can be increased to better than 1% by fitting several of these harmonics.

Next, the detectors are connected to a custom-built gas filling station that allows up to 60 tubes to be filled and leak-checked simultaneously. The first step in this process is leak checking with ordinary Helium. During the leak checking process the tubes may also be subjected to an evacuation and heating cycle, which assists in the removal of outgassing impurities. The tubes are then high-voltage tested to 5000V to insure proper isolation of the anode wire before adding the fill gases. The proportional gas is a proprietary mixture of ethane (C2H6), tetraflouromethane (CF4, industrial designation R14), and Argon. The gas is ordered premixed and arrives in a standard welding-size (approx. 50L water volume) cylinder. Helium-3 is ordered in much smaller quantities and is typically stored in cylinders about 1L in water volume. Following the leak check, the tubes are evacuated and the helium-3 is inserted. The helium-3 is added first to avoid pollution of the remaining He-3 in the cylinder. Next, the helium-3 cylinder is closed off from the rest of the system and the proportional gas is added. Using this method it is impossible to prevent some loss of helium-3 into the proportional gas cylinder. The loss is minor, however, because of the large pressure difference between the filling station and the gas cylinder, and is generally negligible. After the desired pressure is reached, the copper fill tube is crimped closed and trimmed. The tip of the tube is then given a secondary seal with a layer of

solder. A final leak check is performed by immersing the tips of the copper fill tube and anode tubes in water. If no bubbles form, the tube is ready to go into service.

5.2 Array construction

The prototype consists of 72 helium-3 tubes arranged in a 12 x 6 rectangular lattice. Per the results of Chapter 4, this lattice emphasizes efficiency fairly strongly. Portability was also a significant factor in choosing the dimensions; the detector is typically placed on a wheeled cart and the 12 x 6 lattice provides enhanced stability as it is rolled about the laboratory. Each tube is 5.08-cm in diameter, 121.92-cm long, and contains 200 mbar He-3 and 800 mbar proportional gas for a total internal pressure of 1 bar. The outer walls were selected to minimize weight while not unnecessarily sacrificing efficiency. The top, bottom, front and side HDPE slabs are 2.54-cm thick and the rear is 5.08-cm. The top and bottom slabs are drilled through to allow the anode connections and fill tube to pass through. There is a 3.81-cm air space and additional 2.54-cm base below the bottom slab. The open space is reserved for custom electronics that will be installed at a future date[29]. The top area is open save for six aluminum project boxes that provide connection points for high voltage and ground wires. The entire detector is encased in a 0.762-mm thick aluminum faraday shield to reduce electronic noise.

[29] Planning for the electronics-addition project is currently underway; it is slated to begin in June 2009, pending funding.

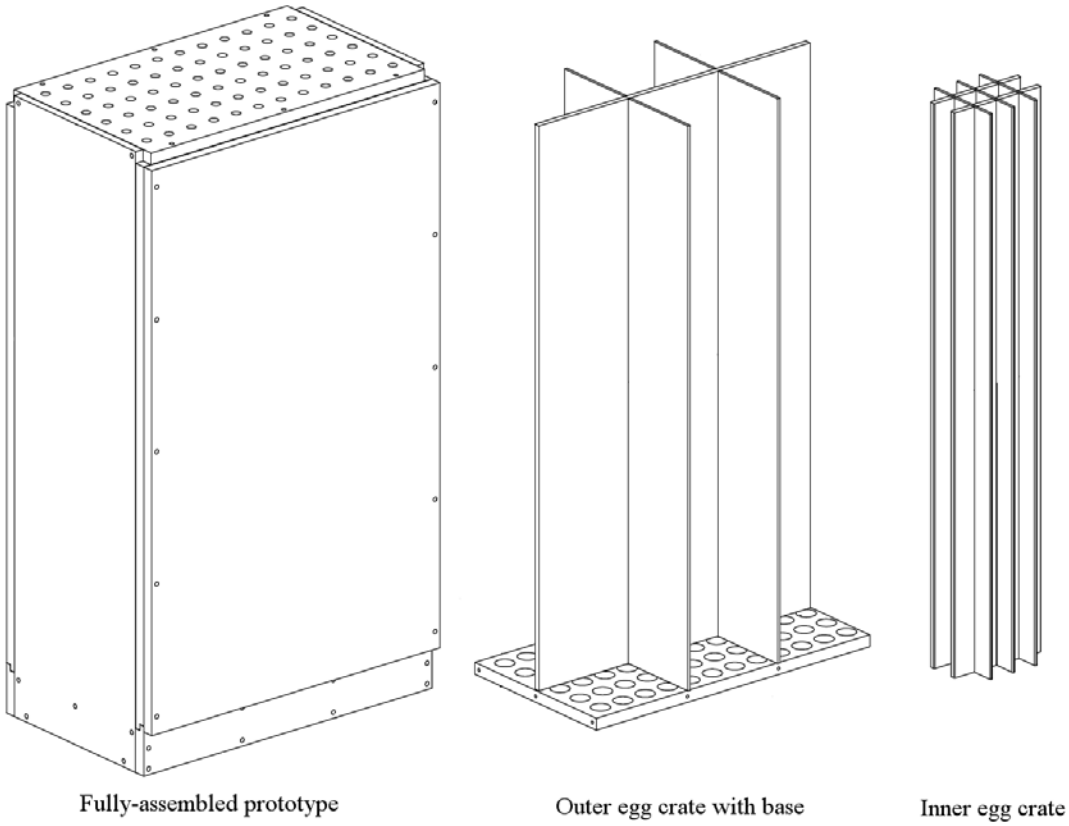

Figure 47: ANDY Prototype assembly

The lattice is comprised of nested structures of HDPE sheets that interlock in a similar fashion to old-style egg crates. Each sheet is cut through to its midpoint lengthwise to allow the sheets to slide together and form a structure without gaps. There are six inner "egg crates" that hold 12 tubes each, made from 0.635-cm and 1.27-cm thick sheets arranged in a 3x2 pattern, respectively. The larger outer egg crate is made from 1.27-cm thick sheets[30] arranged in a 2x1 pattern to hold the six inner lattices. This design greatly speeds assembly of the detector; each egg crate can be assembled by a single person and stands upright by itself. This allows them to be

[30] The design specification actually called for the two sheets aligned front-back to be 0.635-cm thick, so that all the sidewalls were the same thickness. A mistake made by the third-party fabricator led to this result.

assembled independently while the outer box is being bolted together. The large egg crate is placed inside the detector before the four outer walls are closed. The small inner egg crates, on the other hand, are light enough to be lifted above the outer walls and gently dropped inside by a single person. A team of three workers can assemble the entire HDPE lattice structure in a matter of minutes. The fully-assembled weight of the detector, including helium-3 tubes, is about 650 pounds.

5.3 Electronics and readout

Data collection for the ANDY prototype is greatly simplified by combining groups of tubes in parallel. This is done by simply daisy-chaining the high-voltage and ground connections. The number of tubes that are combined and their positions in the array depend on the data that is desired. Typically, all 72 tubes are connected into one signal to facilitate gross count rate monitoring with a single data acquisition (DAQ) channel. Other experiments dictate different detector combinations; for example, 12 tubes comprising one entire row were connected to obtain the row-by-row benchmarking data of sections 6.1 and 6.2.

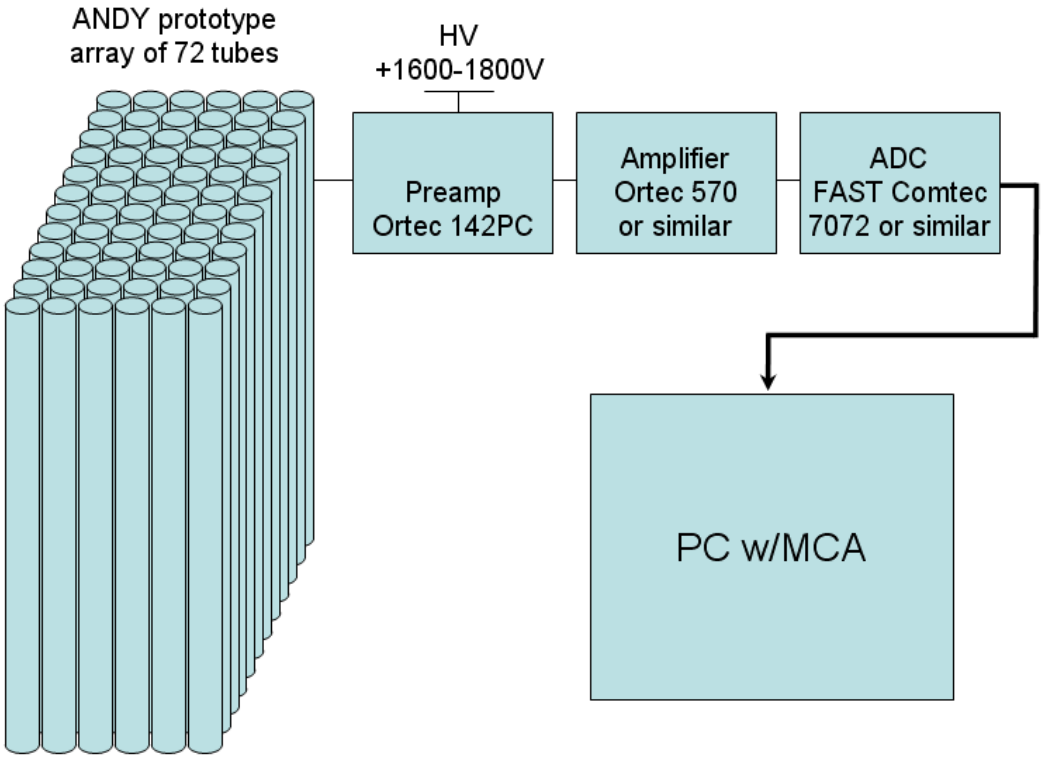

Figure 48: Electronics used in recording neutron counts from ANDY prototype detector. Groups of He-3 tubes are connected in parallel and recorded as a single channel using standard NIM electronics.

The benefits to this technique are clear: standard NIM instrumentation can be used; only one set of electronics needs to be set up; and standard histogramming software can be used to record the data, which results in simple and straightforward output files. There is no need to set up and calibrate complicated multichannel instruments or program elaborate data acquisition routines. There are drawbacks to this method, however:

- The proportional counters must be gain-matched, as there is no independent gain control for individual tubes. Each tube is independently calibrated prior to installation in the array and any outliers are discarded. After a matched set of tubes has been selected and installed, the neutron counts form a single, slightly rounded peak in the energy spectrum (see Figure 49). This peak plays the same important role as with a single tube; it allows the experimenter to identify neutron events and discriminate them with a lower-level threshold. The system is insensitive to small gain drifts because of the roundness in the peak. A gain drift is considered problematic when an additional peak appears in the spectrum. At this point, a single lower-level threshold may not be sufficient to discriminate neutron events. In the event of such a failure, each tube would have to be re-tested on an individual basis. This is a quick process that does not require removable of the tubes; any anomalous tube(s) can be replaced without disturbing the other tubes in the array.
- A more robust DAQ system would count each detector individually. The system is currently used is count rate limited compared to such a system, in that pileup occurs if multiple tubes detect neutrons simultaneously. Many of these pileup events could be recovered by implementing additional lower-level threshold(s) above

the primary neutron peak and multiplying counts in this region by the appropriate factor (2, 3, etc). However, this correction becomes increasingly inaccurate as the pileup increases and it is preferable to limit the count rate so only single-count events occur.

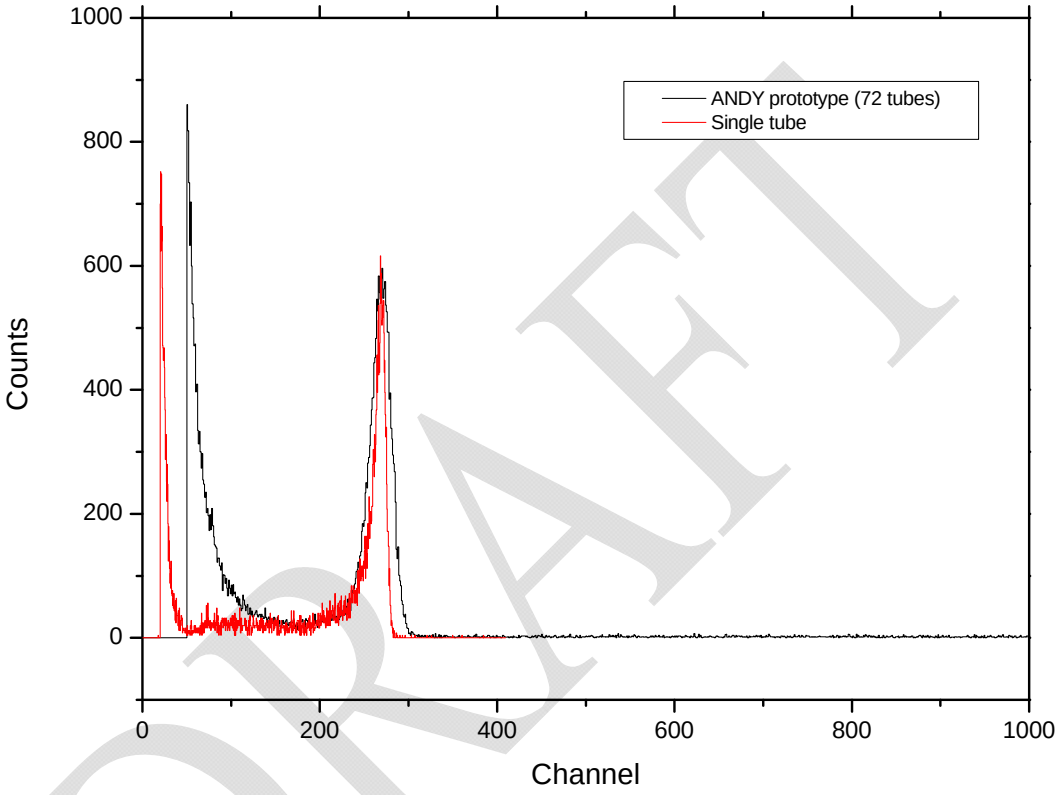

Figure 49: The pulse-height spectrum from the ANDY prototype with all 72 tubes in parallel. The spectrum is considerably noisier than the single-tube spectrum but the neutron peak is still clearly resolved.

- Another count rate limitation occurs in the form of increased saturation recovery time. When a proportional detector receives an overwhelmingly large burst of radiation, the voltage in the tube is depleted and the tube is said to be in saturation. The bias voltage is typically quickly replenished in a matter of microseconds to milliseconds by capacitive storage. During the initial recovery phase the detector is

operating proportionally, but at reduced gain. Recovery time is exacerbated in this system because of the large number of detectors that need to be "recharged" and the varying degree of depletion. The tubes at the front of the detector experience greater depletion and longer recovery time than the tubes at the rear because the rear tubes are partially shielded by the additional HDPE layers in front of them. The causes the neutron peak to appear "smeared out" because the tubes are not all operating at the same gain. The data cannot be considered valid until all tubes have recovered and a single, cohesive neutron peak appears. During recent proton interrogation experiments conducted at LANL the recovery time for the ANDY prototype was several seconds at a 30-m distance, while that for a single 2"x12" He-3 detector at a distance of 1m recovered in a few milliseconds.

- Experiments involving multiple groups of detectors (such as sections 6.1 and 6.2) require repeated measurements. Repeatedly switching detector connections to perform multi-group measurements takes time and is potentially hazardous to the experimenter and the detectors themselves. The anode connections on the detectors are somewhat fragile and due to the finite capacitance of the tubes the experimenter must take care that they are completely drained of charge or (s)he may receive a small but unpleasant shock. The anode connections are also fairly sharp and superficial scratches can occur if they are carelessly brushed up against. While the potential for accident is low when proper precautions are taken, it would still be preferable to eliminate the risk altogether by implementing a multichannel counting system that does not require the detector lid to be removed.

The drawbacks discussed above make it desirable to develop the capability to record each detector individually for long-term use of the detector. However, the daisy-chain method is perfectly satisfactory for occasional use around the laboratory, particularly when the count rates are modest. It is much more convenient for the experimenter to quickly set up a simple single-channel acquisition system than to deal with a complex 72-channel data acquisition system and struggle to re-learn the nuances that are always present in such systems. Therefore, despite the limitations of the existing method, development of such a system has been given a low priority up to this point[31].

[31] See footnote 29 on page 77.

Chapter 6 : Experimental results

Two benchmarking experiments were conducted to verify the ability of the MCNPX code to predict the performance of the ANDY prototype detector at LANL.

6.1 Individual tube efficiency measurement

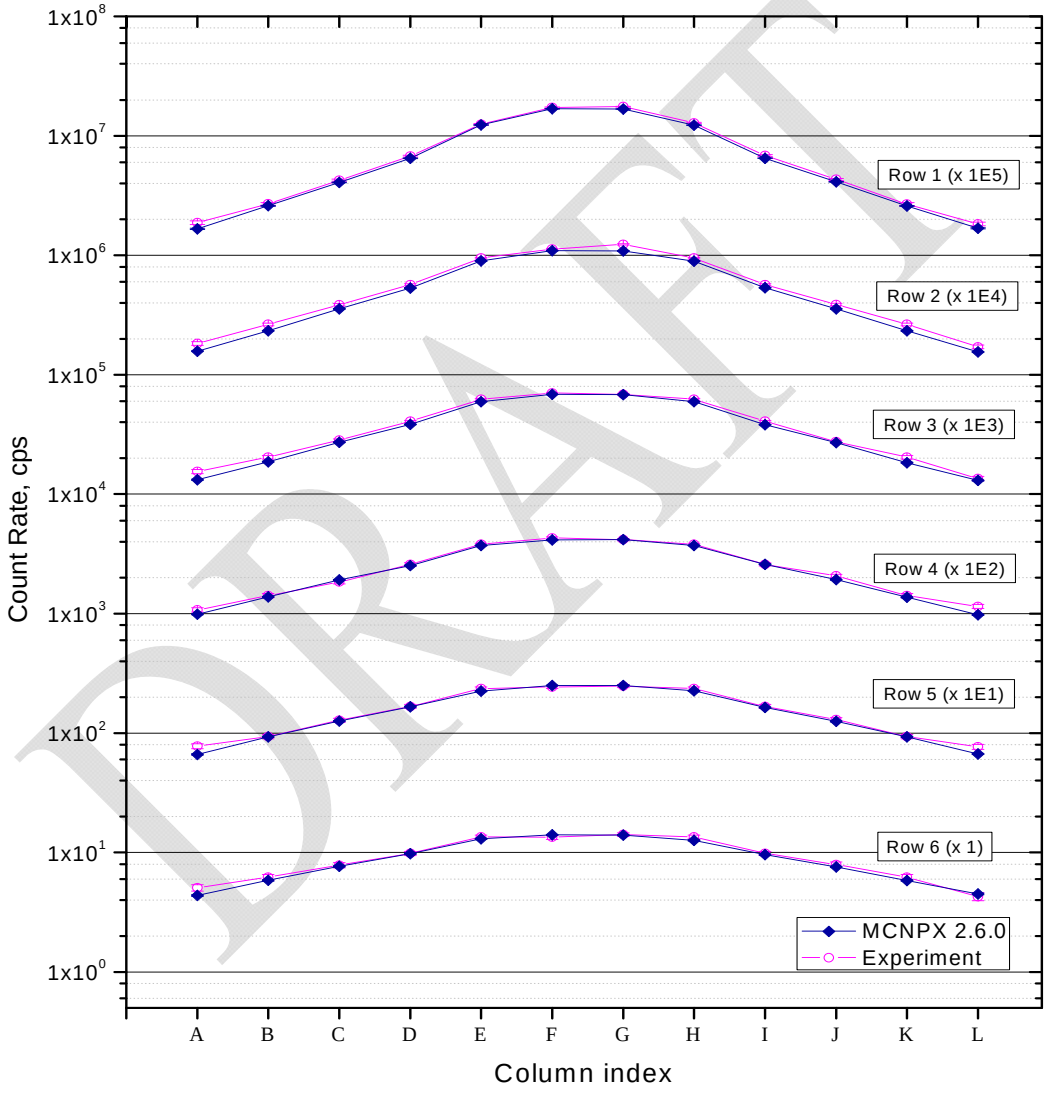

Figure 50: Results of individual-tube efficiency measurement. The results are presented in rows, with each successive row separated by a decade for clarity.

In the first experiment, the efficiency was measured at each of the 72 detector positions using a Cf-252 neutron source inside an HDPE source holder attached to the front of the detector. Several precautions were taken in order to maximize the consistency throughout the experiment: First, the source holder was keyed so it could only be attached in one position, insuring precise repeatability in the source position between background and foreground measurements. Second, all of the available He-3 tubes were counted individually and twelve were selected that had the closest-matching efficiency. These twelve tubes were then inserted into row six—the back row of the lattice. The tube in column A was counted both with and without the source. Then the tubes in columns A and B were switched and column B was counted. Then B and C were switched, and so on. Hence, the same helium-3 tube was counted in every position. The twelve tubes were then moved into row five and the process was repeated. This procedure was repeated for the remaining four rows, again continuing to use the same tube for each measurement. As a final precaution, another helium-3 tube was placed 10m from the apparatus to provide an independent measurement of the background rate. This was important because the signal-to-noise ratio for the tubes having the lowest count rates was less than 2:1. The background rate did not vary significantly throughout the experiment.

Figure 50 shows the excellent agreement between the experimental data and the MCNPX model. Overall, the experimental values are higher than the MCNPX predictions by 6.1%. This result is consistent with section 3.3.2, where the empirical data was 9.0% greater than the code. Furthermore, the experimental curves also appear to be slightly flatter across each row, which is consistent with the results of

section 3.3.3. While these results are once again not statistically significant, such consistency suggests that something is not entirely correct in the model. Several factors could create a minor effect such as this. Possibilities include incorrect HDPE density; incorrect treatment of thermal neutrons; air temperature, density, and/or humidity; or approximations in the geometry, to name just a few. The important thing, however, is that these results prove that the code is able to predict efficiencies of helium-3 detectors within a few percent. This level of precision is certainly suitable to facilitate high-fidelity planning of very sensitive experiments.

6.2 Single-row efficiency measurement with full array

The purpose of the second experiment was twofold: (1) verify the MCNPX-predicted efficiency of the ANDY prototype, and (2) benchmark the code in a more difficult experimental environment. To achieve the latter, the prototype was placed in the high-resolution-spectrometer (HRS) dome at LANSCE Area C at LANL. The HRS dome is a 14-m radius circular concrete room capped with a 0.46-m thick hemispherical concrete dome[32]. The dome is covered by a compacted-earth berm that is 3-m thick at its thinnest point. This construction provides an ideal neutron scattering trap. The detector was placed on a wooden cart 13.3 cm high and located about 5 meters from the nearest concrete wall.

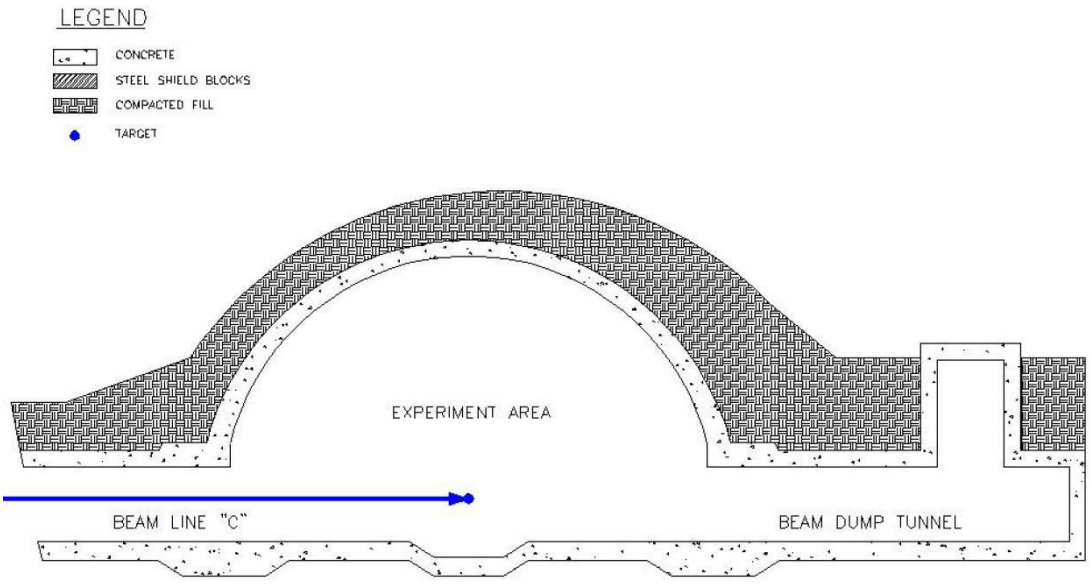

Figure 51: Cross-sectional view of the HRS Dome at LANSCE Area C.

[32] Given dimensions for the HRS dome are approximate.

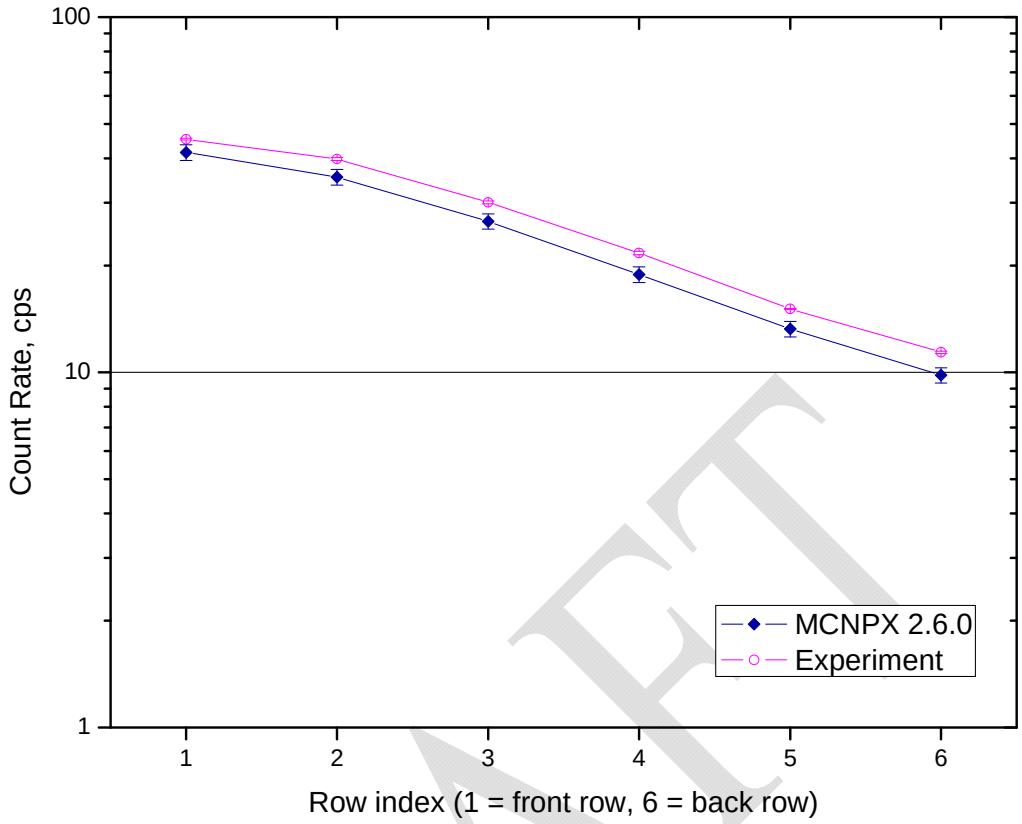

Figure 52: Results of row-sum efficiency measurement with full ANDY array including only the concrete floor in the MCNPX model. The MCNPX data was given 5% error bars to account for approximations in the detector and source models.

Figure 52 was created by summing each row of tubes individually. Only the source, detector, and concrete floor were included in the MCNPX model. Overall, the MCNPX results are 11.6% less than the experimental data. The intrinsic efficiency calculated by MCNPX was 20.2%, 13.0% less than the measured value of 23.2%. These deficiencies are comparable to but slightly greater than those from the results presented earlier. Conversely, the differences are also within the expected range of the efficacy from Chapter 2. Consequently, an improved model is needed to determine if these results are consistent with the other experiments. The question,

then, is what details need to be added to the model to obtain a sufficiently precise result? In this case the choice was fairly straightforward; the experiment and code are already very close to agreement, so the simulation was repeated, this time including the circular walls and dome in the model.

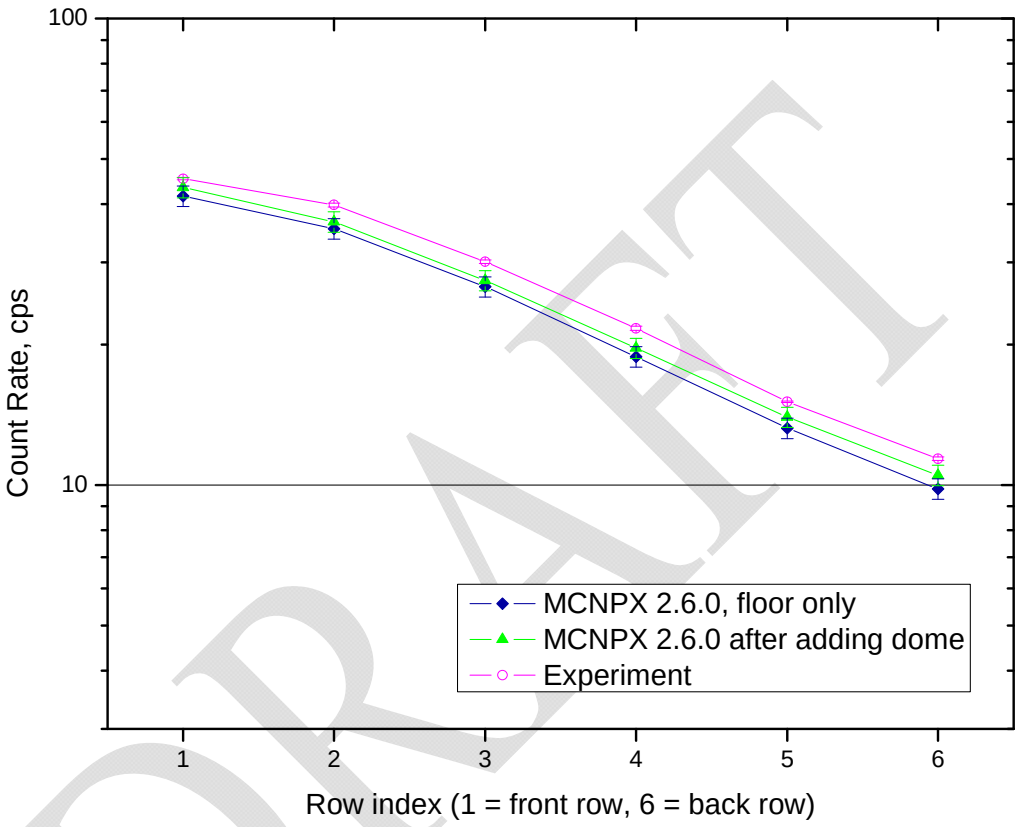

Figure 53: Results of row-sum efficiency measurement with improved MCNPX model.

Adding the concrete dome to the model made a small but profound difference in the results. The average deficiency in the row sums decreased to 7.6% and the difference in efficiency is only 7.2%. Both figures are now in excellent agreement with the earlier results. Now it can certainly be said with confidence that the calibrated source activity is too low by 6-9%.

Chapter 7 : Conclusion

Computer simulations with the MCNPX code predict an increase in cost efficiency of 2.5-3.5 for neutron detectors based on an array of low-pressure helium-3 drift tubes (ANDY-type detector) over conventional high-pressure tubes. A prototype ANDY detector was designed and constructed at LANL. The results were validated by conducting several benchmarking experiments. All of the experiments showed excellent agreement between the computer model and measured data. The results were consistent enough to suggest a correction factor of 6-9% for the activity of several Cf-252 sources that are frequently used at LANL. The concept of efficacy was introduced as a deterministic method of calculating changes in detector count rate that arise from neutrons scattering from objects in the environment. A successful series of neutronics benchmarking experiments reinforces this concept. The results presented herein provide solid groundwork for the design of large-area neutron detectors that will be used in Homeland Security applications. More importantly, this work paves the road toward successful management of limited worldwide helium-3 resources for many years to come.

7.1 Additional Work

Several additional studies are underway to extend this work. A few of these are presented in brief:

7.1.1 Addition of boron lining for further increase in efficiency

The efficiency of low-pressure gaseous neutron detectors can be increased by adding a boron lining. Work is currently underway at LANL to develop this

technology in a robust and cost-effective manner. Figure 54 shows an early initial result. The efficiency of this particular helium-3 detector was increased by nearly 20%. Details of the methods being investigated are proprietary.

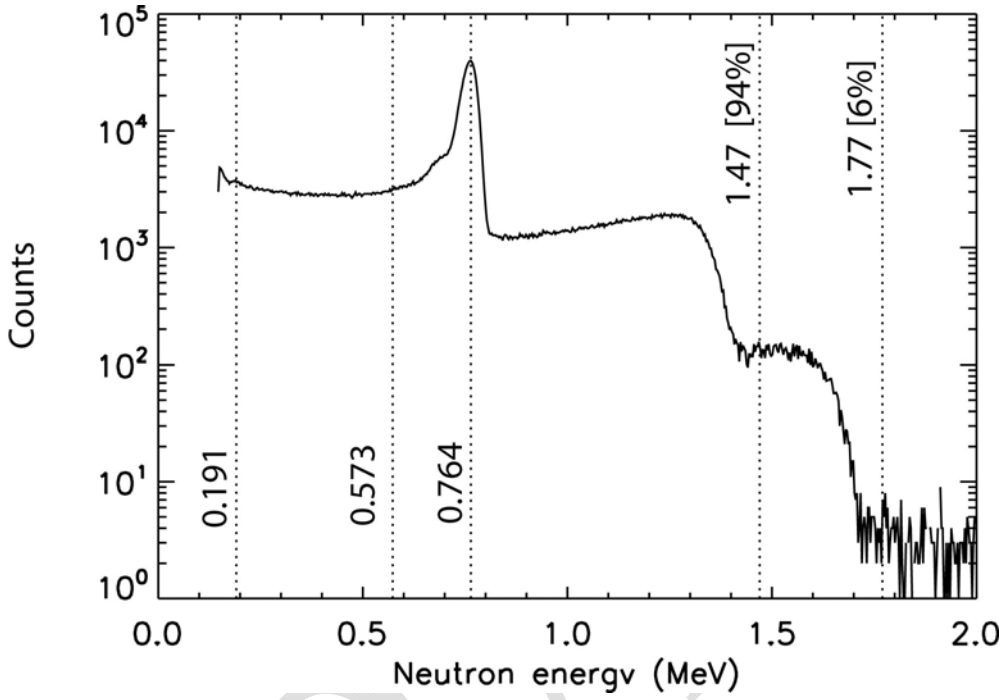

Figure 54: Pulse-height spectrum of a ^{3}He-^{10}B hybrid detector. Key features identifying the daughter particles from both isotopes are clearly distinguishable.

7.1.2 Energy selection via external shielding

The response curve of ANDY-type detectors as a function of neutron energy can be tailored to a desired neutron flux spectrum by adding external neutron moderators and/or absorbers. Figure 55 shows a few examples:

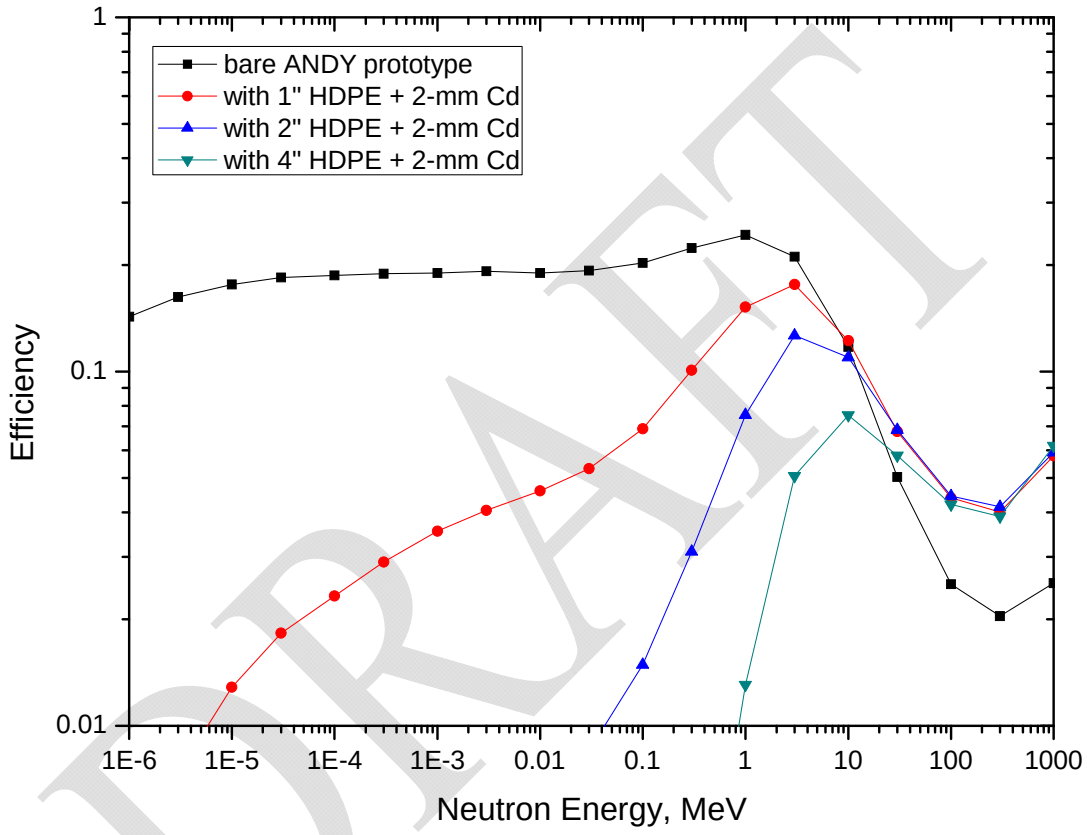

Figure 55: Efficiency curves for the ANDY prototype with several external shielding scenarios.

7.1.3 External Monitoring for Dosimetry and Experimental Support

The high sensitivity of the ANDY prototype detector also makes it very useful for external monitoring applications. These can include dose measurements taken *outside* primary shielding walls as demonstrated in Figures 56-58 or as a sanity check to verify that beam was delivered, to name just a few.

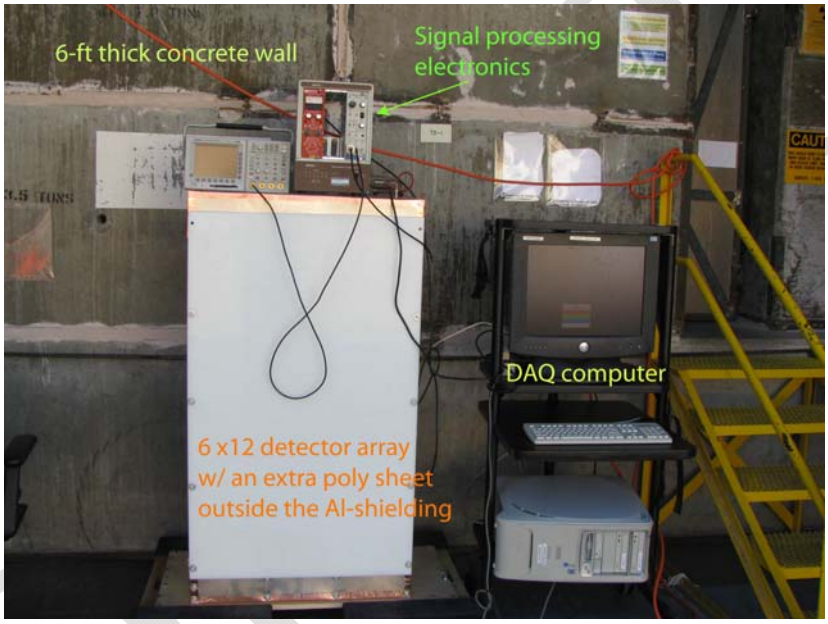

Figure 56: The ANDY Prototype in operation outside the primary shielding door at Area C at LANSCE (HRS dome).

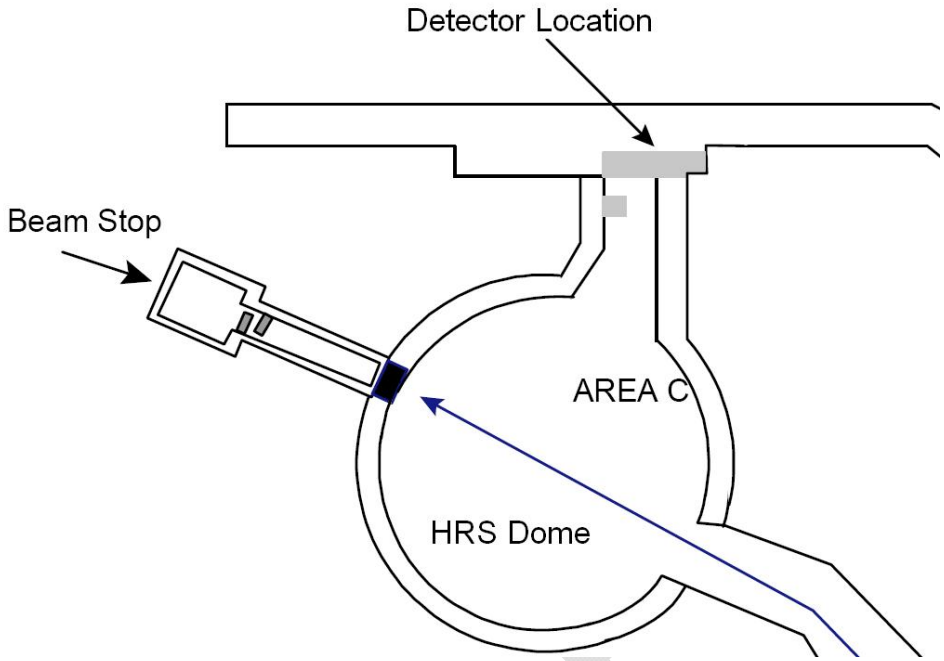

Figure 57: Overhead view of the HRS dome. The blue line is the path of the proton beam.

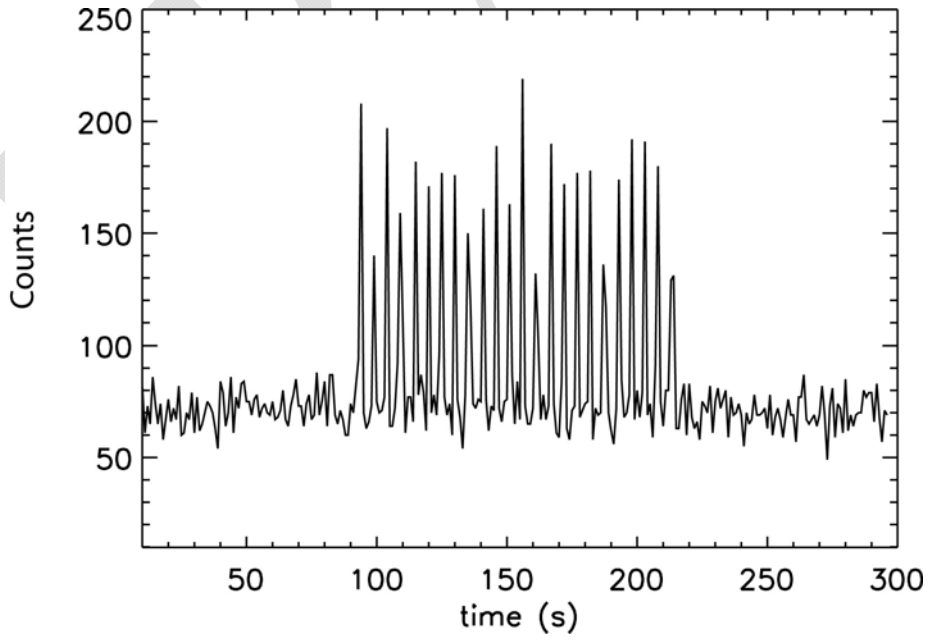

Figure 58: Time response of ANDY prototype during proton beam tuning.

References

1. J.M. Cork, Radioactivity and Nuclear Physics, D. Van Nostrand Co. Inc, New York, 1947.

2. J. Chadwick and M. Goldhaber, "A 'Nuclear Photo-effect': Disintegration of the Diplon by g-Rays", Nature **134**, pg 237, 1934.

3. D. B. Pelowitz, editor, MCNPX User's Manual, Version 2.6.0, Los Alamos National Laboratory, LA-CP-07-1473, 2008.

4. W.J. Price, Nuclear Radiation Detection, 2nd Ed., McGraw-Hill Book Company, New York, 1964.

5. ASTM E 721-94, 1998. "Standard guide for determining neutron energy spectra . . .", 1998 Annual Book of ASTM Standards, Vol. 12.02, ASTM, West Conshohocken, PA, pp. 280-290.

6. Wheeler FJ, Nigg DW, Capala J, Watkins PR, Vroegindeweij C, Auterinen I, Seppälä T, Bleuel D, "Boron neutron capture therapy (BNCT): implications of neutron beam and boron compound characteristics", Medical Physics, Vol. 26 No. 7, pp 1237-44 (1999).

7. J. F. Briesmeister, Editor, X-5 Division, LANL, MCNP-A General Monte Carlo N-Particle Transport Code, Version 4C, RSICC, Oak Ridge National Laboratory, 2000.

8. A. Foderaro, The Elements of Neutron Interaction Theory, The MIT Press, Cambridge, Massachusetts and London, England, 1971.

9. C.E. Wiegand, et al, "Detection Efficiency of Plastic Scintillator for Neutron Energies 4 to 76 MeV", Rev. Sci. Instr., **33** No. 5, pg 526, 1962.

10. P.L. Reeder, "Detection of fast neutrons in a plastic scintillator using digital pulse processing to reject gammas", Nuclear Instruments and Methods-A 422 No 1-3, pp 84-88, 1999.

11. L.M. Bollinger and G.E. Thomas, "Neutron Detection with Glass Scintillators", Nucl. Instr. and Methods 17, pp 97-116, 1962.

12. G.E. Thomas, "A boron-loaded liquid scintillation neutron detector using a single photomultiplier", Nucl. Instr. and Methods 17, pp 137-139, 1962.

13. http://www.nndc.bnl.gov/exfor/endf00.htm; "Evaluated Nuclear Data File", National Nuclear Data Center, Brookhaven National Laboratory, New York.

14. See http://ie.lbl.gov/ngdata/sig.txt for a convenient list; "Neutron Cross Sections . . .", S.F Mughabghab, M. Divadeenam and N.E. Holden, Academic Press, 1981.

15. Z. Wang, et al, "Inexpensive and practical sealed drift-tube neutron detector", submitted to Nuclear Instruments and Methods-A, Feb 2009.

16. R.B Firestone, Coral M. Baglin, and S.Y Frank Chu, Table of Isotopes, 8th Ed., John Wiley & Sons, New York, NY, 1999.

17. A.J Stokes, T.J. Meal, J.E. Myers, Jr, "Improved performance of BF3 neutron counters in high gamma fluxes", IEEE Transactions on Nuclear Science, **13**, pp 630-635, 1966.

18. MCNPX simulation of proton interrogation experiments conducted at LANSCE. Calculations performed by Randy Spaulding, LANL MCNPX applications team, D-5 group, 2008 (unpublished).

19. S.Y.F. Chu, L.P. Ekstrom, R.B. Firestone, The Lund/LBNL WWW Table of Radioactive Isotopes, http://nucleardata.nuclear.lu.se/NuclearData/toi/

20. F.-J. Hambsch, A. Tudora, G. Vladuca, S. Oberstedt, "Calculation of Prompt Neutron Multiplicities and Spectra for Several Nuclides", International Conference on Nuclear Data for Science and Technology, AIP CP 769, pp 362-365, May 24 2005.

21. A.S. Vorobyev, V.N. Dushin, F.-J. Hambsch, V.A. Jakovlev, V.A. Kalinin, A.B. Laptev, B.F. Petrov, and O.A. Shcherbakov, "Distribution of Prompt Neutron Emission Probability for Fission Fragments in Spontaneous Fission of 252Cf and 244, 248Cm", International Conference on Nuclear Data for Science and Technology, AIP CP 769, pp 613-616, May 24 2005.

22. R. C. Martin, J. B. Knauer, and P. A. Balo, "Production, Distribution, and Applications of Californium-252 Neutron Sources", presented at 4th Topical Meeting on Industrial Radiation and Radioisotope Measurement Applications (IRRMA '99), Raleigh, North Carolina, Oct. 3-7, 1999.

23. "Properties of Neutron Sources", Proceedings of an Advisory Group Meeting on Properties of Neutron Sources Organized by the International Atomic Energy Agency, June 9-13 1986, Leningrad, USSR, p.10, International Atomic Energy Agency, Vienna, 1986.

24. Proceedings of IAEA Panel Neutron Standard Reference Data, Vienna, Austria, Nov. 20-24 1972, CONF-721127, p. 362, International Atomic

Energy Agency, Vienna, 1973.

25. Proceedings of IAEA Consultants' Meeting on Prompt Fission Neutron Spectra, Vienna, Austria, Aug. 25-27 1971, p. 169, International Atomic Energy Agency, Vienna, 1979.

26. Definition and discussion at http://en.wikipedia.org/wiki/Efficacy

27. MCNPX calculations performed by Randy Spaulding, 2000-2009.

28. Anatoly V. Zrodnikov, Victor Ya. Poupko, and George M. Gryaznov, "Experimental Detection of Neutron Gas Pressure on the Control Rods of a Nuclear Reactor under the Microgravity Conditions", AIP Conf. Proc. 301, 625, 1994.

29. J. Kammeraad et al., "Radiological and Nuclear Countermeasures", Department of Homeland Security, Briefing, 9 March 2004

30. D. Srikrishna, A. N. Chari and T. Tisch, "Deterrence of Nuclear Terrorism with Mobile Radiation Detectors", *Nonproliferation Review*, 12.3, pp. 573-614, 2005.

31. J. Medalia, "Nuclear Terrorism: A Brief Review of Threats and Responses", CRS Report for Congress RL32595, The Library of Congress, 2004.

32. A. Glaser, "Detection of Special Nuclear Materials", http://www.princeton.edu/~aglaser/lecture2007_detection.pdf

33. S.J. Greene, "Delayed Neutron Emission Induced by 800 MeV Protons", http://p25ext.lanl.gov/~hubert/activei/files/AIWorkshop07.ppt, 2007.

34. J.L Jones, et al, "Proof-of-Concept Assessment of a Photofission-Based Interrogation System for the Detection of Shielded Nuclear Material", INEEL Report INEEL/EXT-2000-01523, 2000.

35. M.T. Kinlaw, A.W. Hunt, "Fissionable isotope identification using the time dependence of delayed neutron emission", Nuclear Instruments and Methods in Physics Research-A 562, pp1081-1084, 2006.

36. J. Medalia, "Terrorist Nuclear Attacks on Seaports: Threat and Response", CRS Report for Congress RS21293, The Library of Congress, 2005.

37. U.S. Department of Homeland Security, Bureau of Customs and Border Protection, "Remarks by Commissioner Robert C. Bonner, Council on Foreign Relations, New York, New York,", January 11, 2005.

38. http://en.wikipedia.org/wiki/Container_Ship

39. G. Peter Nanos, Jr., “CWMD Research & Development Overview”, briefing delivered at 2008 Unrestricted Warfare Conference, March 10, 2008.

40. H. Daniel, “Application of muonic X-rays for elemental analysis”, Biological trace Element Research, Vol. 13 No. 1 pp 301-318, 2007.

41. L.J. Wittenberg, “Non-Lunar He-3 Resources”, presented at the second Wisconsin Symposium on helium-3 and Fusion Power, Madison Wi, July 1993.

42. L.J. Wittenberg, et al, “A Review of helium-3 resources and acquisition for use as a fusion fuel”, Fusion Technology, Special Issue on D-He3 Fusion, Vol. 21 No. 4, pp 2230-2253, 1991.

43. J. Bonde & A. Tortorello, “Helium-3: The energy source of tomorrow?”, http://web.mit.edu/22.012/www/presentations/Helium-3%20version%202.ppt

44. LND Inc. product listing, http://www.lndinc.com/products/category/22/

45. K. Borozdin et al., "Radiographic Imaging with Cosmic Ray Muons", Nature, 422, p.277, 2003.

46. J. A. Green, C. Alexander, T. Asaki, J. Bacon, G. Blanpied, K. Borozdin, et al., "Optimizing the Tracking Efficiency for Cosmic Ray Muon Tomography", 2006 IEEE Nuclear Science Symposium Conference Record, San Diego, CA 286-288, 2006.

47. C. L. Morris, C. C. Alexander, J. D. Bacon, K. N. Borozdin, et al., "Tomographic Imaging with Cosmic Ray Muons", Science & Global Security, Vol. 16 No. 1&2, pp 37-53, 2008.

Appendix A: Sample MCNPX input file

The following input deck represents a model of the ANDY prototype detector located inside the HRS dome.

A.1: Listing of MCNPX input file rbr01.i

```
rbr01.i: Measuring row-by-row neutron efficiency
C
C ******************************** Comments *********************************
C
C Modeling 10/17/2008 experiment
C ANDY prototype in dome on wooden rolling carts
C
C
C ******************************** Cell Cards *******************************
C
C ................................................ Primary Detector Structures
601    13  -2.7         -601 602 604                          $    Al Faraday Cage
603  2201  -9.264E-04   -603 611 612 613 614 615 616 750      $       Interior Air
604  2201  -9.264E-04   -604 741 721 731                      $            Top Air
605  2201  -9.264E-04   -605                                  $          Lower Air
C
611  2201  -9.264E-04   -611 751                              $    Big EC Cell 000
612  2201  -9.264E-04   -612 #752                            $    Big EC Cell 100
613  2201  -9.264E-04   -613 #753                            $    Big EC Cell 200
614  2201  -9.264E-04   -614 #754                            $    Big EC Cell 001
615  2201  -9.264E-04   -615 #755                            $    Big EC Cell 101
616  2201  -9.264E-04   -616 #756                            $    Big EC Cell 201
C
C ................................................ Outer Box Front Polyethylene
701  3221  -0.95        -701 702 703                          $ Front poly modratr
702  2201  -9.264E-04   -702 750                              $             Groove
703  2201  -9.264E-04   -703 750                              $             Groove
C
C ................................................ Outer Box Back Polyethylene
711  3221  -0.95        -711 712 713 714                      $  Back poly modratr
712  2201  -9.264E-04   -712 750                              $             Groove
713  2201  -9.264E-04   -713 750                              $             Groove
714  2201  -9.264E-04   -714                                  $               Step
C
C ................................................ Outer Box Side Polyethylene
721  3221  -0.95        -721 722 741 742                      $ RSide poly modratr
722  2201  -9.264E-04   -722                                  $             Groove
731  3221  -0.95        -731 732 741 742                      $ LSide poly modratr
732  2201  -9.264E-04   -732                                  $             Groove
C
C ........................................ Outer Box Top, Base, and Lower Base
741  3221  -0.95        -741 831 832 833 834 835 836          $               Top
742  3221  -0.95        -742 781 782 783 784 785 786          $              Base
743  3221  -0.95        -743                                  $         Lower Base
C
C ................................................................ Large Egg Crate
C This definition has a glitch where the crate slides into the slots
C in the front and rear panels.  Its negligible.
750  3221  -0.95        -750 611 612 613 614 615 616
                        (701:-702:-703) (711:-712:-713)
751  2201  -9.264E-04   -751             fill=761
752  2201  -9.264E-04   -752             fill=762
753  2201  -9.264E-04   -753             fill=763
754  2201  -9.264E-04   -754             fill=764
755  2201  -9.264E-04   -755             fill=765
756  2201  -9.264E-04   -756             fill=766
C
```

```
761  2201  -9.264E-04   -761    trcl=761 lat=1 u=761
           fill=0:3 0:0 0:2    1  3r         1  3r         1  3r
C
762  like 761 but               trcl=762 lat=1 u=762
           fill=0:3 0:0 0:2    1  3r         1  3r         1  3r
C
763  like 761 but               trcl=763 lat=1 u=763
           fill=0:3 0:0 0:2    1  3r         1  3r         1  3r
C
764  like 761 but               trcl=764 lat=1 u=764
           fill=0:3 0:0 0:2    1  3r         1  3r         1  3r
C
765  like 761 but               trcl=765 lat=1 u=765
           fill=0:3 0:0 0:2    1  3r         1  3r         1  3r
C
766  like 761 but               trcl=766 lat=1 u=766
           fill=0:3 0:0 0:2    1  3r         1  3r         1  3r
C
C ..................................................................... Source
C
772    13  -2.7         -772
C ..................................................... Holes in base
779  3221  -0.95         780                              u=3 $             HDPE
780  2201  -9.264E-04   -780                              u=3 $             Hole
781  3221  -0.95        -781             fill=781
782  3221  -0.95        -782             fill=782
783  3221  -0.95        -783             fill=783
784  3221  -0.95        -784             fill=784
785  3221  -0.95        -785             fill=785
786  3221  -0.95        -786             fill=786
C
791  3221  -0.95        -791    trcl=791 lat=1 u=781 fill=3
792  like 791 but               trcl=792 lat=1 u=782
793  like 791 but               trcl=793 lat=1 u=783
794  like 791 but               trcl=794 lat=1 u=784
795  like 791 but               trcl=795 lat=1 u=785
796  like 791 but               trcl=796 lat=1 u=786
C
C ..................................................... Neutron Detectors
C
800  2201  -9.264E-04    801 805 806                     u=1 $        Outside Air
801    13  -2.7         -801 802                         u=1 $     Detector Outer
802  2344  -1.974E-03   -802 803                         u=1 $       Detector Gas
803  2344  -1.974E-03   -803 804                         u=1 $       Detector Gas
804  2201  -9.264E-04   -804                             u=1 $         Anode Wire
805  3221  -0.95        -805                             u=1 $          Side wall
806  3221  -0.95        -806                             u=1 $          Back wall
C
810  2201  -9.264E-04        805 806                     u=2 $     Empty Cell Air
815  3221  -0.95        -805                             u=2 $ EmptyCel Side wall
816  3221  -0.95        -806                             u=2 $ EmptyCel Back wall
C
C ..................................................................... Top holes
C
827  3221  -0.95         828 829                         u=4 $           Top HDPE
828  2201  -9.264E-04   -828 829                         u=4 $           Top hole
829  2201  -9.264E-04   -829                             u=4 $           Top cone
831  3221  -0.95        -831             fill=841
832  3221  -0.95        -832             fill=842
833  3221  -0.95        -833             fill=843
834  3221  -0.95        -834             fill=844
835  3221  -0.95        -835             fill=845
836  3221  -0.95        -836             fill=846
841  3221  -0.95        -841    trcl=841 lat=1 u=841 fill=4 $     Top Hole univ
842  like 841 but               trcl=842 lat=1 u=842        $     Top Hole univ
843  like 841 but               trcl=843 lat=1 u=843        $     Top Hole univ
844  like 841 but               trcl=844 lat=1 u=844        $     Top Hole univ
845  like 841 but               trcl=845 lat=1 u=845        $     Top Hole univ
846  like 841 but               trcl=846 lat=1 u=846        $     Top Hole univ
C
C ..................................................... Air & Universe
```

```
C
990  2201  -9.264E-04 -990                                  $     Concrete floor
998  2201  -9.264E-04 -999 601 990 772
999     0              999

C ****************************** Surface Cards ******************************
C
C ......................................................................
C Primary Detector Structures
C                                                          $   Faraday Outer
0601  01  rpp  -0.079375  75.618975  -0.079375  138.179175  -0.079375
       46.104175
0602  01  rpp  0  75.5396  0  133.985  0  46.0248            $       Outer Box
0603  01  rpp  2.54  72.9996  9.525  131.445  2.54  40.9448  $        Interior
0604  01  rpp  0  75.5396  131.445  138.0998  0  46.0248     $       Upper Air
0605  01  rpp  2.54  72.9996  2.54  6.985  2.54  40.9448     $       Lower Air
0611  01  rpp  2.54  25.2857  9.525  131.445  2.54  21.1074  $    EC1 Cell 000
0612  01  rpp  26.5557  48.9839  9.525  131.445  2.54  21.1074$    EC1 Cell 100
0613  01  rpp  50.2539  72.9996  9.525  131.445  2.54  21.1074$    EC1 Cell 200
0614  01  rpp  2.54  25.2857  9.525  131.445  22.3774  40.9448$    EC1 Cell 001
C                                                          $    EC1 Cell 101
0615  01  rpp  26.5557  48.9839  9.525  131.445  22.3774  40.9448
C                                                          $    EC1 Cell 201
0616  01  rpp  50.2539  72.9996  9.525  131.445  22.3774  40.9448
C
C ......................................................................
C Outer Box Front Polyethylene
0701  01  rpp  0  75.5396  0  131.445  0  2.54             $        OB Front
0702  01  rpp  25.273  26.5684  9.525  131.445  2.1336  2.54  $       OBF Grv 1
0703  01  rpp  48.9712  50.2666  9.525  131.445  2.1336  2.54 $       OBF Grv 2
C
C ......................................................................
C Outer Box Back Polyethylene
0711  01  rpp  0  75.5396  0  131.445  40.9448  46.0248      $         OB Back
C                                                          $      OBBk Grv 1
0712  01  rpp  25.273  26.5684  9.525  131.445  40.9448  41.3512
C                                                          $      OBBk Grv 2
0713  01  rpp  48.9712  50.2666  9.525  131.445  40.9448  41.3512
0714  01  rpp  0  75.5396  0  9.525  43.4848  46.0248        $       OBBk Step
C
C ......................................................................
C Outer Box Side Polyethylene
0721  01  rpp  0  2.54  0  133.985  2.54  40.9448           $       OB R Side
0722  01  rpp  2.2098  2.54  9.525  131.445  21.082  22.4028  $        OBRS Grv
0731  01  rpp  72.9996  75.5396  0  133.985  2.54  40.9448   $       OB L Side
C                                                          $        OBLS Grv
0732  01  rpp  72.9996  73.3298  9.525  131.445  21.082  22.4028
C
C ......................................................................
C Outer Box Top, Base, and Lower Base
0741  01  rpp  1.905  73.6346  131.445  133.985  0  43.4848   $          OB Top
0742  01  rpp  1.905  73.6346  6.985  9.525  2.54  40.9448    $         OB Base
0743  01  rpp  2.54  72.9996  0  2.54  2.54  40.9448          $    OB Lowerbase
C
C ......................................................................
C Large Egg Crate
0750  01  rpp  2.8448  72.6948  9.525  131.445  2.2098  41.275$    Lg Egg Crate
C                                                          $    EC2 Univ 000
0751  01  rpp  2.8576  25.2856  9.5251  131.4449  3.1751  21.1073
C                                                          $    EC2 Univ 100
0752  01  rpp  26.5558  48.9838  9.5251  131.4449  3.1751  21.1073
C                                                          $    EC2 Univ 200
0753  01  rpp  50.254  72.682  9.5251  131.4449  3.1751  21.1073
C                                                          $    EC2 Univ 001
0754  01  rpp  2.8576  25.2856  9.5251  131.4449  22.3775  40.3097
C                                                          $    EC2 Univ 101
0755  01  rpp  26.5558  48.9838  9.5251  131.4449  22.3775  40.3097
C                                                          $    EC2 Univ 201
0756  01  rpp  50.254  72.682  9.5251  131.4449  22.3775  40.3097
0761  01  rpp  -2.5654  3.2004  0  121.92  -2.5654  3.8354    $  EC2-000 UnitCl
C
```

```
C ....................................................................
C Source
C                                                          $       Src Block
0771      rpp  33.0073  42.5323  64.77  76.2  -2.619375  -0.079375
C                                                          $   Cf-252 source
0772      rcc  37.7698  80.645  -100       0 2.54   0  0.4
0773      rcc  37.7698  70.485  -1.079375  0  0  1  0.400000  $        Src hole
0774      rcc  36.769800  70.485  -1.079375  0  0  1  0.400000$        Src hole
0775      rcc  38.769800  70.485  -1.079375  0  0  1  0.400000$        Src hole
C
C ....................................................................
C Holes in base
0780  01  rcc  6.29412  6.985  6.61162  0  2.54  0  2.032     $        Hole 000
0781  01  rpp  2.8575  25.9207  6.985  9.525  3.175  21.717   $    HoleUniv 000
0782  01  rpp  26.5557  49.6189  6.985  9.525  3.175  21.717  $    HoleUniv 100
0783  01  rpp  50.2539  73.3171  6.985  9.525  3.175  21.717  $    HoleUniv 200
0784  01  rpp  2.8575  25.9207  6.985  9.525  21.7678  39.6748$    HoleUniv 001
C                                                          $    HoleUniv 101
0785  01  rpp  26.5557  49.6189  6.985  9.525  21.7678  39.6748
C                                                          $    HoleUniv 201
0786  01  rpp  50.2539  73.3171  6.985  9.525  21.7678  39.6748
0791  01  rpp  2.8575  8.6233  6.985  9.525  3.175  9.5758    $       Hole Univ
C
C ....................................................................
C Neutron Detectors
0801  01  rcc  0 -1  0  0  122.92  0  2.54                   $       Det outer
0802  01  rcc  0  0.0254  0      0   121.8692  0  2.5146     $       Det inner
0803  01  rcc  0  0.025654  0 0  121.868692  0 2.514346      $     Boron layer
0804  01  rcc  0  0.025654  0 0  121.868692  0  0.00635     $      Anode wire
0805  01  rpp  2.5654  4.2004  -1 122.92  -3.5654  4.8354    $       Side poly
0806  01  rpp  -3.5654  2.5654 -1  122.92  2.5654  4.8354    $       Back poly
C
C ....................................................................
C Holes in Top
0828  01  rcc  0  131.4449  0  0  2.5402  0  0.9525         $        Top hole
0829  01  k/y  0  133.35  0  1  -1                          $     Top cntrsnk
C                                                          $ Top Hole UnitCl
0841  01  rpp  -2.5654  3.2004  131.4449  133.9851  -2.5654  3.8354
C                                                          $TopHole Univ 000
0831  01  rpp  2.8576  25.2856  131.445  133.985  3.1751  21.1073
C                                                          $TopHole Univ 100
0832  01  rpp  26.5558  48.9838  131.445  133.985  3.175  21.1074
C                                                          $TopHole Univ 200
0833  01  rpp  50.254  72.682  131.445  133.985  3.1751  21.1073
C                                                          $TopHole Univ 001
0834  01  rpp  2.8576  25.2856  131.445  133.985  22.3775  40.3097
C                                                          $TopHole Univ 101
0835  01  rpp  26.5558  48.9838  131.445  133.985  22.3775  40.3097
C                                                          $TopHole Univ 201
0836  01  rpp  50.254  72.682  131.445  133.985  22.3775  40.3097
C
C ....................................................................
C Air & Universe
0990      rpp  -2999  2999  -199    0  -2999  2999            $           Floor
0999      rpp  -3000  3000  -200  800  -3000  3000            $     world bndry

C ****************************** Transformations ****************************
C
C                                                            5-1/4" above floor
tr01   0    13.335    0                                     $  Detector origin
C
tr761  5.422900000  9.5250  5.740400000                $   EC2-000 univ origin
tr762  29.12110000  9.5250  5.740400000                $   EC2-100 univ origin
tr763  52.81930000  9.5250  5.740400000                $   EC2-200 univ origin
tr764  5.422900000  9.5250  24.94280000                $   EC2-001 univ origin
tr765  29.12110000  9.5250  24.94280000                $   EC2-101 univ origin
tr766  52.81930000  9.5250  24.94280000                $   EC2-201 univ origin
C
tr791   0          0       0                          $  Base Hole-000 origin
tr792  23.6982     0       0                          $  Base Hole-100 origin
tr793  47.3964     0       0                          $  Base Hole-200 origin
```

```
tr794   0           0      17.45996                    $  Base Hole-001 origin
tr795  23.6982      0      17.45996                    $  Base Hole-101 origin
tr796  47.3964      0      17.45996                    $  Base Hole-201 origin
C
tr841  5.422900000  0       5.740400000                $   EC2-000 univ origin
tr842  29.12110000  0       5.740400000                $   EC2-100 univ origin
tr843  52.81930000  0       5.740400000                $   EC2-200 univ origin
tr844  5.422900000  0       24.94280000                $   EC2-001 univ origin
tr845  29.12110000  0       24.94280000                $   EC2-101 univ origin
tr846  52.81930000  0       24.94280000                $   EC2-201 univ origin
C
C ****************************** Material Cards ******************************
C
read file lanl_gas.trf
read file air_2201_lineC.trf
read file poly_3221.trf
read file concrete_lanl_m5.trf
read file 304.trf
C
C -=-=-=-=-=-=-=-=-=-=-=-=-=-=-=-=-=-=-=-=-=-=-=-=-=-=-=-=-=-=-=- Aluminum, p = 2.7
m13    13027 1
C                                                    Polyurethane Foam p = 0.12
m1028    6012  25      1001  42     7014   2       8016   6
C                                                   Polystyrene  p = 1.060
m3226    1001      -7.7418     6000     -92.2582
C
C
C ***************************** Variance Reduction *****************************
C
imp:n 1  78r   0
C
C ****************************** Source Cards ******************************
C
C Cf-252 area sources, 12 tube positions, vertical thirds
C
sdef   par=1
       erg=d1
       cel 772
       pos 37.7698  80.645  -100
       rad=d4
       ext=d5
       axs=0 1 0
C
si4 0 0.3
sp4 -21 1
C
si5 0.1 0.9
sp5   0   1
C
read file cf252_unbiased.trf
C
C ********************************* Tallies *********************************
C
  FC1 Current crossing the outer faces
   F1:n 602.1 602.2 602.5 602.6
   C1 0 1
   T1 0  36i  37e8
  FQ1 T F C
C
FC104    Flux-integrated He3 signal, rows and total
 F104:n
     (803<(761[0:3 0:0 0:0] 762[0:3 0:0 0:0] 763[0:3 0:0 0:0])<(751 752 753))
     (803<(761[0:3 0:0 1:1] 762[0:3 0:0 1:1] 763[0:3 0:0 1:1])<(751 752 753))
     (803<(761[0:3 0:0 2:2] 762[0:3 0:0 2:2] 763[0:3 0:0 2:2])<(751 752 753))
     (803<(764[0:3 0:0 0:0] 765[0:3 0:0 0:0] 766[0:3 0:0 0:0])<(754 755 756))
     (803<(764[0:3 0:0 1:1] 765[0:3 0:0 1:1] 766[0:3 0:0 1:1])<(754 755 756))
     (803<(764[0:3 0:0 2:2] 765[0:3 0:0 2:2] 766[0:3 0:0 2:2])<(754 755 756))
     T
FM104  4.8806E-06 2339 103
SD104          1   6r                 $    Unity normalization for efficiency
FQ104  T F E
```

```
C
FC114    Flux-integrated He3 signal
 F114:n  (803 < 761[0:3 0:0 0:0] < 751)
         (803 < 762[0:3 0:0 0:0] < 752)
         (803 < 763[0:3 0:0 0:0] < 753)
         (803 < 761[0:3 0:0 1:1] < 751)
         (803 < 762[0:3 0:0 1:1] < 752)
         (803 < 763[0:3 0:0 1:1] < 753)
         (803 < 761[0:3 0:0 2:2] < 751)
         (803 < 762[0:3 0:0 2:2] < 752)
         (803 < 763[0:3 0:0 2:2] < 753)
         (803 < 764[0:3 0:0 0:0] < 754)
         (803 < 765[0:3 0:0 0:0] < 755)
         (803 < 766[0:3 0:0 0:0] < 756)
         (803 < 764[0:3 0:0 1:1] < 754)
         (803 < 765[0:3 0:0 1:1] < 755)
         (803 < 766[0:3 0:0 1:1] < 756)
         (803 < 764[0:3 0:0 2:2] < 754)
         (803 < 765[0:3 0:0 2:2] < 755)
         (803 < 766[0:3 0:0 2:2] < 756)
FM114  4.8806E-06 2339 103
SD114          1 71r                  $    Unity normalization for efficiency
FQ114  T F E
C
C ****************************** Other Data Cards ****************************
C
mode n e h t s p a #
cut:n 2j 0 0
phys:n 6j 2
C
cut:h j 1e-3
cut:t j 1e-3
cut:s j 1e-3
cut:e j 1e-3
cut:a j 0 $ 1e-3
cut:# j 0 $ 1e-3
LCA 9j 1
C
c dbcn j j 1 200 1
print -98 -100 -85 -86                 $ eliminates normally useless tables
C
prdmp j 5e5  1 2  5e5
C
C ****************************** Problem Cutoffs *****************************
C
nps 2e8                                $             source particle cutoff
```

A.2 Supplemental readfiles used in rbr01.i

In order to maintain consistency between different MCNPX decks, commonly-used items such as material definitions and source energy spectra are stored in external files. These files are read into the code via the "read file" card. The file extension ".trf" is used to uniquely identify this type of file on the Windows platform.

lanl_gas.trf

```
C …..................................................................
C
C Gas mixes based on LANL standard proportional gases
C DSC Naked gas (D) is composed of **.*% He4, **.*% C2H6, **.*% CF4, **.*% Ar
C *DSC Naked gas mix is protected by CRADA agreement
C Makela gas (M) is composed of 7.7% C2H6, 43.6% CF4, 48.7% Ar
C The BaseGas column refers to the base gas used and its pressure in mbar
C
C  mat  BaseGas  He-3 pp      g/cc     He3/b*cm
C m2340  M1000  5.000E-02  2.443E-03  1.2202E-06
C m2341  M1000  1.000E-01  2.449E-03  2.4403E-06
C m2342  M1000  3.000E-01  2.474E-03  7.3209E-06
C m2343  M1000  2.500E-02  2.440E-03  6.1008E-07
C m2344  D0800  2.000E-01  *.***E-03  *.****E-06
C
m2339 2003 1                    $ pure He-3 for rxn rate calculation
m2340 2003 5.0E+01 1001 4.620E+02 6012 5.9E+02 9019 1.744E+03 18000 4.870E+02
      gas=1
m2341 2003 1.0E+02 1001 4.620E+02 6012 5.9E+02 9019 1.744E+03 18000 4.870E+02
      gas=1
m2342 2003 3.0E+02 1001 4.620E+02 6012 5.9E+02 9019 1.744E+03 18000 4.870E+02
      gas=1
m2343 2003 2.5E+01 1001 4.620E+02 6012 5.9E+02 9019 1.744E+03 18000 4.870E+02
      gas=1
m2344 2003 *.*E+0* 2004 *.***E+0* 1001 *.*E+0* 6012 *.***E+0* 18000 *.***E+0*
      9019 *.***E+0* gas=1
C
```

poly_3221.trf

```
c  polyethelene   density .92-.95 gm/cc
m3221     1001 2 6000 1
           nlib .66c
mt3221    poly.01t
```

air_2201_lineC.trf

```
C Air at LANSCE line 'C'
C 2120m, 21C, 10% Rel. Humidity
C Atmosphere density 9.264E-04 g/cc
m2201 pnlib=99u plib=04p elib=03e hlib=.24h gas=1
      1001   3.31142E-03
      1002   4.96787E-07
      2003   3.58769E-12
      2004   2.61875E-06
      6012   1.87820E-04
      6013   2.08900E-06
      7014   7.77545E-01
      7015   2.88760E-03
      8016   2.10878E-01
      8017   8.45543E-05
      8018   4.22771E-04
     10020   8.23427E-06
     10021   2.45718E-08
     10022   8.41811E-07
     18036   1.57304E-05
     18038   2.94070E-06
     18040   4.64910E-03
     36078   1.99405E-09
     36080   1.28189E-08
     36082   6.60884E-08
     36083   6.55187E-08
     36084   3.24745E-07
     36086   9.85629E-08
     54124   4.34792E-11
     54126   3.91313E-11
     54128   8.30453E-10
     54129   1.14785E-08
     54130   1.78265E-09
     54131   9.21760E-09
     54132   1.16959E-08
     54134   4.52184E-09
     54136   3.86965E-09
C #       mx2201:n   mx2201:p   mx2201:h
C  1001      j
C  1002      j
C  2003
C  2004
C  6012
C  6013
C  7014
C  7015
C  8016
C  8017
C  8018
C 10020
C 10021
C 10022
C 18036
C 18038
C 18040
C 36078
C 36080
C 36082
C 36083
C 36084
C 36086
C 54124
C 54126
C 54128
C 54129
C 54130
C 54131
```

```
C 54132
C 54134
C 54136
```

concrete_lanl_m5.trf

```
c concrete (los alamos)   density = 2.3 gm/cc
m5     pnlib=99u  hlib=.24h
     1001   8.47509e-2
     1002   1.27145e-5
     8016   6.02636e-1
     8017   2.41634e-4
     8018   1.20817e-3
     11023  9.47250e-3
     12024  2.36833e-3
     12025  2.99826e-4
     12026  3.30108e-4
     13027  2.48344e-2
     14028  2.23067e-1
     14029  1.12949e-2
     14030  7.49766e-3
     19000  6.85513e-3
     20040  1.98543e-2
     20042  1.42511e-4
     20043  2.76491e-5
     20044  4.27229e-4
     20046  8.19232e-7
     20048  3.82991e-5
     26054  2.74322e-4
     26056  4.26455e-3
     26057  9.76401e-5
     26058  1.30187e-5
mx5:p      0 j j j j j j j j j j j model
           j j j j j j j j j j
mx5:h    j j j 8016 8016 model model model model j
         j j j model j 20040 20040 20040 20040 20040
         j j j j
```

304.trf

```
c  SS304  8.03 gm/cc
m1     6000    -0.08
       25055   -2.00
       15031   -0.045
       16032   -0.030
       14028   -0.75
       24052  -19.0
       28058  -10.0
       7014    -0.10
       26056  -67.995
```

cf252_unbiased.trf

```
C ......................................................................
C Cf-252 Neutron Energy Spectrum
#      si1     sp1
        A       D
      0.199     0
      0.20   1.983E-02
      0.21   2.017E-02
      0.22   2.050E-02
      0.23   2.081E-02
      0.24   2.111E-02
      0.25   2.139E-02
      0.26   2.166E-02
      0.27   2.191E-02
      0.28   2.216E-02
      0.29   2.239E-02
      0.30   2.261E-02
      0.31   2.282E-02
      0.32   2.302E-02
      0.33   2.321E-02
      0.34   2.339E-02
      0.35   2.356E-02
      0.40   2.431E-02
      0.50   2.530E-02
      0.60   2.581E-02
      0.70   2.595E-02
      0.80   2.583E-02
      0.90   2.551E-02
      1.00   2.504E-02
      1.10   2.445E-02
      1.20   2.377E-02
      1.30   2.304E-02
      1.40   2.226E-02
      1.50   2.145E-02
      1.60   2.063E-02
      1.70   1.980E-02
      1.80   1.897E-02
      1.90   1.814E-02
      2.00   1.733E-02
      2.10   1.654E-02
      2.20   1.576E-02
      2.30   1.500E-02
      2.40   1.427E-02
      2.50   1.356E-02
      2.60   1.287E-02
      2.70   1.221E-02
      2.80   1.158E-02
      2.90   1.097E-02
      3.00   1.039E-02
      3.10   9.836E-03
      3.20   9.304E-03
      3.30   8.797E-03
      3.40   8.314E-03
      3.50   7.854E-03
      3.60   7.416E-03
      3.70   7.000E-03
      3.80   6.605E-03
      3.90   6.230E-03
      4.00   5.874E-03
      4.10   5.537E-03
      4.20   5.218E-03
      4.30   4.916E-03
      4.40   4.630E-03
      4.50   4.359E-03
      4.60   4.104E-03
      4.70   3.862E-03
      4.80   3.634E-03
```

4.90	3.419E-03
5.00	3.215E-03
5.50	2.359E-03
6.00	1.724E-03
6.50	1.256E-03
7.00	9.117E-04
7.50	6.603E-04
8.00	4.771E-04
8.50	3.441E-04
9.00	2.477E-04
9.50	1.781E-04
10.00	1.278E-04
10.50	9.166E-05
11.00	6.564E-05
11.50	4.696E-05
12.00	3.356E-05
12.50	2.397E-05
13.00	1.710E-05
13.50	1.219E-05
14.00	8.687E-06
14.50	6.186E-06
15.00	4.402E-06